

HIGH-THROUGHPUT ELECTRON-BEAM LITHOGRAPHY WITH MULTIPLE
PLASMONIC ENHANCED PHOTEMISSION BEAMLETS

A Dissertation

Submitted to the Faculty

of

Purdue University

by

Zhidong Du

In Partial Fulfillment of the

Requirements for the Degree

of

Doctor of Philosophy

December 2018

Purdue University

West Lafayette, Indiana

THE PURDUE UNIVERSITY GRADUATE SCHOOL
STATEMENT OF DISSERTATION APPROVAL

Dr. Liang Pan, Chair

School of Mechanical Engineering

Dr. Xianfan Xu

School of Mechanical Engineering

Dr. Jong H. Choi

School of Mechanical Engineering

Dr. Peide D. Ye

School of Electrical and Computer Engineering

Approved by:

Dr. Jay P. Gore

Head of the School Graduate Program

To my parents,
Guihua Wei and Jinzeng Du.

ACKNOWLEDGMENTS

First and foremost, I would like to sincerely thank my advisor, Prof. Liang Pan, for his help and guidance during my PhD study. He has been supportive ever since I got admittance to the PhD program. He has put a large portion of his resources into my project for me to use the expensive cleanroom facilities. He has shown me in incalculable ways what it means to do scientific research, and I have benefited tremendously from his valuable discussion and advice. I would also like to thank Prof. Xianfan Xu, for his experimental support and valuable suggestions. I would like to acknowledge Prof. Jong H. Choi and Prof. Peide D. Ye for their help for my PhD project and serving as my committee members.

I would like to express my gratitude and appreciation to all the group members I have been working with, Chen Chen, Ye Wen, Luis Traverso, Anurup Datta, Qiming Chen, Zitao He, Tong Shen, Jin Cui, Shih-Hsin Hsu, and Bojing Yao and many more. Your fruitful discussion and warm accompany makes my Ph.D. study a wonderful experience.

Finally, I would like to offer my greatest gratitude to my family. Without your encouragement and support I will never succeed to finish my Ph.D. study.

TABLE OF CONTENTS

| | Page |
|--|------|
| LIST OF TABLES | 7 |
| LIST OF FIGURES | 8 |
| SYMBOLS | 15 |
| ABBREVIATIONS | 16 |
| ABSTRACT | 17 |
| 1 INTRODUCTION | 20 |
| 1.1 Surface Plasmon Enhanced Electron Beam Lithography | 20 |
| 1.2 Surface Plasmon Polariton | 25 |
| 1.3 Photoemission | 31 |
| 1.4 Electrostatic Lens for Electron-Beam | 33 |
| 1.5 Structure of This Dissertation | 39 |
| 2 PLASMONIC LENS | 40 |
| 2.1 Optical Focusing Beyond the Diffraction Limit | 40 |
| 2.2 Design of Plasmonic Lens | 41 |
| 3 PLASMONIC ENHANCED PHOTOEMISSION SOURCE | 54 |
| 3.1 Fabrication of Plasmonic Lens | 54 |
| 3.2 Surface Plasmon Enhanced Photoemission | 60 |
| 3.3 Test of Plasmonic Electron-Beam Source | 68 |
| 4 ELECTROSTATIC LENS FOR ELECTRON-BEAM | 73 |
| 4.1 Design and Analysis of Electrostatic Lens | 73 |
| 4.2 Fabrication of Electrostatic Lens | 82 |
| 5 MULTIPLE ELECTRON-BEAM LITHOGRAPHY SYSTEM | 88 |
| 6 LITHOGRAPHY RESULTS AND DISCUSSION | 94 |
| 6.1 Lithography Results | 94 |

| | Page |
|--------------------------|------|
| 6.2 Discussion | 98 |
| REFERENCES | 101 |
| VITA | 108 |

LIST OF TABLES

| Table | Page |
|---|------|
| 3.1 The recipe of fabricating bowtie aperture using FIB. | 56 |
| 3.2 The recipe of fabricating bowtie aperture using HSQ/PMMA liftoff. | 59 |
| 3.3 Photocurrent drift and fluctuation. | 68 |
| 4.1 Optimized design parameters of microcolumn. | 79 |
| 4.2 The recipe of fabricating microscale electrostatic lens. | 85 |

LIST OF FIGURES

| Figure | Page |
|---|------|
| 1.1 Schematic overview of the electron optics column [1]. | 23 |
| 1.2 Schematic of 'beam on'/'beam off' states [1]. | 24 |
| 1.3 Schematic diagram of the prototype DEAL device with a SEM micrograph of a device taken at 35 degrees from normal. The vertically aligned carbon nanofiber (VACNF) emitter is seen in the center of the device well [11]. . . | 25 |
| 1.4 Schematic of the multiple-electron-beam lithography approach. Individually addressable UV beamlets shine onto the SPEBL emitter array. The SPEBL emitters focus the UV beamlets and emit electrons with nanoscale source size. The emitted electrons are collected and focused by the microscale electrostatic lenses to form electron beamlets. By scanning the underneath wafer and switching the UV beamlets, arbitrary nanoscale patterns are generated on the wafer. | 26 |
| 1.5 Schematic of the surface plasmon polaritons (SPPs) enhanced electron source. The free space UV photons are coupled into the SPPs and then focused onto the centre electron emission site. The high-energy SPPs excite the internal electrons out of the metal surface. | 27 |
| 1.6 Two semi-infinite media with local dielectric constants ϵ_1 and ϵ_2 separated by a planar interface at $z = 0$ | 27 |
| 1.7 Dispersion curve of Surface Plasmon Polaritons (SPPs) at the interface between semi-infinite large metal and vacuum regions. The damping term η in the Drude model of metal dielectric function is omitted. The plasma frequency ω_p is set to be 15 eV. | 31 |
| 1.8 Three-step model of photoemission. The photoemission process can be model with three steps: 1. Photon absorpition. 2. Electron transport. 3. Electron crossing the surface [25]. | 32 |
| 1.9 Analogies between electron and photon optics. (a) Refraction of light at a plane boundary between two media having refractive indices n_1 and n_2 ; and (b) deviation of an electron beam at a plane boundary separating regions have potentials V_1 and V_2 [33]. | 34 |

| | | |
|------|--|----|
| 1.10 | Cross-sectional view of the cylinder lens. The cylinder lens is the simplest example of electrostatic lens for electron optics. It is composed of two coaxial cylinder shells separated by a gap. The two cylinder shells are made of conducting materials and two potentials V_1 and V_2 are applied to them respectively. The red curves show the equipotential lines of the electric potential. The electrons enter the cylinder lens and focus on the image plane. The cylinder lens has two modes of operation. (a) Accelerating mode: the potential of V_2 is higher. The electrons entering the lens from the left will be accelerated and focused. (b) Decelerating mode: the potential of V_1 is higher. The electrons will be decelerated and focused. . . | 36 |
| 1.11 | Aberrations of electron optics. Electrons entering the lens from the same location or angle are focused to different locations due their different initial energies or angles. The non-perfect focusing behavior is called aberration of the lens (a) Spherical aberration. Spherical aberration happens because paraxial rays passing through a lens are focused to different locations. (b) Chromatic aberration. Chromatic aberration is the error caused by the different focal length of different initial electron energies passing through the lens. The larger the initial electron energy is, the longer the focal length is. | 37 |
| 2.1 | Reflectivity of some common metals versus wavelength at normal incidence with wavelength in the range of 200 nm to 2000 nm [43]. | 44 |
| 2.2 | Parameters of Drude model and propagation length for some common metals. The metals are aluminum, silver, gold, chromium, copper, nickel, platinum and titanium. (a) Plasma frequency ω_p and collision frequency γ calculated using Drude model. The dielectric constants are experiment results from Ref. [44] for wavelengths of 266 nm, 532 nm and 1064 nm. (b) Propagation lengths for the metals at 266 nm, 532 nm and 1064 nm. . | 45 |
| 2.3 | Plasmonic electron emitter. An example design is composed of three concentric rings and a bowtie aperture at the center. The excitation wavelength of the UV laser is 266 nm. A 50-nm-thick Al and a 15-nm-thick Au are deposited on the fused silica substrate with predefined rings. The radii for the three rings are 364 nm, 521 nm and 678 nm, respectively. The centred bowtie aperture is patterned through the dual-layer metallic film. The size of the bowtie is 260 nm with a 25-nm gap. (a) Top and cross-sectional views of the optical intensity enhancement compared to that of the incident light. (b) Top and cross-sectional views of the normalized optical absorption distribution. | 47 |

- 2.4 Different aperture designs with one, two and three hot spots. (a-c) Top view of the optical intensity enhancement compared to that of the incident light. The insets show the aperture design. (e-g) Top view of the normalized optical absorption distribution. The excitation wavelength of the UV laser is 266 nm. And it is linearly polarized in the horizontal direction. A 80-nm-thick Cr film is deposited on the fused silica substrate. (a) The size of the bowtie aperture is 200 nm by 200 nm with a 20-nm gap at the center. (b) The size of the C aperture is 200 nm by 200 nm with 30-nm gap. The width of the tip at the bottom is 120 nm. (c) The size of the three-tip aperture is 150 nm by 300 nm. The gap between the tips and the aperture edge is 50 nm. The three tips are separated by 50 nm. The numbers of optical absorption hot spots are one, two and three for the C, bowtie and three-tip apertures, respectively. 48
- 2.5 Different aperture designs with line and split ring hot-spot distributions. (a-c) Top view of the optical intensity enhancement compared to that of the incident light. The insets show the aperture design. (e-g) Top view of the normalized optical absorption distribution. The excitation wavelength of the UV laser is 266 nm. And it is linearly polarized in the horizontal direction for (a) and (b). It is left or right circular polarized for (c). A 80-nm-thick Cr film is deposited on the fused silica substrate. (a) The narrow slit gap is 20 nm and there are two openings on the two ends to improve the uniformity of the field distribution. (e) The optical absorption distribution of the narrow slit shows two adjacent hot-spot lines separated by 20 nm. (b) The wide slit gap is 100 nm and there are two openings on the two ends to improve the uniformity of the field distribution. (f) The optical absorption distribution of the wide slit shows two hot-spot lines separated by 100 nm. Because of the narrow gap, the electrons emitted will merge into single line on the image plane of the electron optics. (c) The diameter of split ring is 260 nm and the gap is 20 nm. The opening of the split ring is 50 nm. 50

- 2.6 The novel quasi-3D plasmonic lens design. The quasi-3D plasmonic lens design has two sets of mismatched half-ring slit gratings on both sides of a push pin structure shown in the right inset. The plasmonic material is chosen be Al for its low loss. There is another Al layer placed 5 nm away from the push pin top surface. The left inset shows the light intensity profile at a distance of 2.5 nm from the 10-nm-diameter pins top surface. The intensity enhancement is 2500 times with a focus spot diameter of 20 nm. The substrate is sapphire and the working wavelength is 355 nm. The linear polarized light is shining from the back side and the polarization is along the symmetric axis of the plasmonic structure. The thickness of the Al film is 80 nm. The width of the grating slits is 40 nm and the radii of the left and right set of gratings are 140 and 380, 260 and 500 nm, respectively. The pin structure is 10 nm tall and 10 nm in diameter [42]. 52
- 3.1 SEM images of the bowtie aperture fabricated using focused ion beam. (a) Top view of the bowtie aperture. The bowtie aperture is milled on a 70-nm-thick Cr film using 10-pA FIB current. The gap is 20.6 nm. (b) Tilt view of the bowtie aperture shows that the sharp edges are rounded during the milling process. 55
- 3.2 SEM images of (a) C aperture and (b) bowtie aperture with concentric rings fabricated using focused ion beam. 55
- 3.3 SEM images of the bowtie aperture fabricated using electron-beam lithography and liftoff. (a) SEM image of the patterned hydrogen silsesquioxane (HSQ). The HSQ is negative tone EBL resist which exposed area remains after development. (b) SEM image of bowtie aperture after pattern transfer using Cr deposition and liftoff. 57
- 3.4 Fabrication process of plasmonic lens using HSQ/PMMA liftoff method. (a) Clean and coat fused silica wafer with HSQ/PMMA bilayer resist. Use EBL to pattern the plasmonic lens with low current. (b) Develop HSQ with 25% TMAH for 40 s and rinse with DI water. (c) Use O₂ plasma RIE to etch PMMA. (d) Deposit 70-nm thick Cr with E-beam PVD. (e) Use acetone to do the liftoff. (f) Plasmonic lens array fabricated using HSQ/PMMA liftoff method. 58

- 3.5 Quantum efficiency map of bowtie aperture. The map of quantum efficiency is calculated using the power loss density simulated by the FDTD EMW tool, CST. There is a 15-nm thick gold on top of the 70-nm thick chrome film to harvest the SPP energy and prevent the contamination of photoemission metal surface. The substrate is fused silica and laser wave length is 266 nm. (a) The absorption ratio distribution of the bowtie aperture. It is defined as the ratio of absorbed optical areal energy density through the gold layer over the incident light areal energy density from the fused silica substrate. (b) The local absorption ratio distribution along the vertical direction of the bowtie plane at one of the bowtie tips. (c) Calculated F_{e-e} . F_{e-e} is the ratio of excited electrons transported to the metal-vacuum interface over the incident photons. (d) Quantum efficiency map. It is defined as the ratio of photo-emitted electron over the incident photons. 64
- 3.6 Photoemission test of 12 nm thick gold film deposited on fused silica substrate. The vacuum pressure is 3×10^{-6} mbar. The laser beam with 266 nm wavelength is shining onto the sample from the substrate side through vacuum viewport. A UV grade viewport is used to maintain good transmission at 266 nm. The laser power is 28.8 mW before the viewport. . . . 65
- 3.7 Photocurrent test of 81 bowtie apertures. The laser has a beam of power of 75 mW and 500 μ m beam diameter. The vacuum pressure is 3.8×10^{-6} mBar. The Cs dispenser is heated with 3 A for 60 s to deposit a thin film onto the bowtie apertures. A voltage of 100 V is applied to accelerate the photoelectrons. The gap between the bowtie apertures and the anode is set at 34 μ m. 67
- 3.8 The proximity lithography system using plasmonic electron-beam source. (a) The schematic of the system setup. (b) The physical process of the proximity lithography. There are six steps of the process. i) Incident UV light. ii) Focused plasmons. iii) Hot electron generation. iv) Electron emission. v) Accelerated beam. vi) Guided beam. vii) Deep resist pattern formation. 70
- 3.9 The microscopic image of the island with bowtie apertures. The substrate is quartz and a center island with 10 μ m height is fabricated to reduce the contact area. The top surface of the island has an area of 35 μ m by 35 μ m. The bowtie apertures are milled on the 70 nm thick Cr film on top of the island. 71

| Figure | Page |
|---|------|
| 3.10 The AFM image of the developed PMMA resist after one hour irradiation of the photoelectrons from the array of bowtie apertures. A bias voltage of 50 V is applied between the bowtie apertures and the Si wafer underneath. A laser beam with intensity of 0.4 MW/m^2 is irradiating on the bowtie apertures. | 72 |
| 4.1 The electrostatic microcolumn: schematic of the components and parameters. The system is composed of three electrodes. The plasmonic lens is fabricated on the source electrode where the electrons are generated by plasmonic enhanced photoemission. The extractor and focus electrodes are accelerating and focusing the electrons onto the silicon wafer underneath. The gap between the focus electrode and the silicon wafer is called working distance (WD). | 74 |
| 4.2 The scaling capability and the dependence of spot size in FWHM on (a) extraction voltage, (b) focusing voltage, (c) distance between source and extractor, (d) distance between extractor and focusing electrode, (e) aperture diameter, and (f) thickness of each electrode. Dashed lines label the optimized parameter values. | 76 |
| 4.3 Spot diagram of the microcolumn with 10-nm-diameter source. The size in full-width half-maximum is (a) 3.69 nm for $L_0 = 1 \mu\text{m}$, (b) 5.32 nm for $L_0 = 5 \mu\text{m}$, and (c) 10.34 nm for $L_0 = 10 \mu\text{m}$ | 78 |
| 4.4 Electronelectron interaction simulation of single column. The spot size was plotted as a function of the beam current. The microcolumn is capable of keeping the spot size variation smaller than 10% over a large current range. | 80 |
| 4.5 Dual-column interaction with different aperture center-to-center distances for $L_0 = 1 \mu\text{m}$. It shows that a minimum spacing of $12 \mu\text{m}$ can safely avoid the field distortion effect from the adjacent microcolumns. | 81 |
| 4.6 Breakdown test of the $2 \mu\text{m}$ thick SiO_2 film. The breakdown voltage is 635 V corresponding to $317.5 \text{ V}/\mu\text{m}$. Above 635 V, the current is limited by the limiting resistance. | 83 |
| 4.7 Optical image of metal layers. The source and focus layers are chromium and the extractor layer is titanium. | 84 |
| 4.8 SEM image of the fabricated microcolumn. (a) The 3×3 array with a spacing of $15 \mu\text{m}$. (b) The cross section of the microcolumn. | 86 |
| 4.9 Delamination of the focus layer due to interface stress and electrostatic force. | 87 |
| 5.1 Illustration of the surface plasmon enhanced photoemission multiple electron-beam lithography system first-stage engineering system using plasmonic lenses (PLs). | 88 |

| Figure | Page |
|--|------|
| 5.2 Image of the high voltage module. | 90 |
| 5.3 Gap detection system. (a) The pair of chirped gratings are used to detect the gap with nanometer accuracy. (b) The working mechanism of ISPI gratings. [7] (c) The SEM image of the fabricated ISPI grating on the electron source sample. (d) The image of the detected interference fringes of the ISPI gratings. The gap is proportional to the numbers of the peaks in the interference pattern. (e) The rough measurement of the gap using grating imaging. The 5 gratings on the right are real and fabricated on the microcolumn sample. The 5 gratings on the left are image of the real gratings reflected by the Si wafer. The distance between these two sets of gratings is proportional to the gap. The scale is set according to the known distance between the real 5 gratings. | 91 |
| 5.4 Image of the first stage multiple electron-beam lithography system. | 92 |
| 5.5 Image of the first stage multiple electron-beam lithography system. | 93 |
| 6.1 Simulation results of the focused beam size using the real geometry parameters, voltages, and working distance of the microcolumns. The electron source is set to a disk with a diameter of 50 nm. The initial electron energy spread is estimated to be 0.5 eV. (a) The image of the electrons landing on the silicon wafer. (b) The histogram of current density distribution with respect to R coordinate. The magnification of the electron optics is -0.5 and an electron beam with FWHM of 25 nm can be achieved. Within the 25 nm diameter beam spot, 25% of the overall current is useful. | 95 |
| 6.2 Compact microscale electrostatic lens designed for plasmonic electron emitters. (a) The electric potential distribution of this compact design. (b) The optimized focused beam size as a function of working distance and source size (Φ). (c) SEM images of the top and oblique views of an electron lens. The lens diameter is 6- μ m diameter. The center bowtie aperture can be clear seen. | 95 |
| 6.3 Maskless lithography results using SPEBL method. (a) An SPEBL device that can produce more than 1 million electron beamlets within a 1-cm ² area. (b) SEM image of an array of electron lenses. (c) The proximity lithography result shows the size of the electron source. (d) SEM image of a line of dots at 22-nm FWHM written by SPEBL at a working distance of 10 μ m. (e) SEM image of parallel-writing of an array of lines. | 96 |
| 6.4 Patterns writtten by SPEBL. (a) An array of letters of 'NSF' are written on the PMMA resist. (b) Zoom-in AFM image of the 'NSF'. | 98 |

SYMBOLS

| | |
|-----------------|--|
| λ | wavelength |
| c | vacuum light velocity |
| \hbar | reduced Planck constant |
| ϵ | dielectric constant |
| q | wave vector |
| ω_p | plasma frequency |
| $R(\omega)$ | reflectivity at frequency ω |
| E_F | Fermi energy |
| λ_{opt} | photon absorption length |
| λ_{e-e} | electron-electron interaction mean free path |
| n | refractive index |
| V | electric potential |
| v | velocity |

ABBREVIATIONS

| | |
|------|----------------------------------|
| CD | Critical Dimension |
| CNT | Carbon Nanotube |
| CW | Continuous Wave |
| DMD | Digital Micromirror Device |
| DSA | Directed Self-assembly |
| DUV | Deep Ultraviolet |
| EBID | Electron-Beam Induced Deposition |
| EBL | Electron Beam Lithography |
| EUV | Extreme Ultraviolet |
| FDTD | Finite-Difference Time-Domain |
| FIB | Focused Ion Beam |
| FWHM | Full Width at Half Maximum |
| HSQ | Hydrogen Silsesquioxane |
| IPA | Isopropyl Alcohol |
| IR | Infrared |
| LEEM | Low Electron Energy Microscopy |
| NA | Numerical Aperture |
| PL | Plasmonic Lens |
| PMMA | Poly Methyl Methacrylate |
| PVD | Physical Vapor Deposition |
| RIE | Reactive Ion Etch |
| SEM | Scanning Electron Microscopy |
| SPPs | Surface Plasmon Polaritons |
| WD | Working Distance |

ABSTRACT

Du, Zhidong Ph.D., Purdue University, December 2018. High-Throughput Electron-Beam Lithography with Multiple Plasmonic Enhanced Photemission Beamlets. Major Professor: Liang Pan, School of Mechanical Engineering.

Nanoscale lithography is the key component of the semiconductor device fabrication process. For the sub-10 nm node device, the conventional deep ultraviolet (DUV) photolithography approach is limited by the diffraction nature of light even with the help of double or multiple patterning. The upcoming extreme ultraviolet (EUV) photolithography can overcome this resolution limit by using very short wavelength (13.5nm) light. Because of the prohibitive cost of the tool and the photomask, the EUV lithography is only suitable for high volume manufacturing of high value. Several alternative lithography technologies are proposed to address the cost issue of EUV such as directed self-assembly (DSA), nanoimprint lithography (NIL), scanning probe lithography, maskless plasmonic photolithography, optical maskless lithography, multiple electron-beam lithography, etc.

Electron-beam lithography (EBL) utilizes a focused electron beam to write patterns dot by dot on the silicon wafer. The beam size can be sub-nanometers and the resolution is limited by the resist not the beam size. However, the major drawback of EBL is its low throughput. The throughput can be increased by using large current but at the cost of large beam size. This is because the interaction between electrons in the pathway of the electron beam. To address the trade-off between resolution and throughput of EBL, the multiple electron-beam lithography was proposed to use an array of electron-beams. Each beam has a not very large beam current to maintain good resolution but the total current can be very high to improve the throughput.

One of the major challenges is how to create a uniform array of electron beamlets with large brightness.

This dissertation shows a novel low-cost high-throughput multiple electron-beam lithography approach that uses plasmonic enhanced photoemission beamlets as the electron beam source. This technology uses a novel device to excite and focus surface electromagnetic and electron waves to generate millions of parallel electron beamlets from photoemission. The device consists of an array of plasmonic lenses which generate electrons and electrostatic micro-lenses which guide the electrons and focus them into beams. Each of the electron beamlets can be independently controlled. During lithography, a fast spatial optical modulator will dynamically project light onto the plasmonic lenses individually to control the switching and brightness of electron beamlets without the need of a complicated beamlet-blanking array and addressable circuits. The incident photons are first converted into surface electromagnetic and electron waves by plasmonic lens and then concentrated into a diffraction-unlimited spot to excite the local electrons above their vacuum levels. Meanwhile, the electrostatic micro-lens will extract the excited electrons to form a finely focused beamlet, which can be rastered across a wafer to perform lithography. The scalable plasmonic enhanced photoemission electron-beam sources are designed and fabricated. An array of micro-scale electrostatic electron lenses are designed and fabricated using typical micro-electro-mechanical system (MEMS) fabrication method. The working distance (WD) defined as the gap from the electron lens to the underneath silicon wafer is regulated using a gap control system. A vacuum system is designed and constructed to host the multiple electron-beam system. Using this demo system, the resolution of the electron beams is confirmed to be better than 30 nm from the lithography results done on poly methyl methacrylate (PMMA) and hydrogen silsesquioxane (HSQ) resists. According to simulation results, the electron beam spot size can be further optimized to be better than 10 nm.

This scheme of high-throughput electron-beam lithography with multiple plasmonic enhanced photoemission beamlets has the potential to be an alternative ap-

proach for the sub-10 nm node lithography. Because of its maskless nature, it is cost effective and especially suitable for low volume manufacturing and prototype demonstration.

1. INTRODUCTION

1.1 Surface Plasmon Enhanced Electron Beam Lithography

Lithography is one of the most important processes in semiconductor manufacturing. It patterns the semiconductor wafer at the nanoscale. Currently, industry is using deep UV immersion (ArF 193nm) with multiple patterning process to create sub-20 nm half pitch patterns. However, current approach is no longer suitable for next generation node device due to diffraction limit of the deep UV light. For optical lithography, the smallest feature size or critical dimension (CD) is governed by the equation: $CD = k_1 \cdot \frac{\lambda}{NA}$, where k_1 is a process related factor, λ is the wavelength of UV light and $NA = n \cdot \sin(\theta)$ is the numerical aperture of the optical system. For a single patterning, the ArF 193 nm light source can only roughly generate 40 nm half pitch patterns so double patterning and quadrupole patterning are used to reduce the CDs. According to the 2015 International Technology Roadmap for Semiconductors (ITRS) Lithography, the CD limit for line and space patterns using ArF Quadruple Patterning is around 10 nm and for hole patterns its about 30 nm. So new technology must be introduced to solve the problem. There are several technical approaches: EUV Lithography, Directed Self-Assembly, Nanoimprint, and Maskless Lithography.

EUV lithography is an optical lithography technique that uses extreme UV light with a wavelength of 13.5 nm. Due to its notorious absorption feature, all optical elements must work in a reflective way using defect-free Mo/Si multilayer mirrors. The biggest issue was the source power and the EUV tool manufacturer, ASML, is making significant progress on the source. The complexity and engineering challenges make the cost of the tool very expensive in the range of 100 million dollars. Given the even higher cost of the mask sets, EUV is only profitable in high volume manufacturing.

The tool is expected to be ready in the near future. Other key challenges for EUV are defects and resist resolution, sensitivity and yield.

Directed Self-Assembly (DSA) can create patterns by using block copolymers that has lowest energy with separate domains of different compositions. The DSA patterns can be guided by lithographically printed features. Both lines/spaces and holes are suitable to use DSA. DSA can be used to make the patterns smaller and uniform. However, the rectification of the CDs is limited by the block copolymer size. The larger the rectification is, the larger the block copolymer needs to be. But the large block copolymer is very hard to anneal which limits its application to large CD rectification.

Maskless lithography is technique that the resist is patterned with programmable writing beams without the need of photomasks. The key advantage of maskless lithography is the flexibility and its potential low cost for low volume manufacturing. The cost of a mask set even for 28 nm node is well above 1 million US dollars. There are several approaches of maskless lithography, such as multiple electron beam lithography [1–4], direct laser writing [5], nearfield plasmonic lens [6, 7], and AFM based maskless lithography [8]. The direct laser writing is suitable for making patterns with feature size larger than 1 μm . The Nearfield plasmonic lens method can achieve a very good resolution and throughput but it has issues of compatibility with current manufacturing process. The AFM base method can also achieve good resolution but the throughput is too small. One of the Maskless lithography tools currently under development uses multiple electron beam lithography because it has the potential to address the tradeoff between resolution and throughput. Electron-beam lithography (EBL) utilizes a focused electron beam to write patterns dot by dot on the silicon wafer. The beam size can be sub-nanometers and the resolution is limited by the resist not the beam size. However, the major drawback of EBL is its low throughput. The throughput can be increased by using a large current but at the cost of large beam size. This is because the interaction between electrons in the pathway of the electron beam. To address the trade-off between resolution and throughput of EBL,

the multiple electron-beam lithography was proposed to use an array of electron-beams. Each beam has a not very large beam current to maintain good resolution but the total current can be very high to improve the throughput. The key challenge is to make a uniform massively parallel electron beam source without the brightness limitation.

There are several approaches to realize the multiple electron beam lithography. The first approach is to use a single bright electron source. The single electron is first expanded and split into an array of electron beams. Currently, the state of art being developed in this scheme is the Mapper shown in Figure (1.1) [1]. The electrons emitted from the single point source are first collimated by the collimator lens into a wide parallel beam. The wide beam is then split by the aperture array into an array of electron beamlets. Right under the aperture array is the condenser lens array which focus the electron beamlets individually onto the beam blanker array. The switching of the individual electron beam is achieved by shifting the electron beam by the beam blanker array which is controlled by the array of light signal. As shown in Figure (1.2) the shifted electron beams will be blanked by the beam stop array. The electron beamlets which passing through the beam stop array will be deflected by the deflector and focused by the objective lens array. The Mapper has been developed for 18 years and it has 66248 beamlets in parallel with resolution compatible with 40-nm logic node lithography. The physical limitation of the overall throughput of Mapper is the brightness of the single electron source. Because of the requirement of thermodynamics, the brightness of the electron source (the current per unit area per unit solid angle) of an electron beam is invariant over any equipotential region of space if irreversible effects are excluded [9]. This optical invariance limits the largest possible throughput of Mapper especially at small resolution.

Another approach is to use an array of carbon fibers as the field emission source [10,11]. As shown in Figure (1.3), an in-situ grown vertically aligned carbon nanofiber (VACNF) was fabricated together with microscale electrostatic lens for electron optics. Electrons at the tip atom of the will be extracted by the electric field between

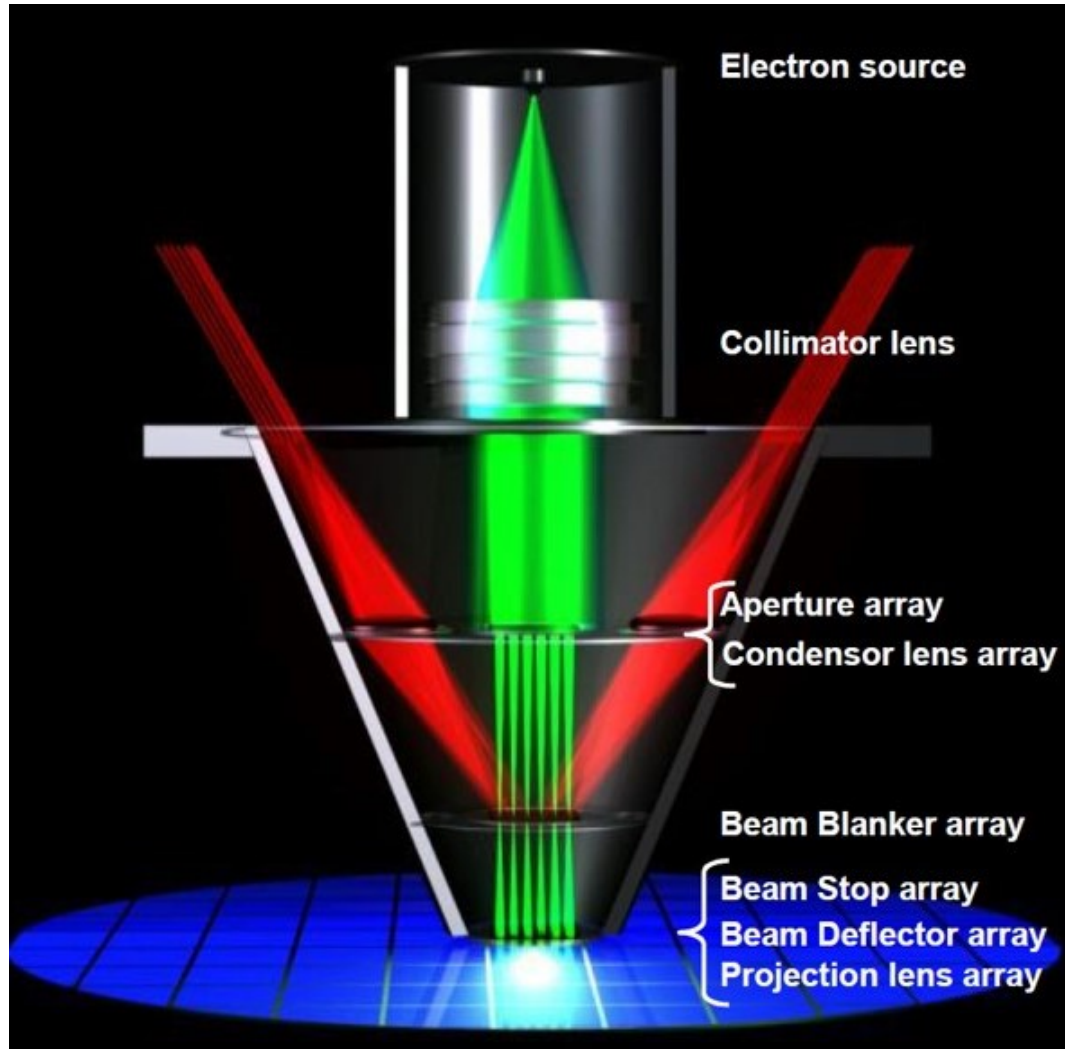


Fig. 1.1. Schematic overview of the electron optics column [1].

the gate electrode and the VACNF. VACNFs are good cathode materials for micro-fabricated field emission devices, due to their low threshold electric field to initiate electron emission. VACNFs can address the brightness limitation, however, they suffer from the poor uniformity. This is due to the field emission nature and the field emission is sensitive to the tip geometry at the atomic scale which make it very hard to make a large array of uniform electron beam source.

Our approach is to develop a new technology, so-called surface-plasmon-enhanced electron beam lithography (SPEBL), which uses the dispersive and quantum natures

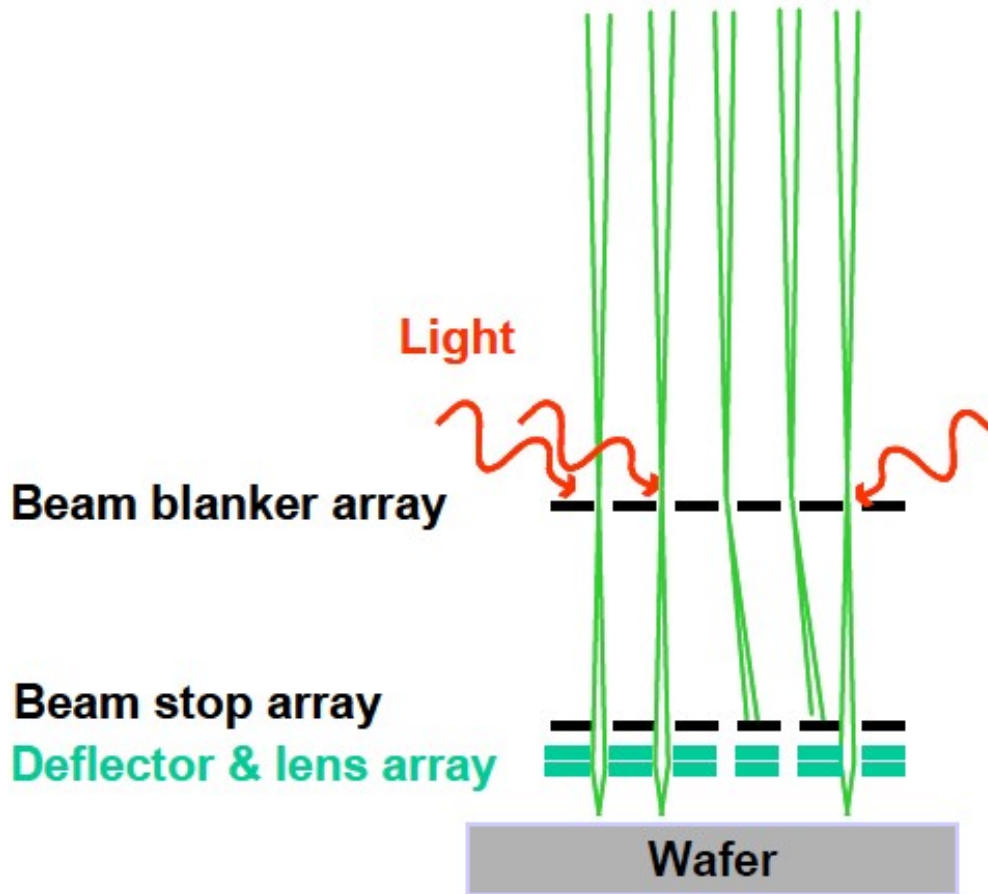


Fig. 1.2. Schematic of 'beam on'/'beam off' states [1].

of plasmonic materials to generate millions of high-quality electron beamlets for parallel direct-write. The SPEBL device shown in Figure (1.4) consists of an array of plasmonic electron emitter and electrostatic micro-lens pairs packed as closely as several micrometers. Each plasmonic electron emitter works as an independent nanoscale electron source. The emitters are made of the standard thin-film structures and robust to geometry variations, therefore we can fabricate them into a massive array with desired uniformity. During operation, optical modulators control the individual emitters by switching of incident UV light beams without the needs for addressable electron-beam shutters. Meanwhile, the electrostatic micro-lenses [12] guide and accelerate the emitted electrons to form beamlets and write on a resist surface.

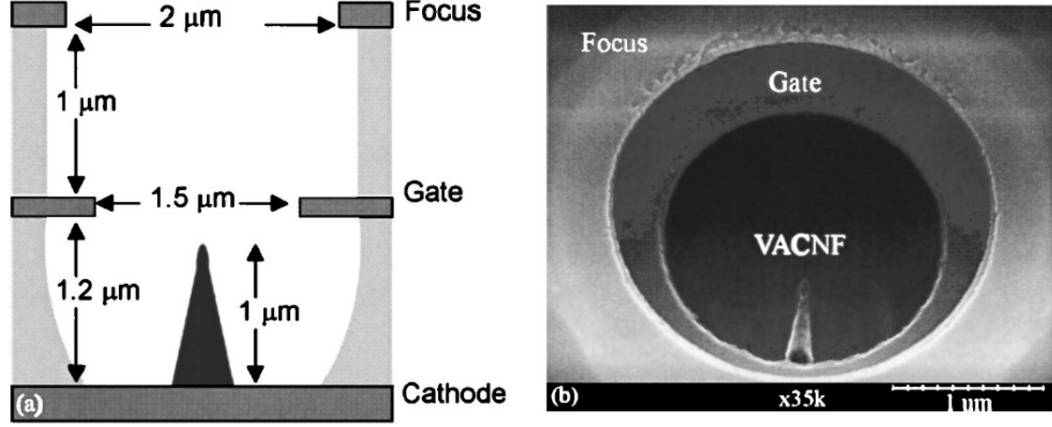


Fig. 1.3. Schematic diagram of the prototype DEAL device with a SEM micrograph of a device taken at 35 degrees from normal. The vertically aligned carbon nanofiber (VACNF) emitter is seen in the center of the device well [11].

The plasmonic electron emitter is the key component in SPEBL. An efficient plasmonic electron emitter needs an effective mechanism to deliver the incident photon energy at the nanoscale with high contrast, meanwhile requires strong material absorptions and low backscattering at the electron emission site. This is achieved through progressive conversions of incident photons into surface plasmon polaritons (SPPs). As illustrated in Figure (1.5), the incident photons are first coupled into propagating-type SPPs by emitters self-contained gratings and guided towards the emitter center. At the center, SPPs are converted into a localized mode and then squeezed into a predefined electron emission site. At this emission site, SPPs strongly interact with electrons and excite them to above their vacuum levels. A portion of these excited electrons can emit into the vacuum and be collected by the electrostatic micro-lens to form an accelerated beamlet.

1.2 Surface Plasmon Polariton

Predicted by Ritchie in 1957 [13], the self-sustained collective excitations at the metal surfaces are named surface plasmon by Stern and Ferrell [14]. Surface Plas-

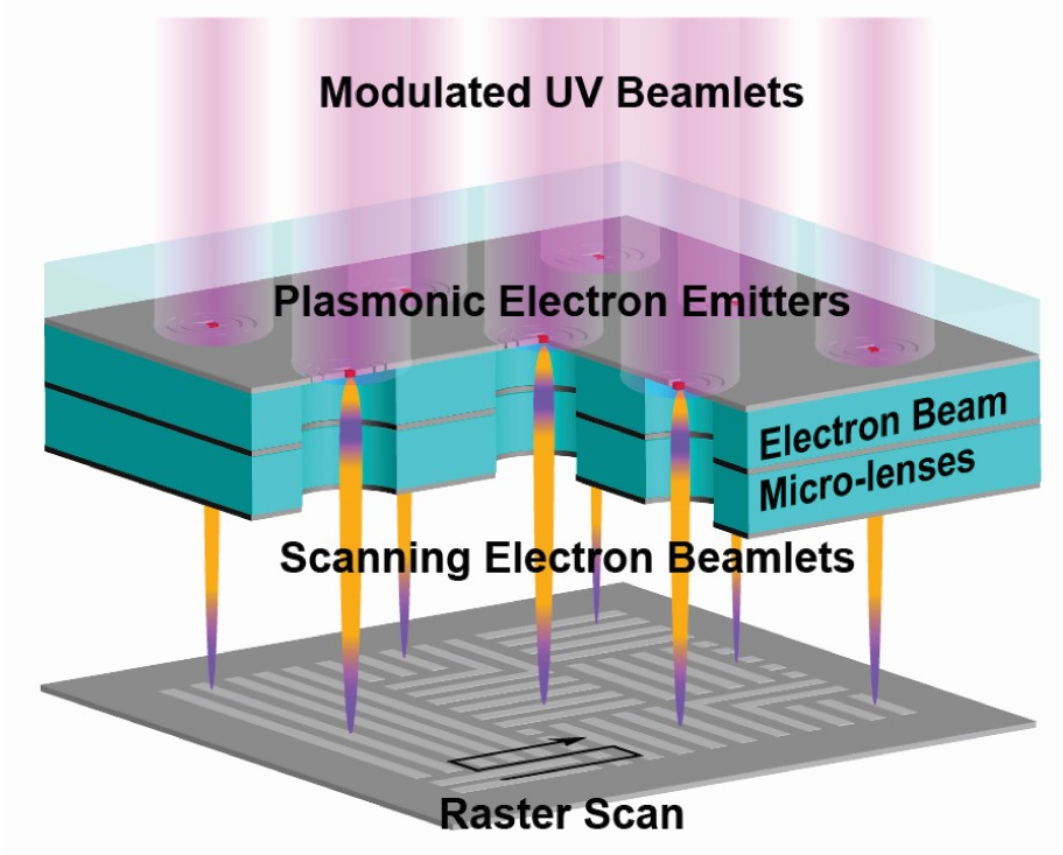


Fig. 1.4. Schematic of the multiple-electron-beam lithography approach. Individually addressable UV beamlets shine onto the SPEBL emitter array. The SPEBL emitters focus the UV beamlets and emit electrons with nanoscale source size. The emitted electrons are collected and focused by the microscale electrostatic lenses to form electron beamlets. By scanning the underneath wafer and switching the UV beamlets, arbitrary nanoscale patterns are generated on the wafer.

mon Polaritons (SPPs) are the quasiparticles resulting from strong coupling between surface plasmons and photons. Because of its superb high wave vector and long propagation length, it is used to focus light to go beyond the diffraction limit. It can be used in nanoscale photonic devices [15, 16], sensors [17], plasmonic lens [18, 19], nanolithography [6, 20], etc.

The SPPs can be analyzed using a classical model [21]. Considering a region of two semi-infinite nonmagnetic media with local dielectric constants ϵ_1 and ϵ_2 separated

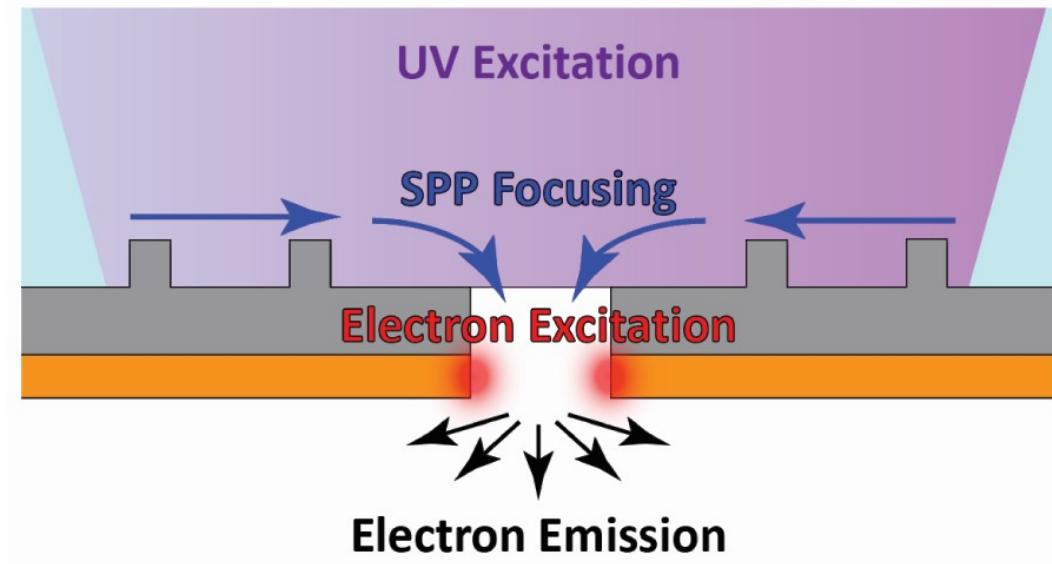


Fig. 1.5. Schematic of the surface plasmon polaritons (SPPs) enhanced electron source. The free space UV photons are coupled into the SPPs and then focused onto the centre electron emission site. The high-energy SPPs excite the internal electrons out of the metal surface.

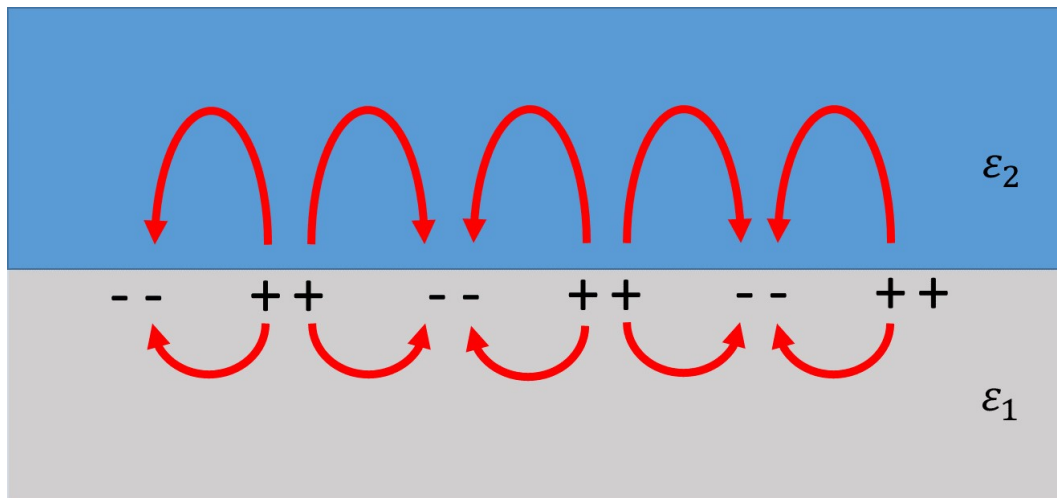


Fig. 1.6. Two semi-infinite media with local dielectric constants ϵ_1 and ϵ_2 separated by a planar interface at $z = 0$.

by a planar interface at $z = 0$, shown in Figure (1.6), the Maxwells equations can be written as follows

$$\nabla \times \mathbf{H}_i = \epsilon_i \frac{1}{c} \frac{\partial}{\partial t} \mathbf{E}_i \quad (1.1)$$

$$\nabla \times \mathbf{E}_i = -\frac{1}{c} \frac{\partial}{\partial t} \mathbf{H}_i \quad (1.2)$$

$$\nabla \cdot \epsilon_i \mathbf{E}_i = 0 \quad (1.3)$$

$$\nabla \cdot \mathbf{H}_i = 0 \quad (1.4)$$

Choose $z < 0$ for ϵ_1 and $z > 0$ for ϵ_2 . If the electromagnetic wave is s-polarized, no E-field component is in the normal direction which contradicts the collective motion of electrons near the interface. So only p-polarized wave is supported at the interface. Choosing the x-axis along the propagating direction, E and H field can be expressed as

$$\mathbf{E}_i = (E_{ix}, 0, E_{iz}) e^{-\kappa_i |z|} e^{i(q_i x - \omega t)} \quad (1.5)$$

$$\mathbf{H}_i = (0, H_{iy}, 0) e^{-\kappa_i |z|} e^{i(q_i x - \omega t)} \quad (1.6)$$

where q_i stands for the wave vector. Introducing Equation (1.5) (1.6) into Equation (1.1) (1.2) (1.3) (1.4), we can find

$$i\kappa_1 H_{1y} = +\frac{\omega}{c} \epsilon_1 E_{1x} \quad (1.7)$$

$$i\kappa_2 H_{2y} = -\frac{\omega}{c} \epsilon_2 E_{2x} \quad (1.8)$$

and

$$\kappa_i = \sqrt{q_i^2 - \epsilon_i \frac{\omega^2}{c^2}} \quad (1.9)$$

Given the boundary conditions that the parallel component of E and H field must be continuous, combining Equation (1.7) (1.8) will give the following equations

$$\frac{\kappa_1}{\epsilon_1} H_{1y} + \frac{\kappa_2}{\epsilon_2} H_{2y} = 0 \quad (1.10)$$

$$H_{1y} - H_{2y} = 0 \quad (1.11)$$

which has a solution only if the determinant is zero,

$$\frac{\kappa_1}{\epsilon_1} + \frac{\kappa_2}{\epsilon_2} = 0 \quad (1.12)$$

Equation (1.12) is the surface-plasmon condition. The wave vector q_i must be continuous, i.e. $q_1 = q_2 = q$. Hence, the surface-plasmon condition Equation (1.12) is rewritten as

$$q(\omega) = \frac{\omega}{c} \sqrt{\frac{\epsilon_1 \epsilon_2}{\epsilon_1 + \epsilon_2}} \quad (1.13)$$

In the case of a Drude semi-infinite metal in vacuum, $\epsilon_2 = 1$ and $\epsilon_1 = 1 - \frac{\omega_p^2}{\omega(\omega + i\eta)}$, where η is a positive small number. Hence, by dropping η , Equation (1.13) yields

$$q(\omega) = \frac{\omega}{c} \sqrt{\frac{\omega^2 - \omega_p^2}{2\omega^2 - \omega_p^2}} \quad (1.14)$$

Choosing $\omega_p = 15$ eV, Equation (1.14) is plotted in Figure (1.7). It can be seen that there are two branches. The upper solid line shows the dispersion of light in the solid. The lower solid is the SPPs

$$\omega^2(q) = \frac{\omega_p^2}{2} + c^2 q^2 - \sqrt{\frac{\omega_p^4}{4} + c^4 q^4} \quad (1.15)$$

which always lies under the light line $\omega = cq$. This tells us that due to the moment mismatch (wave vector q), the SPPs cannot be excited only by shining an external light onto the metal surface. Nevertheless, there are two methods that can couple

external radiation to SPPs: surface roughness or gratings, which can provide the requisite momentum via Umklapp processes [22], and attenuated total reflection (ATR) which provides the external radiation with an imaginary wave vector in the direction perpendicular to the surface [23, 24].

Introducing Equation (1.13) into Equation (1.9), we can get

$$\kappa_i = \frac{\omega}{c} \sqrt{\frac{-\epsilon_i^2}{\epsilon_1 + \epsilon_2}} \quad (1.16)$$

The skin depth d_i is defined as $1/e$ of the electric field in the perpendicular direction which can be calculated as $d_i = 1/\kappa_i$. In order to get propagation wave, the real part of the wave vector q needs to be positive. Equation (1.13) shows that the real part of the metal dielectric constant needs to be more negative than the dielectric constant of the surrounding medium to make SPPs propagate. Because of the loss of the metal material, the SPPs will lose its energy along the propagation through Joule heating. The propagation length is defined as $1/e$ of the intensity of the SPPs along the interface direction which can be calculated as

$$l = \frac{1}{2\text{Im}(q)} \quad (1.17)$$

The dispersion curve shown in Figure (1.7) illustrates that the wave vector of SPPs can be much larger than that of light in free space. This feature can be utilized to focus the light into tiny spot which goes beyond the diffraction limit of light.

The above derivations illustrate a simple classical model of SPPs. A more realistic hydrodynamical model is used to capture the nonlocal feature of the metal dielectric constant caused by the hydrodynamic behavior of the electron system. Metal-dielectric interfaces of arbitrary geometries also support charge density oscillations similar to the planar surface plasmons called localized surface plasmons (LSPs). For simple geometries, like sphere and cylinder, LSPs can be calculated analytically. More complicated structures can be simulated using finite-difference time-domain (FDTD) method or finite element analysis (FEA) method. For composite systems with a large

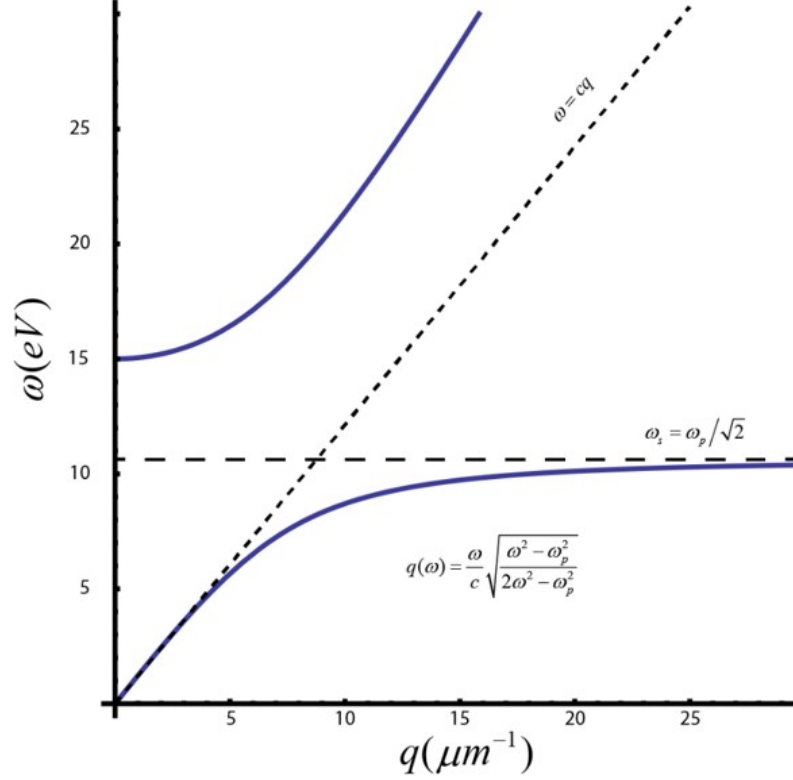


Fig. 1.7. Dispersion curve of Surface Plasmon Polaritons (SPPs) at the interface between semi-infinite large metal and vacuum regions. The damping term η in the Drude model of metal dielectric function is omitted. The plasma frequency ω_p is set to be 15 eV.

number of interfaces with feature size smaller than the wave length, an effective-medium approach can be used. Another approach is sum rule. It has played a key role in providing insight in the investigation of a variety of physical situations [21]. Using these techniques mentioned above, plasmonic lens is designed and focus light well beyond the diffraction limit.

1.3 Photoemission

The photoemission or photoelectric effect is the emission of free electron from materials under light illumination. The emitted electrons are called photo electrons. It was first discovered by Heinrich Hertz in 1887, when he found that the ultraviolet

light helped create electric sparks between electrodes under its illumination. This phenomenon can only be explained by quantum point of view of photons. Albert Einstein proposed that light energy is carried in discrete quantized packets named as photons. He was awarded the Nobel Prize for his discovery of the law of the photoelectric effect.

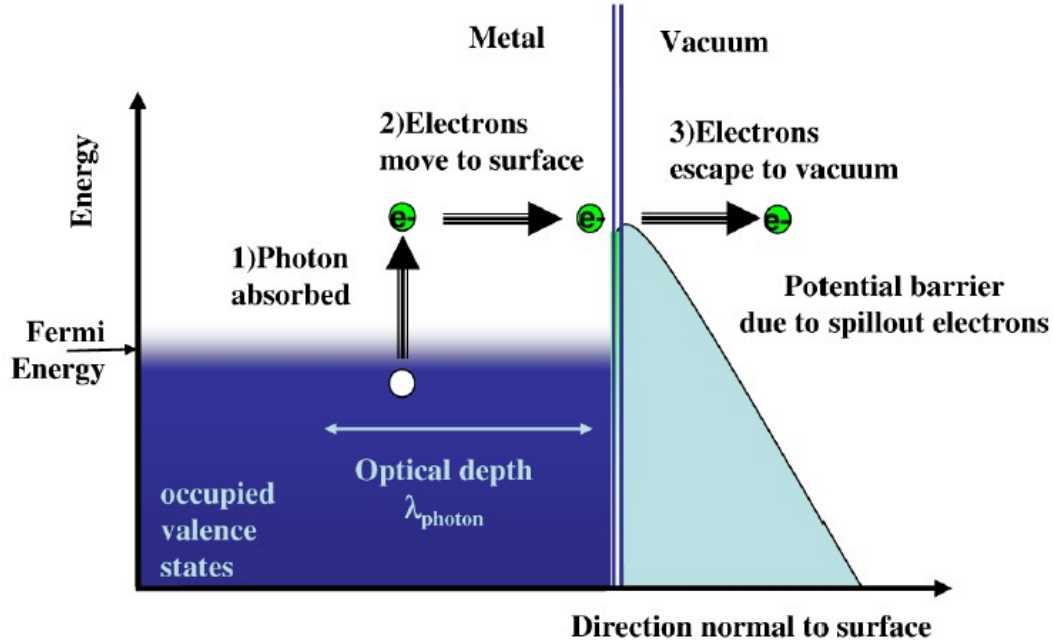


Fig. 1.8. Three-step model of photoemission. The photoemission process can be model with three steps: 1. Photon absorpition. 2. Electron transport. 3. Electron crossing the surface [25].

The photoemission process can be explained in a semi-classical three-step model proposed by Puff [26] and Spicer [27,28]. In this model, the complicated quantum effect is simplified into three steps. The first step is the absorption of the incident photon by an electron in the metal. The second step is the transport of the excited electron to the metal-vacuum interface. In the second step, the excited electron loses its energy through inelastic scattering. In the third step, the electron overcomes the work function and the energy and momentum of the electron changed abruptly

across the metal-vacuum interface. Using this model, the quantum efficiency can be calculated [25] as follows

$$QE(\omega) = \frac{1 - R(\omega)}{1 + \frac{\lambda_{opt}(\omega)}{\lambda_{e-e}(\omega)}} \frac{E_F + \hbar\omega}{2\hbar\omega} \left(1 - \sqrt{\frac{E_F + \Phi_{eff}}{E_F + \hbar\omega}} \right)^2 \quad (1.18)$$

where $R(\omega)$ is the reflectivity of light on the metal surface, E_F is the Fermi energy, $\hbar\omega$ is the photon energy, λ_{opt} is the photon absorption length and λ_{e-e} is the electron-electron mean free path. This model matches well with conventional emission cathode even though the assumption of momentum nonconservation is used [29–31]. Recent research shows that there are more physics involved during the surface plasmon polariton enhanced photoemission process at the metal surfaces [32]. Because of the large field gradient generated by the SPPs at the metal surface, the ponderomotive acceleration cannot be ignored especially under a femtosecond laser irradiation. The SPP-enhanced emission process can be seen as a two-step mechanism. The first step considers an electronic transition from the metallic conduction band to the metal continuum, while in the second step, the freed electrons are accelerated under the ponderomotive force caused by the inhomogeneous SPP field outside the metal.

1.4 Electrostatic Lens for Electron-Beam

In order to focus electron-beam onto the target, there are two types of electron lenses can be used. One is electromagnetic lens which utilizes the Lorentz force to focus the electron-beam. The other is electrostatic lens which uses only the electrostatic force. They have their own advantages and applications respectively. In general, electromagnetic lens has better performance in terms of smaller aberrations, but it is cumbersome and not easy to be miniaturized. Electrostatic lens has slightly larger aberrations, but it is easier to design and fabricated at micrometer scale. In multiple electron-beam system, electrostatic lens is chosen for its potential to be fabricated in a compacted and scalable way.

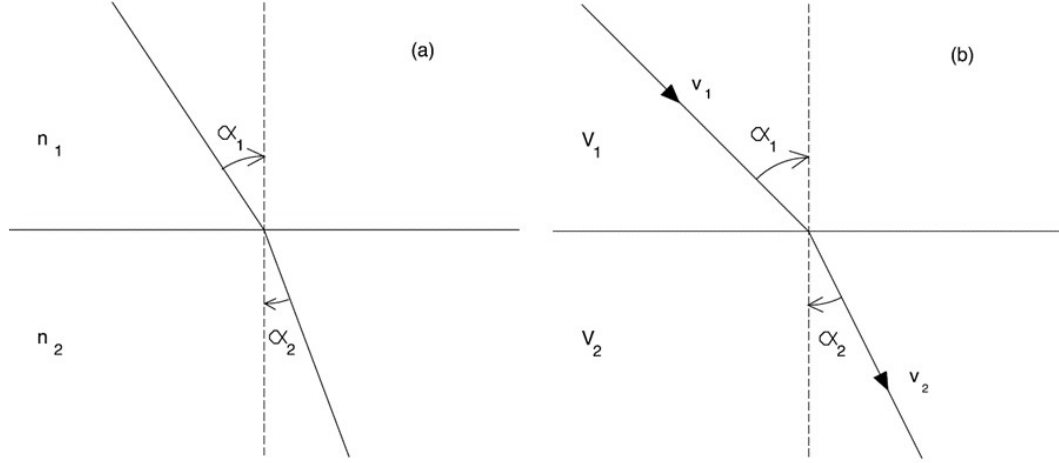


Fig. 1.9. Analogies between electron and photon optics. (a) Refraction of light at a plane boundary between two media having refractive indices n_1 and n_2 ; and (b) deviation of an electron beam at a plane boundary separating regions having potentials V_1 and V_2 [33].

Figure (1.9) shows the analogies between electron and photon optics. It obeys the Snells law that the path of a ray of light crossing the boundary between two media having refractive indices n_1 and n_2 . The angles obey that

$$\frac{\sin(\alpha_1)}{\sin(\alpha_2)} = \frac{v_1}{v_2} = \frac{n_2}{n_1} \quad (1.19)$$

The analogue in electron optics is a boundary separating two regions at different electrostatic potentials. Here we consider an electron with a velocity v_1 in the first region and v_2 in the second. These velocities are related to the potentials, V_1 and V_2 in the two regions by

$$\frac{1}{2}mv_1^2 - eV_1 = \frac{1}{2}mv_2^2 - eV_2 = 0 \quad (1.20)$$

Equation (1.20) defines the zero potential at where the electron is at rest. Given momentum conservation along the boundary, the velocities obey as follows

$$mv_1 \sin(\alpha_1) = mv_2 \sin(\alpha_2) \quad (1.21)$$

Combining Equation (1.20) and (1.21), the analogue Snells law for electron optics is

$$\frac{\sin(\alpha_1)}{\sin(\alpha_2)} = \frac{v_2}{v_1} = \frac{\sqrt{V_2}}{\sqrt{V_1}} \quad (1.22)$$

Comparing Equation (1.19) and (1.22), it can be seen that the term plays the role of refractive index with the proper definition of zero potential.

Figure (1.10) shows the cross-sectional view of the cylinder lens. The cylinder lens is the simplest example of electrostatic lens for electron optics. It is composed of two coaxial cylinder shells separated by a gap. The two cylinder shells are made of conducting materials and two potentials V_1 and V_2 are applied to them respectively. The red curves show the equipotential lines of the electric potential. The electrons enter the cylinder lens and focus on the image plane. The cylinder lens has two modes of operation according to the electric potentials applied to the two cylinders. Figure (1.10)(a) shows the accelerating mode in which the potential of V_2 is higher than that of V_1 . The electrons entering the lens from the left will be accelerated and focused onto the image plane on the right. Figure (1.10)(b) shows the decelerating mode in which the potential of V_2 is lower than that of V_1 . The electrons passing the lens will be decelerated and focused.

The performance of all electron optics, whether used as scanning electron microscopy (SEM) or electron beam lithography (EBL), is limited by fundamental aberrations in the electron-optical system. For an ideal electron-optical system without aberrations, the beam size at the image plane is determined by $M \cdot d_s$ where M is the magnification of the imaging system and d_s is the effective size of electron source. Ideally the beam size can be reduced by increasing the amount of demagnification. Because of thermal dynamics, the brightness of the beam can't exceed that of the electron source where the brightness β is defined as

$$\beta = \frac{I}{\pi d_b^2/4} \cdot \frac{1}{\pi \alpha^2} = \frac{4I}{\pi^2 \alpha^2 d_b^2}, \quad (1.23)$$

where $\frac{I}{\pi d_b^2/4}$ is the current density, $\int_0^\alpha 2\pi \sin(\theta) d\theta = \pi \alpha^2$ is the solid angle at small α . The maximum brightness of the electron beam is limited by the brightness of

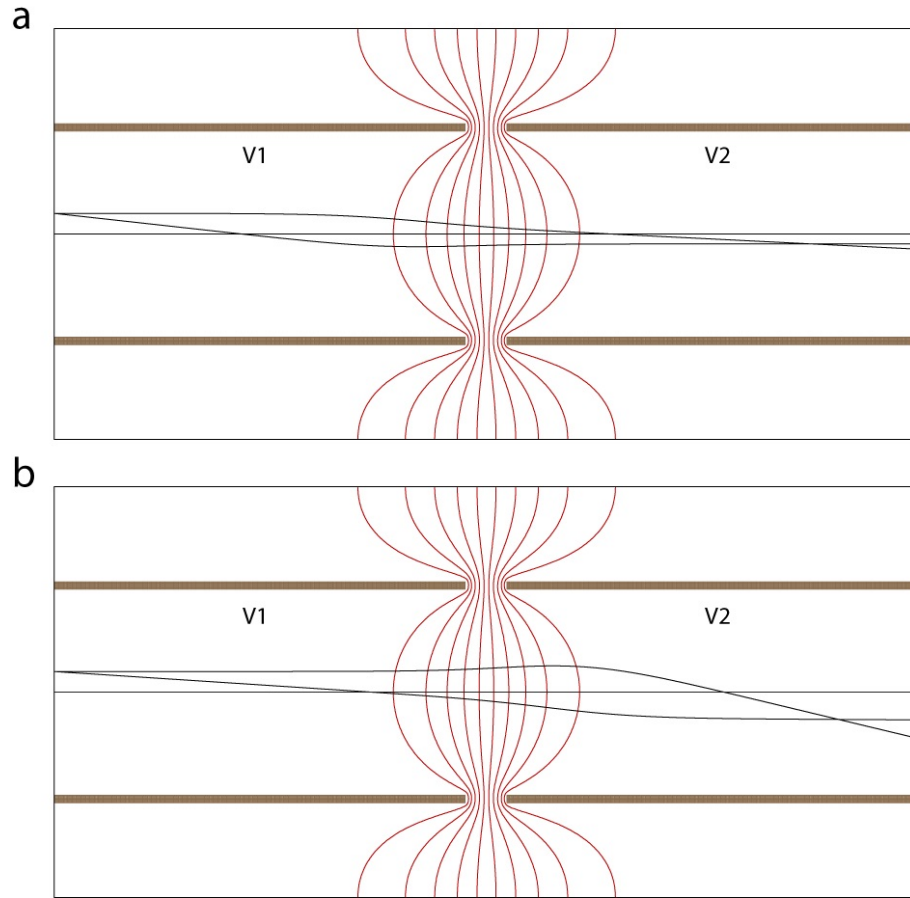


Fig. 1.10. Cross-sectional view of the cylinder lens. The cylinder lens is the simplest example of electrostatic lens for electron optics. It is composed of two coaxial cylinder shells separated by a gap. The two cylinder shells are made of conducting materials and two potentials V_1 and V_2 are applied to them respectively. The red curves show the equipotential lines of the electric potential. The electrons enter the cylinder lens and focus on the image plane. The cylinder lens has two modes of operation. (a) Accelerating mode: the potential of V_2 is higher. The electrons entering the lens from the left will be accelerated and focused. (b) Decelerating mode: the potential of V_1 is higher. The electrons will be decelerated and focused.

the source, so a bright source is needed to achieved a superb resolution and beam current. The brightness equation Equation (1.23) shows that for a given beams size,

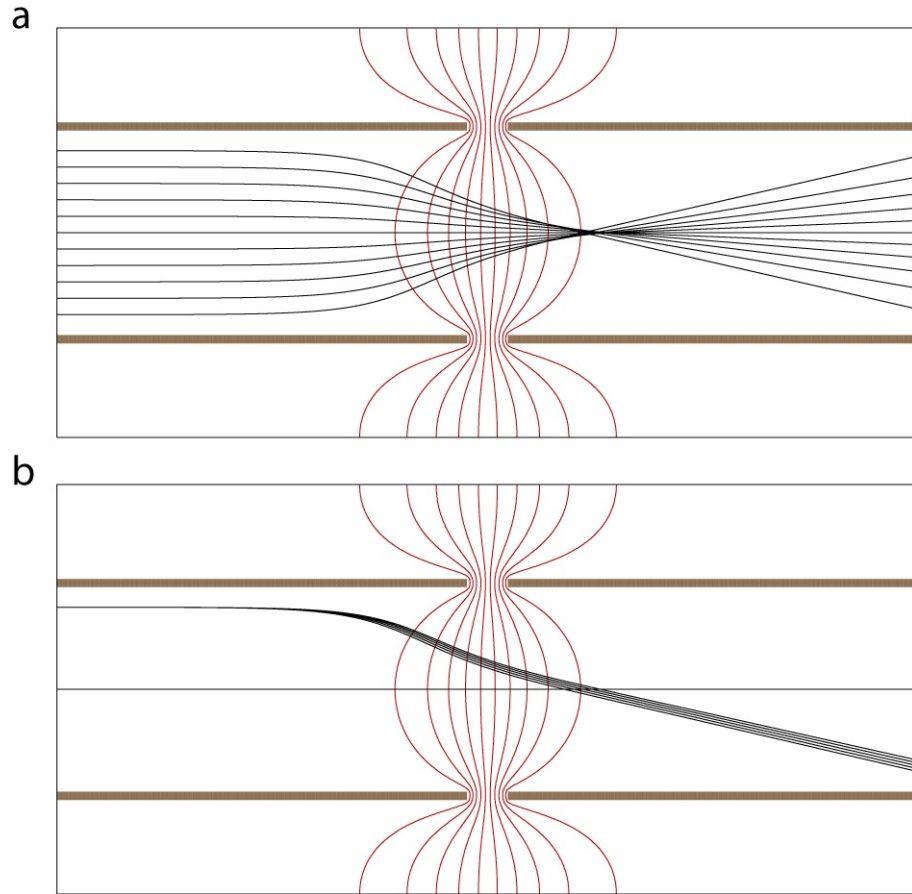


Fig. 1.11. Aberrations of electron optics. Electrons entering the lens from the same location or angle are focused to different locations due to their different initial energies or angles. The non-perfect focusing behavior is called aberration of the lens (a) Spherical aberration. Spherical aberration happens because paraxial rays passing through a lens are focused to different locations. (b) Chromatic aberration. Chromatic aberration is the error caused by the different focal length of different initial electron energies passing through the lens. The larger the initial electron energy is, the longer the focal length is.

the current density can be increased by increasing the angle α . This can be done by reducing the working distance between image plane and the electron lens.

The ideal situation will never appear because of the aberrations shown in Figure (1.11). A point electron source will form a disk on the image plane due to aberrations.

tions. For a typical electron-optical system, three main types of aberrations [34] are geometrical, chromatic and mechanical or parasitic aberrations.

Geometrical aberrations happen when the rays of electrons trajectory are too far from, or at too large an angle to, the axis of the lens. The important example is the spherical aberration which is shown in Figure (1.11)(a). The diameter of the error disk on the image plane caused by spherical aberration is given as

$$d_{sph} = 0.5C_s\alpha^3, \quad (1.24)$$

where C_s is the spherical aberration coefficient in length unit.

Chromatic aberrations describes the focusing errors coming from the different focal length associated with different initial electron energies. This is shown in Figure (1.11)(b). Mechanical or parasitic aberrations come from the small mechanical or electrical imperfections in lenses. An example of this type of aberration is the stigmatic error that the focal length of a lens is different in X and Y directions.

The diameter of the error disk on the image plane caused by chromatic aberration is given as

$$d_{chr} = C_c\alpha\frac{\Delta E}{E_0}, \quad (1.25)$$

where C_c is the chromatic aberration coefficient in length unit. E and ΔE are electron energy and electron energy spread.

Diffraction is not an aberration of the lens but it comes from the wave behavior of electrons especially when the electron kinetic energy is small or convergence angle is too small. The beam profile at the focus has a the form of a central maximum surrounded by several additional peaks of lower intensity called "Airey" disk. The width of the beam diameter d_{Airey} is given as

$$d_{Airey} = 0.61\frac{\lambda}{\alpha}, \quad (1.26)$$

where λ is the wavelength of electrons and it's determined by $\lambda = \frac{1.26}{\sqrt{E_0}}$ nm. E_0 is the electron energy in eV. α is the convergence angle. If the convergence angle α is 10

mrad, for electrons with energy of 100 keV and 100 eV, d_{Airey} are 0.24 nm and 7.7 nm, respectively. So for small electron landing energy electron optics, larger convergence angle should be used to reduce the Airey disk effect. But it's at the cost of increasing the spherical and chromatic aberrations.

Unlike the optical lenses for electromagnetic waves, all electron-optical lenses with ordinary rotationally symmetry display positive-definite aberrations [35]. This was first proven by Scherzer in 1936 and later he showed that this condition didn't extend to lenses with either non-cylindrical symmetry or with varying electron energy or lens excitation with time.

1.5 Structure of This Dissertation

This dissertation focuses on using surface plasmon enhanced photoemission to build novel scalable bright electron-beam source at nanoscale. With the help of surface plasmon enhanced photoemission electron-beam source, a demo system of maskless multiple electron-beam writing is built and tested.

It is organized into 6 chapters. Besides the introduction chapter, the rest chapters are organized as follows.

Chapter 2 focuses on the plasmonic lens design and simulation and fabrication results are shown.

Chapter 4 focuses on the electrostatic lens system design and fabrication.

Chapter 5 shows the demo system of the multiple electron-beam lithography tool.

Chapter 6 shows the lithography test results and its potential applications.

2. PLASMONIC LENS

2.1 Optical Focusing Beyond the Diffraction Limit

The resolution of all conventional optical lens is limited by the diffraction nature of light. The electromagnetic wave reflected from the object has two components according to wave vectors q . The low q component is real and can propagate to as far-field. The high q component is imaginary and decays exponentially. It is an evanescent wave. The information carried by the high q component of the electromagnetic wave is lost during the propagation of light from the object to the image plane. Only the low q component will arrive at the image plane so the spatial frequency of the image is limited. This diffraction limit can be overcome by focusing the evanescent wave onto the image plane. The concept of "superlens" was proposed by John Pendry in 2000 [36]. When $\epsilon = -1$ and $\mu = -1$, the negative refractive index material plate can be a perfect lens. Because of the dispersion and absorption in the materials, the conditions of $\epsilon = -1$ and $\mu = -1$ is hard to satisfy for the natural materials. Although the perfect lens may not exist, the superlens which can provide resolution beyond the diffraction limit have been proved [37].

Surface plasmon polaritons are the strong coupling between the evanescent electromagnetic wave and the collective motion of electrons at the interface between metal and dielectric materials. Plasmonic lens utilizes the large wave vectors of surface plasmon polaritons mentioned in the introduction chapter to focus the light energy into nanoscale spot. Because of the dispersion curve of SPPs lies under the light line, there is momentum mismatch between the free space light and the SPPs. In order to couple the incident light to the surface plasmons, concentric gratings can be used to excite the propagating SPPs to deliver the energy into the center region. Then the propagating SPPs can be coupled to some plasmonic structures which excites the

localized SPPs. The mode of the localized SPPs is typically complicated and can be analyzed numerically.

2.2 Design of Plasmonic Lens

Because of its superb potential to focus beyond diffraction limit, the plasmonic lens is extensively explored for past decades and a variety of brilliant designs have been proposed, such as bulls eye, C-shaped and H-shaped apertures, and the bowtie aperture and antennas [38–41]. Here I use three types of plasmonic lenses. The first design is the bowtie aperture for its easiness of fabrication. The second design is the C aperture for its single hot spot. The third design is the quasi-3D plasmonic lens [42] for its superb focusing performance. The loss of the metal material limits the propagating distance of the SPPs and Q factor as well. As shown in Equation (1.17), the propagation length is inversely proportional to the imaginary part of the dielectric constant. The dielectric constant can be analyzed using the famous Lorentz-Drude model. The equations of motion of an electron in materials can be shown in

$$m_e \frac{d^2 \mathbf{r}}{dt^2} = -m_e \omega_0^2 \mathbf{r} - \gamma m_e \frac{d\mathbf{r}}{dt} - e \mathbf{E}, \quad (2.1)$$

where m_e is the electron mass, γ is the collision frequency and \mathbf{E} is the applied electric field. When the electron is not bound to a particular nucleus like the electrons in the conducting band of metals, the restoring force term $m_e \omega_0^2 \mathbf{r}$ can be neglected.

Substituting the current density $\mathbf{J} = N_e e \mathbf{v}$ in the equation of motion, we can get

$$\frac{d\mathbf{J}}{dt} + \gamma \mathbf{J} = \frac{N_e e^2}{m_e} \mathbf{E}. \quad (2.2)$$

When the conducting material is excited by electromagnetic waves, the applied external electric field is given as $\mathbf{E} = \mathbf{E}_0 \exp(-i\omega t)$. Under the local response approximation the current density can be written as $\mathbf{J} = \mathbf{J}_0 \exp(-i\omega t)$. Substituting these quantities into Equation (2.2) we obtain

$$-i\omega \mathbf{J}_0 \exp(-i\omega t) + \gamma \mathbf{J}_0 \exp(-i\omega t) = \left(\frac{N_e e^2}{m_e} \right) \left(\mathbf{E}_0 \exp(-i\omega t) \right). \quad (2.3)$$

Equation (2.3) can be simplified as

$$(-i\omega + \gamma) \mathbf{J} = \left(\frac{N_e e^2}{m_e} \right) \left(\mathbf{E} \right). \quad (2.4)$$

When ω approaching zero frequency, the static conductivity is written as $\sigma = \frac{N_e e^2}{m_e \gamma}$.

For $\omega > 0$, the current density response is

$$\mathbf{J} = \frac{\sigma}{1 - \frac{i\omega}{\gamma}} \left(\mathbf{E} = \sigma_\omega \mathbf{E} \right), \quad (2.5)$$

where σ_ω is the dynamic conductivity. This is the free electron response to external electric fields. For very low frequencies, $\omega/\gamma \ll 1$, the dynamic conductivity is purely real and the electrons follow the electric field without phase lag. For medium frequency range, the inertia of electrons induces a phase lag in the electron response to the electric field, and the dynamic conductivity is a complex number. For very high frequencies, $\omega/\gamma \gg 1$, the dynamic conductivity is purely imaginary and the electron oscillations are $\pi/2$ phase lag with the applied electric field. This can be seen as an oscillator with infinitely large resonance frequencies.

Applying Equation (2.5) to the maxwell's relation we can get

$$\nabla^2 \mathbf{E} = \frac{1}{c^2} \frac{\partial^2 \mathbf{E}}{\partial t^2} + \frac{1}{\epsilon_0 c^2} \frac{\partial \mathbf{J}}{\partial t} = \frac{1}{c^2} \frac{\partial^2 \mathbf{E}}{\partial t^2} + \frac{1}{\epsilon_0 c^2} \left(\frac{\sigma}{1 - \frac{i\omega}{\gamma}} \right) \left(\frac{\partial \mathbf{E}}{\partial t} \right). \quad (2.6)$$

The solution of Equation (2.6) is

$$\mathbf{E} = \mathbf{E}_0 \exp[i(\mathbf{k} \cdot \mathbf{r} - \omega t)], \quad (2.7)$$

where

$$k^2 = \frac{\omega^2}{c^2} + i \frac{\sigma \omega \mu_0}{1 - \frac{i\omega}{\gamma}} \quad (2.8)$$

is the dispersion relation. And the refractive index can be derived from Equation (2.8) as

$$n^2 = \frac{c^2}{\omega^2} k^2 = 1 - \frac{\gamma \sigma c^2 \mu_0}{\omega^2 + i\omega\gamma} \quad (2.9)$$

The plasma frequency is defined as

$$\omega_p^2 = \gamma \sigma c^2 \mu_0 = \frac{N_e e^2}{m_e \epsilon_0}, \quad (2.10)$$

so the refractive index of the medium is given by

$$n^2 = 1 - \frac{\omega_p^2}{\omega^2 + i\omega\gamma}. \quad (2.11)$$

And using the relationship between the dielectric constant and refractive index, we can get

$$\epsilon = n^2 = 1 - \frac{\omega_p^2}{\omega^2 + i\omega\gamma} = \left(1 - \frac{\omega_p^2}{\omega^2 + \gamma^2}\right) + i \left(\frac{\omega_p^2 \gamma}{\omega^3 + \omega\gamma^2}\right) \quad (2.12)$$

The Drude model is only accurate when the excitation frequency is much lower than the interband transition of metals. Figure (2.1) shows the reflectivity of some common metals in the spectrum from UV to IR. It can be seen that Al, Cu, Au and Ag are good mirrors in the IR wavelength. This is because of the interband transition in the shorter wavelength. The small dip in the reflectivity for Al is because the very high density of states for parallel bands at the critical points which gives an absorption at 1.5 eV. Other than this small dip, Aluminum is a good mirror for wavelength down to 200 nm which means it's a good SPP material for 266 nm UV. Au and Cu shows characteristic colors can be explained by the inner d orbitals form narrow bands below the Fermi energy and the optical transitions to outer half-full s band gives a sharp absorption edge.

Figure (2.2)(a) shows the calculated plasma frequency ω_p and collision frequency γ using the Drude model Equation (2.12) for some common metals. The metals are aluminum, silver, gold, chromium, copper, nickel, platinum and titanium. The

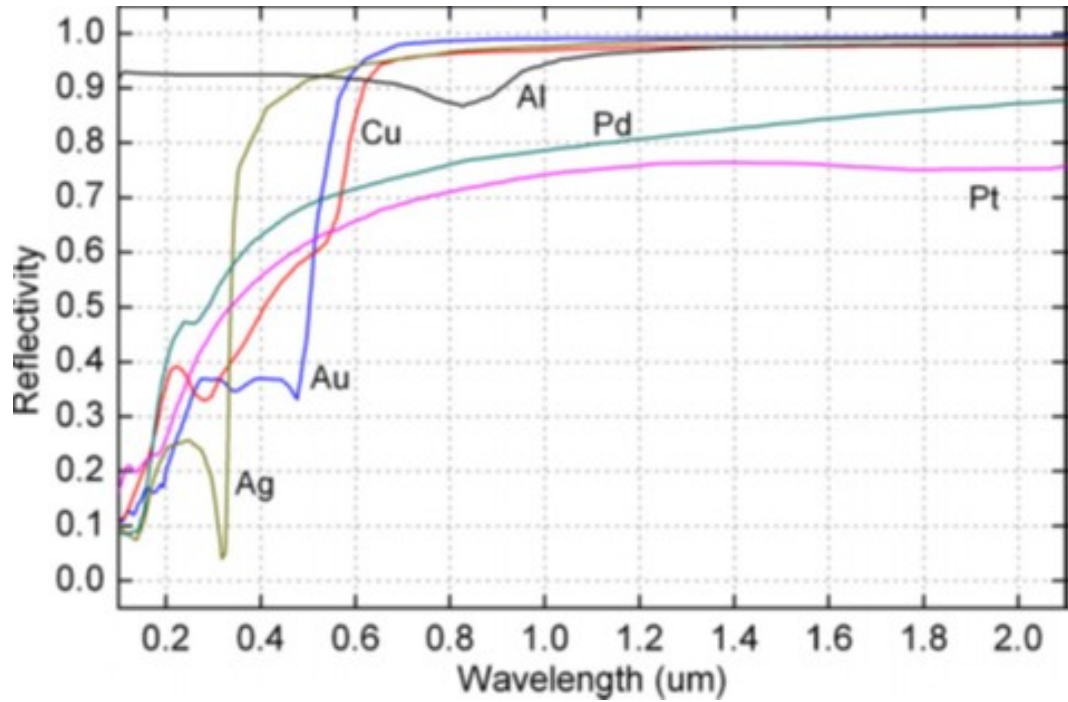


Fig. 2.1. Reflectivity of some common metals versus wavelength at normal incidence with wavelength in the range of 200 nm to 2000 nm [43].

dielectric constants are experiment results from Ref. [44] for wavelengths of UV 266 nm, visible 532 nm and IR 1064 nm. Ideally the plasma frequencies and collision frequencies should be independent of excitation frequencies as shown in Drude model however the discrepancy between Drude model and experiment data comes from the electron-phonon scattering, interband transitions and so on which depend on frequencies. Plasmonic and metamaterial devices have been studied in the microwave, IR and visible spectrum [45–57]. Few studies have been done in the UV spectrum. In order to have photoemission, a 266-nm continuous wave (CW) laser is used to overcome the work function of the metal.

Among the common metals shown in Figure (2.2)(b), the propagation lengths of SPPs increase with the increase of wavelengths of 266 nm, 532 nm and 1064 nm. This trend is true for all the metals listed above because with the increase of the wavelength, the loss due interband transition decrease. In the IR range, silver has

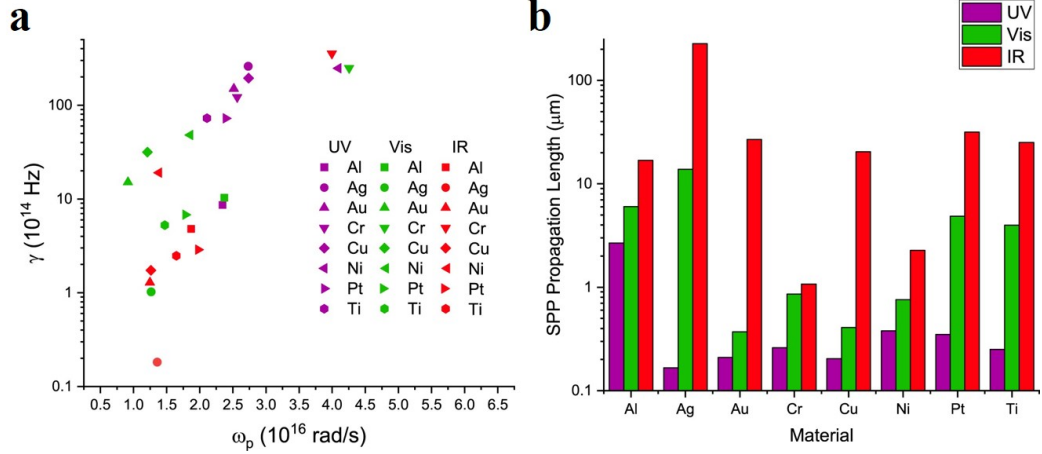


Fig. 2.2. Parameters of Drude model and propagation length for some common metals. The metals are aluminum, silver, gold, chromium, copper, nickel, platinum and titanium. (a) Plasma frequency ω_p and collision frequency γ calculated using Drude model. The dielectric constants are experiment results from Ref. [44] for wavelengths of 266 nm, 532 nm and 1064 nm. (b) Propagation lengths for the metals at 266 nm, 532 nm and 1064 nm.

the best performance in terms of long propagation length. It has a propagation length longer than 200 μm . On the contrary, chrome has the smallest propagation length which is about only 1 μm . Except nickel, other metals have propagation length in the range of several tens of μm . So for metamaterial and plasmonic applications in the IR range silver is a good material to work with but the oxidation of silver in air needs to be carefully taken care of. In the visible range, silver still has the largest propagation length. Besides silver, aluminum, platinum and titanium also have very good performances. They have propagation lengths in the range of 5 μm to 10 μm . The metals of gold, chrome, copper and nickel are lossy materials at the wavelength of 532 nm. Among them, gold has the smallest propagation length of 200 nm. In the UV range, the propagation lengths drops dramatically. Among them, aluminum drops less than 10 times for 266 nm compared to 1064 nm which is best metal material in the UV range. However, the propagation length of silver drops from over 200 μm at 1064 nm to less than 0.2 μm at 266 nm which corresponds to over 1000 times drop.

This is due to the strong interband transition in the UV range. Chrome also has a large loss at 266 nm and the propagation length is only 260 nm but not as bad as silver.

In summary, the common metals have much less loss at 1064 nm compared to 266 nm which corresponds to a larger focusing efficiency for plasmonic lens operating at IR range. Silver has the longest propagation length at the wavelength of 1064 nm. loss of Aluminum in the spectrum from IR to UV doesn't change as much as other metals except the small reflectivity dip shown in Figure (2.1). And aluminum has the smallest loss at the wavelength of 266 nm. However, the quality of aluminum films with the thickness around 100 nm is hard to control and the grain size is larger compared to chrome and titanium. With the help of a metallic seed layer on the dielectric substrate and the control of other deposition parameters, the film quality can be improved [58]. Aluminum is a good metal material working at 266 nm so it is chosen as one of the materials to work with. Chrome is also chosen as the plasmonic lens material because of its high film quality and resistance to chemical and mechanical damage even though it is very lossy at 266 nm.

Figure (2.3)(a) shows optical performance of an example design made of an aluminium-gold double layer on a fused-silica substrate. The initial propagating SPPs are excited at the low-loss aluminium-dielectric interface and are focused between the two opposing tips of the bowtie aperture. This gap mode then radiates along the thickness direction and reaches the absorptive gold surface. The thickness and location of the gold layer are optimized to couple in the SPPs without significant backscattering. The gold layer also helps to enhance the contrast of the emitting site by diminishing the outbound SPPs. Figure (2.3)(b) shows the localized absorption of polariton energy inside the structure. This kind of plasmonic structures has an overall optical efficiency of a few percent, defined by the fraction of the overall incident energy that reached the bowtie center.

From Figure (2.3) it can be seen that there are two absorption hot spots. This corresponds to two electron emission sites. In order to have only one electron emission

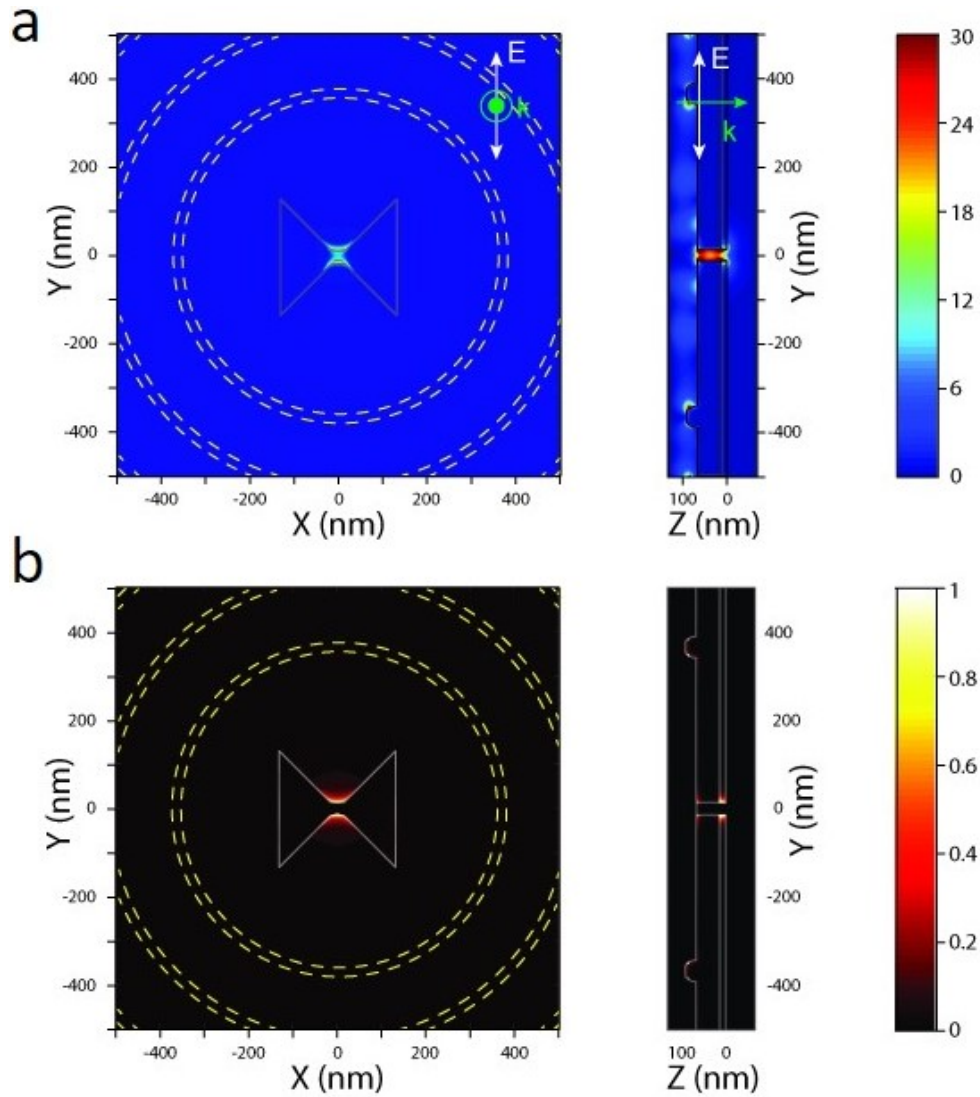


Fig. 2.3. Plasmonic electron emitter. An example design is composed of three concentric rings and a bowtie aperture at the center. The excitation wavelength of the UV laser is 266 nm. A 50-nm-thick Al and a 15-nm-thick Au are deposited on the fused silica substrate with predefined rings. The radii for the three rings are 364 nm, 521 nm and 678 nm, respectively. The centred bowtie aperture is patterned through the dual-layer metallic film. The size of the bowtie is 260 nm with a 25-nm gap. (a) Top and cross-sectional views of the optical intensity enhancement compared to that of the incident light. (b) Top and cross-sectional views of the normalized optical absorption distribution.

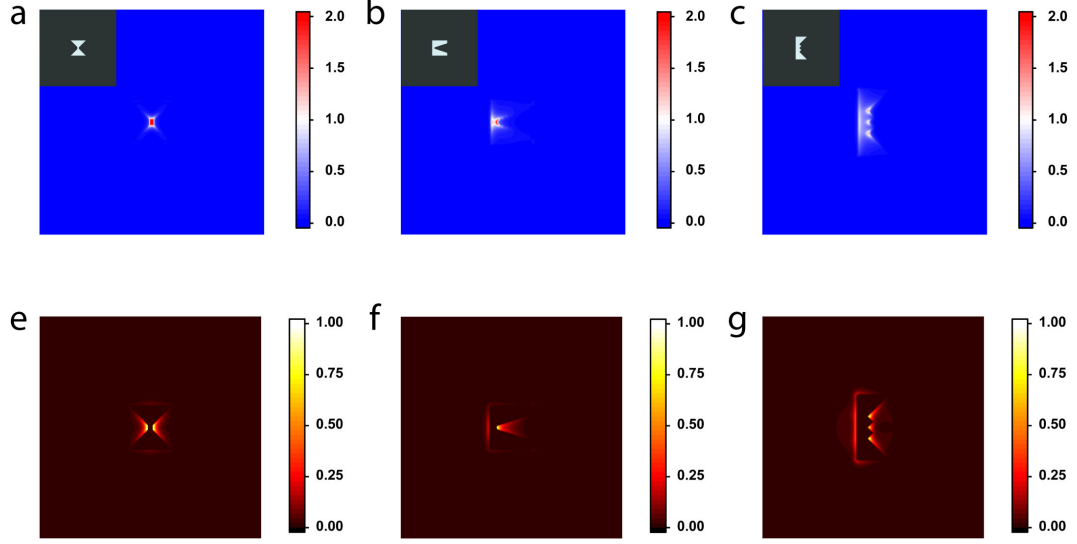


Fig. 2.4. Different aperture designs with one, two and three hot spots. (a-c) Top view of the optical intensity enhancement compared to that of the incident light. The insets show the aperture design. (e-g) Top view of the normalized optical absorption distribution. The excitation wavelength of the UV laser is 266 nm. And it is linearly polarized in the horizontal direction. A 80-nm-thick Cr film is deposited on the fused silica substrate. (a) The size of the bowtie aperture is 200 nm by 200 nm with a 20-nm gap at the center. (b) The size of the C aperture is 200 nm by 200 nm with 30-nm gap. The width of the tip at the bottom is 120 nm. (c) The size of the three-tip aperture is 150 nm by 300 nm. The gap between the tips and the aperture edge is 50 nm. The three tips are separated by 50 nm. The numbers of optical absorption hot spots are one, two and three for the C, bowtie and three-tip apertures, respectively.

site per plasmonic lens, there are several methods. One is to add a thin layer to high work function material (such as MoO_x [59]) to cover one of the hot spot. The thickness of the high work function material is controlled and the SPPs wouldn't change much. Now even though there are two hot spots of SPPs but only one will emit electrons. Another method is to use other plasmonic lens design to get single hot spot. One of the advantages of using plasmonic enhanced photoemission is the flexibility of plasmonic lens design to get a variety of hot-spot distribution. These hot-spot distribution will be imaged at the wafer through the electron imaging optics. One good outcome

is that we can create not only traditional electron beams but also shaped electron beam pattern which can further enhance the throughput of the lithography and have smaller line roughness.

Figure (2.4) shows the design and simulation results of different apertures. Figure (2.4)(a-c) show the top view of the optical intensity enhancement compared to that of the incident light. The insets show the aperture design. Figure (2.4)(e-g) show the top view of the normalized optical absorption distribution. The plots are generated near the interface of the chrome and the vacuum. The excitation wavelength of the UV laser is 266 nm. And it is linearly polarized in the horizontal direction. A 80-nm-thick Cr film is deposited on the fused silica substrate. The size of the bowtie aperture shown in Figure (2.4)(a) is 200 nm by 200 nm with a 20-nm gap at the center. The optical intensity enhancement is 2.4 times. The size of the C aperture shown in Figure (2.4)(b) is 200 nm by 200 nm with 30-nm gap. The width of the tip at the bottom is 120 nm. The optical intensity enhancement is 2.0 times. The size of the three-tip aperture shown in Figure (2.4)(c) is 150 nm by 300 nm. The gap between the tips and the aperture edge is 50 nm. The three tips are separated by 50 nm. The optical intensity enhancement is 1.5, 1.3 and 1.5 times for the three hot spots. The numbers of optical absorption hot spots are one, two and three for the C, bowtie and three-tip apertures, respectively. These designs can be used to direct write multiple dots on the wafer with single shot of electron beams.

The shape of the electron beam generated by the plasmonic enhanced photoemission is not limited to dots. With proper design other useful shapes can be generated such as lines and split rings. Figure (2.5) shows the different aperture designs with line and split ring hot-spot distributions. Figure (2.5)(a-c) show the top view of the optical intensity enhancement compared to that of the incident light. The insets show the aperture design. Figure (2.5)(e-g) show the top view of the normalized optical absorption distribution. The excitation wavelength of the UV laser is 266 nm. And it is linearly polarized in the horizontal direction for Figure (2.5)(a) and (b). It is left or right circular polarized for Figure (2.5)(c). The plots are generated near the

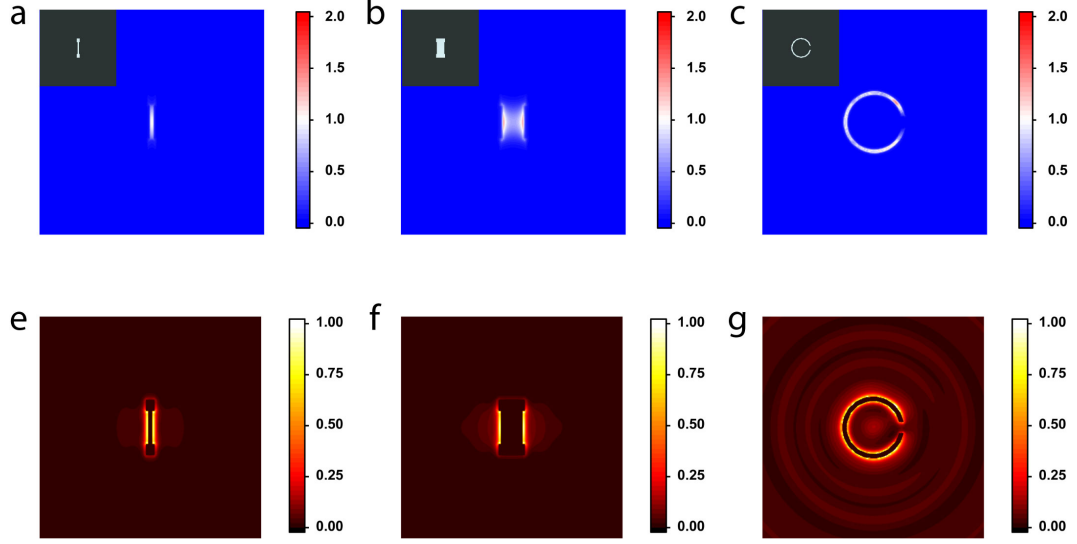


Fig. 2.5. Different aperture designs with line and split ring hot-spot distributions. (a-c) Top view of the optical intensity enhancement compared to that of the incident light. The insets show the aperture design. (e-g) Top view of the normalized optical absorption distribution. The excitation wavelength of the UV laser is 266 nm. And it is linearly polarized in the horizontal direction for (a) and (b). It is left or right circular polarized for (c). A 80-nm-thick Cr film is deposited on the fused silica substrate. (a) The narrow slit gap is 20 nm and there are two openings on the two ends to improve the uniformity of the field distribution. (e) The optical absorption distribution of the narrow slit shows two adjacent hot-spot lines separated by 20 nm. (b) The wide slit gap is 100 nm and there are two openings on the two ends to improve the uniformity of the field distribution. (f) The optical absorption distribution of the wide slit shows two hot-spot lines separated by 100 nm. Because of the narrow gap, the electrons emitted will merge into single line on the image plane of the electron optics. (c) The diameter of split ring is 260 nm and the gap is 20 nm. The opening of the split ring is 50 nm.

interface of the chrome and the vacuum. A 80-nm-thick Cr film is deposited on the fused silica substrate. First a single slit electron source is generated by using a narrow slit shown in Figure (2.5)(a). The narrow slit gap is 20 nm and there are two openings on the two ends to improve the uniformity of the field distribution. Figure (2.5)(e) shows the optical absorption distribution of the narrow slit. There are two adjacent

hot-spot lines separated by 20 nm. Because of the narrow gap, the electrons emitted will merge into single line on the image plane by the aberration of the electron optics when the demagnification ratio is large. The optical intensity enhancement for the narrow slit is 1.02 times. As shown in Figure (2.5)(b) the wide slit gap is 100 nm and there are two openings on the two ends to improve the uniformity of the field distribution. The optical absorption distribution of the wide slit shows two hot-spot lines separated by 100 nm shown in Figure (2.5)(f). The wide slit design will give two separate lines of electron source. The optical intensity enhancement for the wide slit is 1.35 times. For metamaterial applications, the split ring is very important. Figure (2.5)(c) shows the design of split ring electron source. The diameter of split ring is 260 nm and the gap of the slot is 20 nm. The opening of the split ring is 50-nm wide. The peak optical intensity enhancement for the split ring is 1.3 times.

Besides the planar designs shown in Figure (2.3), (2.4) and (2.5), a novel quasi-3D plasmonic lens design (shown in Figure (2.6)) which has an intensity enhancement as high as 2500 times with a spot size of 20 nm [42] is also designed. With this design the electron beam size and brightness can be improved dramatically. Instead of exciting a localized gap resonance horizontally like bowtie aperture, this novel quasi-3D plasmonic lens design excites the direct resonance between the plasmonic structure and the Al sample vertically. The quasi-3D plasmonic lens has two sets of mismatched half-ring slit gratings on both sides of the pin. Each set of the slit gratings has the same period as the SPP wavelength (λ_{SPP}) except that the first ring of the right-hand set is placed at $1 \lambda_{SPP}$ distance away from the pin while the left-hand set is placed at $0.5 \lambda_{SPP}$. Upon the forward plane wave excitation, each slit can generate a localized SPP resonance and further excite the propagating SPP along the metallic surface. The two propagating SPPs launched by the mismatched gratings have a relative phase shift of π at the center, which allows us to construct SPP interference at the center and generate a standing wave with strong electric field along the off-plane direction. At this location, the lightning pole effect of the center pin further converts the background standing wave SPPs into a localized SPP

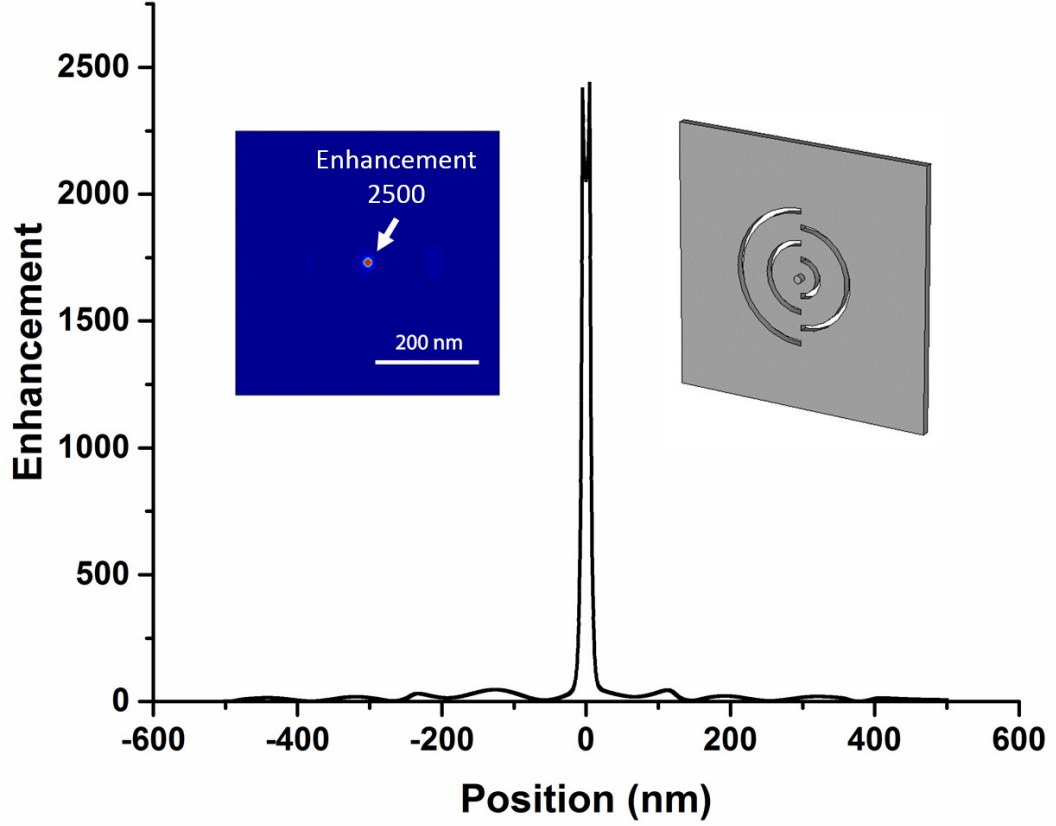


Fig. 2.6. The novel quasi-3D plasmonic lens design. The quasi-3D plasmonic lens design has two sets of mismatched half-ring slit gratings on both sides of a push pin structure shown in the right inset. The plasmonic material is chosen be Al for its low loss. There is another Al layer placed 5 nm away from the push pin top surface. The left inset shows the light intensity profile at a distance of 2.5 nm from the 10-nm-diameter pins top surface. The intensity enhancement is 2500 times with a focus spot diameter of 20 nm. The substrate is sapphire and the working wavelength is 355 nm. The linear polarized light is shining from the back side and the polarization is along the symmetric axis of the plasmonic structure. The thickness of the Al film is 80 nm. The width of the grating slits is 40 nm and the radii of the left and right set of gratings are 140 and 380, 260 and 500 nm, respectively. The pin structure is 10 nm tall and 10 nm in diameter [42].

mode with a strong off-plane electric field resonance between the push pin and the underneath Al film. The localized SPP mode forms a direct interaction between the

collective resonance of the plasmonic nanofocusing structure and the local Al film surface underneath the focus spot.

There are other plasmonic lens design available, I chose the above designs as examples to show the nanofocusing performance potential of plasmonic structures. We can see that they are suitable to generate photoemission with spot size as small as 20 nm. Compared to other ways to generate compacted nanoscale photoemission sources like the carbon nanotube column [60], plasmonic enhanced electron source is sensitive to the geometry at tens of nanometers which is achievable using current nanofabrication technologies. So it has the advantage of uniformity over a large array [7].

3. PLASMONIC ENHANCED PHOTOEMISSION SOURCE

3.1 Fabrication of Plasmonic Lens

The fabrication of plasmonic lens is the key point of the actual performance of the photoemission nano-source. The smallest feature size of the plasmonic lenses designed in chapter 2 is at the order of 10 nm, so how to make an array of plasmonic lenses uniformly over a large area is challenging. There are several methods to fabricate the plasmonic structure. The bowtie aperture is taken as an example to develop the fabrication recipe. Two recipes of fabrication have been developed. One is using focused ion beam (FIB) to mill the unwanted part away from a thin film to get the bowtie aperture. The other is using electron-beam lithography (EBL) to pattern negative tone e-beam resist and deposit and liftoff metal film afterwards to get the bowtie aperture.

Figure (3.1) shows the fabrication results of the bowtie aperture using FIB. The accelerating voltage of the ion beam is set to be 30 keV. A 10-pA ion current is chosen to balance the throughput and milling resolution. The ion milling is operated in a parallel mode to achieve the best results. A larger current can enhance the milling speed but at the cost of a worse resolution. The bowtie aperture has a 20.6-nm gap which meets the requirement of design. Figure (3.1)(b) shows that the sharp edges are rounded during the milling process which affects the performance for optical near field lithography because the peak intensity is away from the top surface, but for photoemission, it doesn't matter much. The final milling resolution is determined by the ion beam size and the interaction between ion beam and materials. It takes about four hours to make one thousand bowtie apertures. The recipe is listed in Table (3.1). First, the fused silica wafer is cleaned with toluene, acetone and IPA

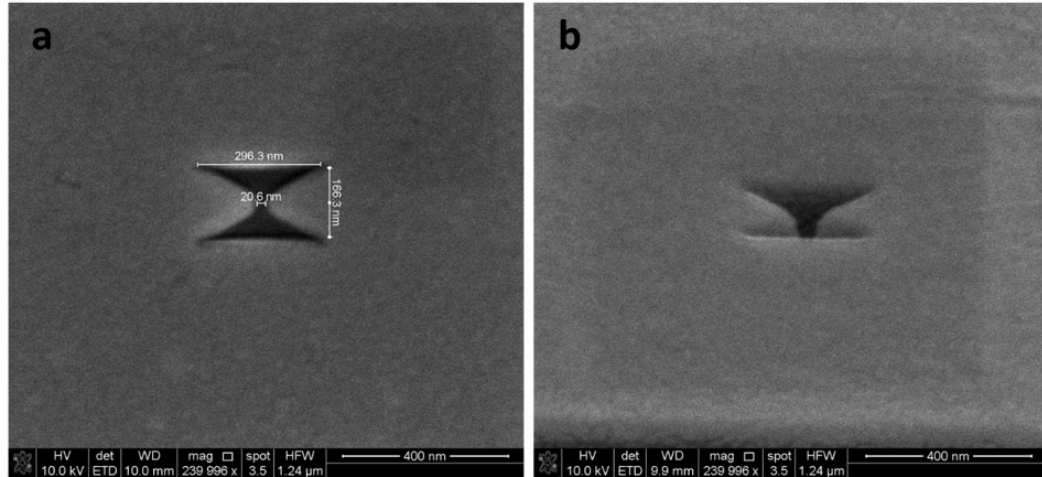


Fig. 3.1. SEM images of the bowtie aperture fabricated using focused ion beam. (a) Top view of the bowtie aperture. The bowtie aperture is milled on a 70-nm-thick Cr film using 10-pA FIB current. The gap is 20.6 nm. (b) Tilt view of the bowtie aperture shows that the sharp edges are rounded during the milling process.

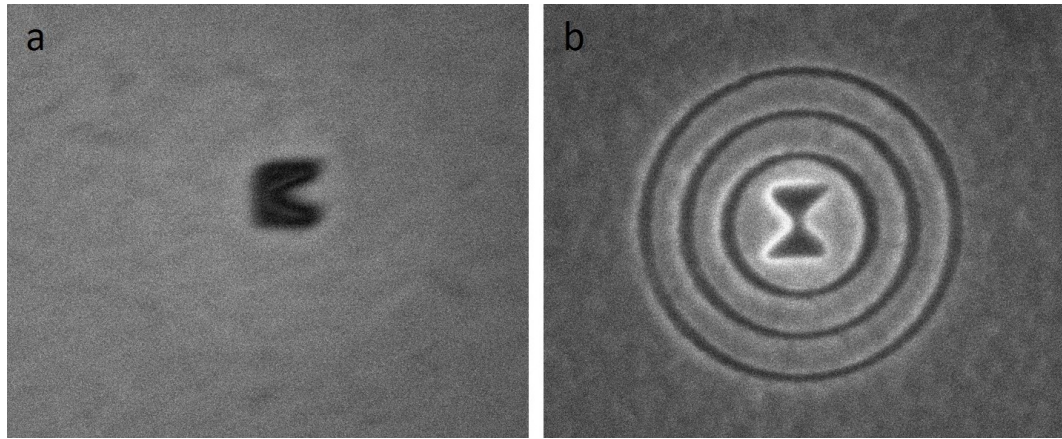


Fig. 3.2. SEM images of (a) C aperture and (b) bowtie aperture with concentric rings fabricated using focused ion beam.

to remove the organic contaminations and piranha acid solution is used remove the residues. Second, a 70-nm thick chrome film is deposited on the fused silica wafer using e-beam physical vapor deposition tool. The deposition rate of Cr is chosen to be 2 \AA/s to get a smooth surface. The FIB is used to mill the plasmonic lens with

10-pA ion current. A 12-nm gold film is deposited on top of the chrome layer as the electron emission material.

Other designs of plasmonic lenses are fabricated and shown in Figure (3.2). Figure (3.2)(a) shows the C aperture and (b) shows the bowtie aperture with concentric rings fabricated using the FIB. The C aperture has the benefit of a single hot spot and the bowtie aperture with concentric rings has a better light focusing efficiency and thus a higher quantum efficiency of electron emission.

Table 3.1.
The recipe of fabricating bowtie aperture using FIB.

No. Fabrication Step

- 1 Clean fused silica wafer with toluene, acetone and IPA.
- 2 Clean fused silica wafer with piranha acid solution.
- 3 Deposit 70-nm thick Cr film onto fused silica wafer using e-beam physical vapor deposition (PVD) tool.
- 4 Use FIB to mill the bowtie aperture with 10-pA source current.
- 5 Deposit 12-nm thick Au film onto fused silica wafer using e-beam physical vapor deposition (PVD) tool.

The focused ion beam milling method is easy to use however the throughput is very slow. In order to make a large number of plasmonic lenses such as one million of bowtie apertures, the FIB is too slow to be used. I developed another recipe of making plasmonic lenses using electron-beam lithography and lift-off method. Figure (3.3) shows the fabrication results using EBL and liftoff recipe. Figure (3.3)(a) shows the patterned negative EBL resist hydrogen silsesquioxane (HSQ). The negative resist

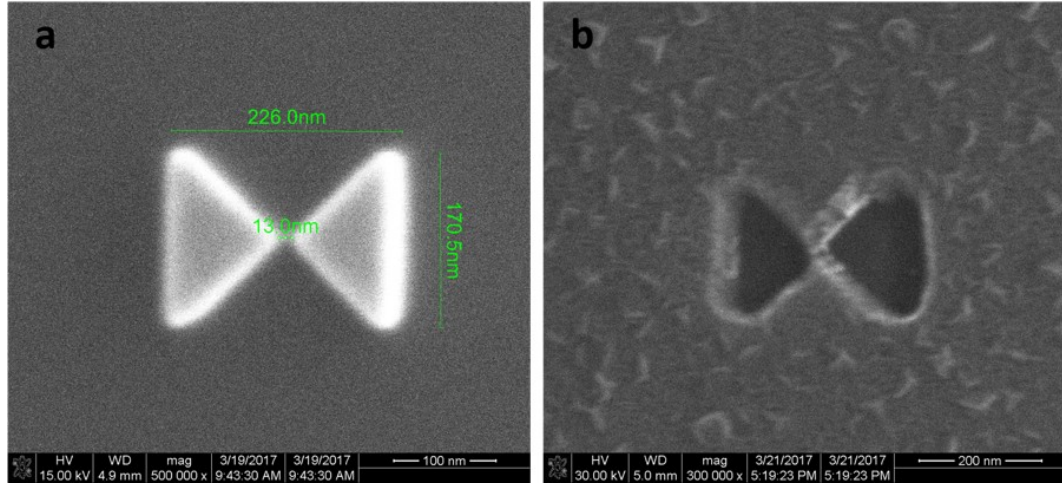


Fig. 3.3. SEM images of the bowtie aperture fabricated using electron-beam lithography and liftoff. (a) SEM image of the patterned hydrogen silsesquioxane (HSQ). The HSQ is negative tone EBL resist which exposed area remains after development. (b) SEM image of bowtie aperture after pattern transfer using Cr deposition and liftoff.

HSQ is chosen because the patterned area is much smaller than that using positive resist (ZEP or PMMA). However, HSQ is not good for liftoff because the exposed HSQ is cross linked and hard to remove. A bilayer of HSQ/PMMA resists for negative tone lift-off process was proposed by Haifang Yang, etc [61]. The fused silica wafer is firstly cleaned using toluene, acetone and IPA. Then piranha acid solution is used remove the residue. A layer of PMMA is coated before the HSQ layer. The 950k PMMA A4 is spun with 1000 rpm and the thickness of PMMA is 400 nm. The PMMA layer is baked on a hot plate for 5 min at the temperature of 180 °C. Let the wafer cool down to room temperature. The 6% HSQ is spun from 0 to 4000 rpm within 4 s and kept at 4000 rpm for 60 s. Because of the high evaporation rate of the MIBK solvent, the acceleration rate of the spin coating is very important. The thickness of the HSQ is about 100 nm. The HSQ layer is baked at 120 °C for 4 min. HSQ is not stable at room temperature in air so it's crucial to do the electron-beam writing immediately. The EBL process patterns the negative tone resist HSQ. The dose of HSQ is 3200 $\mu\text{C}/\text{cm}^2$. The size of the triangle is 170 nm by 113 nm. The HSQ layer is developed

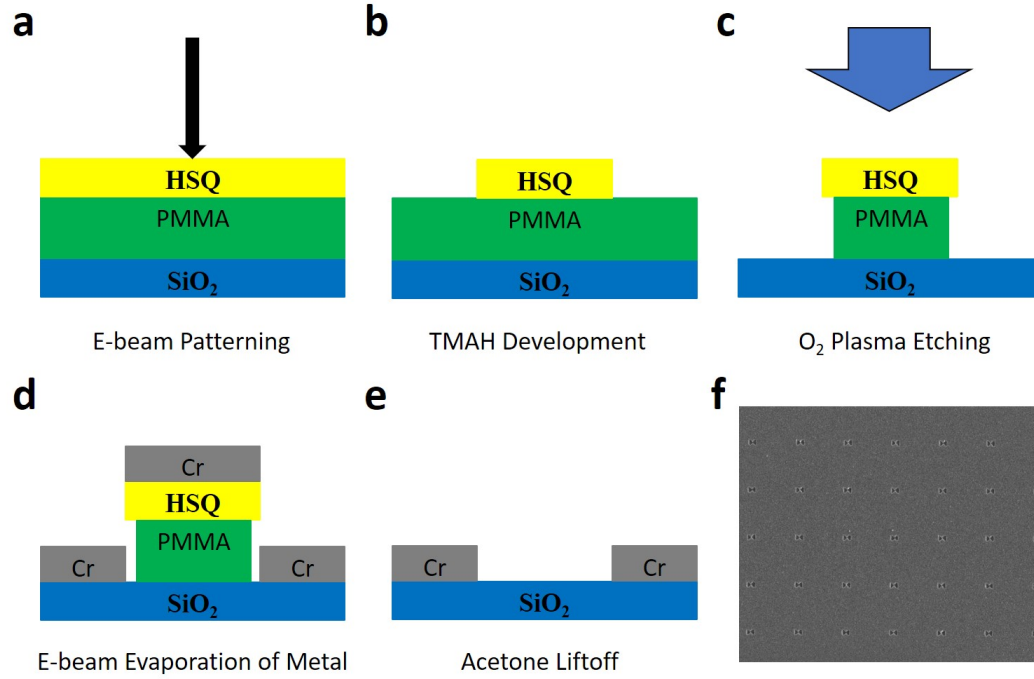


Fig. 3.4. Fabrication process of plasmonic lens using HSQ/PMMA liftoff method. (a) Clean and coat fused silica wafer with HSQ/PMMA bilayer resist. Use EBL to pattern the plasmonic lens with low current. (b) Develop HSQ with 25% TMAH for 40 s and rinse with DI water. (c) Use O₂ plasma RIE to etch PMMA. (d) Deposit 70-nm thick Cr with E-beam PVD. (e) Use acetone to do the liftoff. (f) Plasmonic lens array fabricated using HSQ/PMMA liftoff method.

with 25% TMAH for 40 s and rinsed with a lot of running DI water to reduce the residue of HSQ. If the size of the triangle is smaller, the adhesion of the HSQ pattern to the PMMA layer is not strong enough to hold the HSQ pattern which limits the aperture size. After development of HSQ, the patterned HSQ layer works as a mask for a reactive ion etching (RIE) process with O₂ plasma recipe to etch the PMMA layer. The RIE tool is the Panasonic E620 Etcher which is an inductively coupled plasma system. The flow rate of the O₂ is 30 cm²/min and the chamber pressure is 2 Pa. The RF (source) FWD power is 60 W and the RF (BIAS) FWD power is 80 W. After 2 minutes etching, the exposed PMMA layer is removed by the oxygen plasma.

The HSQ structure covered PMMA is protected. The bilayer HSQ/PMMA bowtie structures can be lifted off using acetone. The detailed recipe is listed in Table (3.2). To make one million bowtie apertures, it takes about two hour to use EBL method with 1 nA current. So it's feasible to make a multiple electron beam lithography with one million beamlets using the plasmonic enhanced photoemission source.

Table 3.2.
The recipe of fabricating bowtie aperture using HSQ/PMMA liftoff.

No. Fabrication Step

- 1 Clean fused silica wafer with toluene, acetone and IPA.
- 2 Clean fused silica wafer with piranha acid solution.
- 3 Spin coat 400-nm thick PMMA and bake at 180 °C for 5 min.
- 4 Spin coat 100-nm thick HSQ and bake at 120 °C for 4 min.
- 5 Use EBL to pattern the bowtie structures with 1 nA.
- 6 Develop HSQ with 25% TMAH for 40 s and rinse with DI water.
- 7 Use O₂ plasma RIE to etch PMMA.
- 8 Deposit 70-nm thick Cr with e-beam PVD.
- 9 Do the liftoff with two beakers of acetone.
- 10 Deposit 12-nm thick Au film.

3.2 Surface Plasmon Enhanced Photoemission

The photoemission or photoelectric effect is the emission of free electrons from materials under light illumination. It was first discovered by Heinrich Hertz in 1887 when he observed that electrodes illuminated by ultraviolet light create electric sparks more easily. This phenomenon can't be explained by the classical electrodynamics theory which leads to the discovery of the quantum concept. The photoemission process can be explained in a semi-classical three-step model proposed by Puff [26] and Spicer [27,28]. In this model, the first step is the absorption of the incident photon by an electron in the metal. The excitation rate is governed by the Fermi golden rule. The second step is the transport of the excited electron to the metal-vacuum interface. In the second step, the excited electron loses its energy through inelastic scattering and not all of the excited electrons can survive to the metal-vacuum interface. The inelastic scattering is described by the mean free path which is the averaged travel distance before the excited electron gets scattered by other electrons, phonons or defects. In the third step, some of the excited electrons overcome the work function and the energy and momentum of the electron changed abruptly across the metal-vacuum interface. During the last step, the energy is conserved and the momentum along the interface is conserved. Because of these two constraints, only a portion of the excited electrons have the chance to overcome the work function to become free electrons. The ratio between numbers of the free electrons over the incident photons is defined as the quantum efficiency (QE).

Here the bowtie aperture is chosen as an example to calculate the quantum efficiency. The shape and dimensions are shown in the previous chapter.

The photon absorption probability in the first step is calculated using a commercial finite-difference time-domain (FDTD) software CST. A linear polarized UV light is shining from the fused silica side. The polarization is along the gap direction. There is a localized gap mode to harvest the photon energy. The calculation results are presented in Figure (2.3). The field peaks at the vacuum-metal interface with an

enhanced electric field. Compared to the conventional photoemission, the absorption of photons happens at the surface within a depth of only a few nanometers. The mean free path of excited electrons with 5 eV energy is about 5 nm. The absorption coefficient of gold for 266 nm wavelength photon is $8.4 \times 10^5 \text{ cm}^{-1}$ which corresponds to a 12-nm absorption depth. This means that without the help of surface plasmon polaritons, the incident photon can penetrate the gold film by 12 nm and its distribution is the exponentially decay. Considering the small mean free path (5 nm), a large portion of the excited electrons decay along the transport to the metal-vacuum interface. The absorption ratio distribution shown in Figure (3.5)(a) and (b) show that most of the photons are absorbed within a few nanometers to the top corner of the gap. The plasmonic excited electrons are much closer to the metal-vacuum interface and it is the reason of the surface plasmon enhanced photoemission. The photon absorption probability is defined as

$$P(z) = \frac{n(z)}{\int_0^d n(z) dz}. \quad (3.1)$$

The number of electronic states at energy E_0 is $N(E_0)$ and the occupancy of those states is given by the Fermi-Dirac functions $f_{FD}(E_0)$. The Fermis golden rule dictates that the electron transition rate is given by

$$P_{exc}(E) = N(E) \cdot f_{FD}(E) \cdot N(E + \hbar\omega) \cdot [1 - f_{FD}(E + \hbar\omega)]. \quad (3.2)$$

In the second step, an assumption is made that after an electron-electron scattering, the excited electron has no enough energy to escape the work function. The scattering probability is characterized by an exponential function with the mean free path λ_{e-e} . The probability that an excited electron transports to the metal-vacuum interface without electron-electron scattering is

$$F_{e-e}(E) = \int_0^d P(z) \cdot e^{-\frac{d-z}{\lambda_{e-e}}} dz. \quad (3.3)$$

From Equation (3.3), it can be seen that the transport probability F_{e-e} is governed by the convolution of photon absorption probability $P(z)$ and the scattering decay $e^{-\frac{d-z}{\lambda_{e-e}}}$. In order to increase the transport probability, materials with large mean free path or localized plasmonic mode can be used.

In the third step, the parallel component of the wave vector of the electron is conserved across the metal-vacuum interface. While the momentum in the normal direction is reduced to overcome the work function of metal. The excited electron has energy of $E_0 + \hbar\omega$ and the energy of the freed electron outside the metal is $E_0 + \hbar\omega - E_F - \Phi$, where E_0 is the initial energy, $\hbar\omega$ is the photon energy, E_F is the Fermi energy and ϕ is the work function. The parallel component conservation of the wave vector is given by

$$\sin(\theta_m) \cdot \sqrt{2m \cdot (E_0 + \hbar\omega)} = \sin(\theta_v) \cdot \sqrt{2m \cdot (E_0 + \hbar\omega - E_F - \Phi)}, \quad (3.4)$$

where θ_m and θ_v are angles of electrons in the metal and vacuum relative to the normal direction of the metal-vacuum interface, respectively. For the maximum angle of $\theta_v = 90^\circ$, all electron trajectories inside the metal must fall within a cone to escape. The cone angle is

$$\theta_{max} = \arcsin \left(\sqrt{\frac{E_0 + \hbar\omega - E_F - \Phi}{E_0 + \hbar\omega}} \right) \quad (3.5)$$

The probability of the excited electrons has the trajectories falling in the escaping cone is given by

$$P_{esc} = \frac{1}{4\pi} \int_{\cos(\theta_{max})}^1 d(\cos\theta) \int_0^{2\pi} d\Phi. \quad (3.6)$$

The overall quantum efficiency is thus given by

$$QE(\omega) = \frac{\int P_{exc} \cdot F_{e-e} \cdot P_{esc} dE}{\int P_{exc} dE}. \quad (3.7)$$

Equation (3.7) shows that the quantum efficiency can be enhanced by using low work function material and surface plasmon polaritons. However, our vacuum cham-

ber can only achieve 2×10^{-7} mbar. To minimize the contamination of the metal surface and increase the work function, a 15-nm thick gold film is coated on the plasmonic structure. Another advantage of using gold film is that it has larger photon absorption in the UV range and can better harvest the SPP energy. The mean free path (MFP) of gold is about 5 nm [62]. The effective work function of gold (exposed to air) Φ_{eff} is from 3.7 eV to 5.1 eV [63] and the 266-nm photon energy is 4.66 eV. The effective work function is estimated to be 4.4 eV. Comparing the effective function 4.4 eV and the photon energy 4.66 eV, a flat band electron density of state is a good approximation and the P_{exc} can be treated as a constant. F_{e-e} can also be treated as constant under near the Fermi level. So the quantum efficiency can be simplified as

$$QE(\omega) = F_{e-e} \cdot \frac{E_F + \hbar\omega}{2\hbar\omega} \left[\left(+ \frac{E_F + \Phi}{E_F + \hbar\omega} - 2\sqrt{\frac{E_F + \Phi}{E_F + \hbar\omega}} \right) \right] \quad (3.8)$$

For the bowtie aperture design, the three-step model is used to calculate the quantum efficiency shown in Figure (3.5). The map of quantum efficiency is calculated using the power loss density simulated by the FDTD EMW tool, CST. There is a 15-nm thick gold on top of the 70-nm thick chrome film to harvest the SPP energy and prevent the contamination of photoemission metal surface. The substrate is fused silica and laser wave length is 266 nm. Figure (3.5)(a) shows the absorption ratio distribution of the bowtie aperture. It is defined as the ratio of absorbed optical areal energy density through the gold layer over the incident light areal energy density from the fused silica substrate. It can be seen that the peak absorption ratio is over 2 times at the bowtie tips. This is due to the focusing effect of plasmonic lens. Figure (3.5)(b) shows the local absorption ratio distribution along the vertical direction of the bowtie plane at one of the bowtie tips. From the absorption distribution, it can be see that plasmonic lens not only focuses the light but also tunes the absorption peak location along the vertical direction. With proper design, the absorption can be tuned more towards the metal vacuum interface to lower the loss of excited electron during the transport step of photoemission. This can be explained by Equation (3.3). Figure

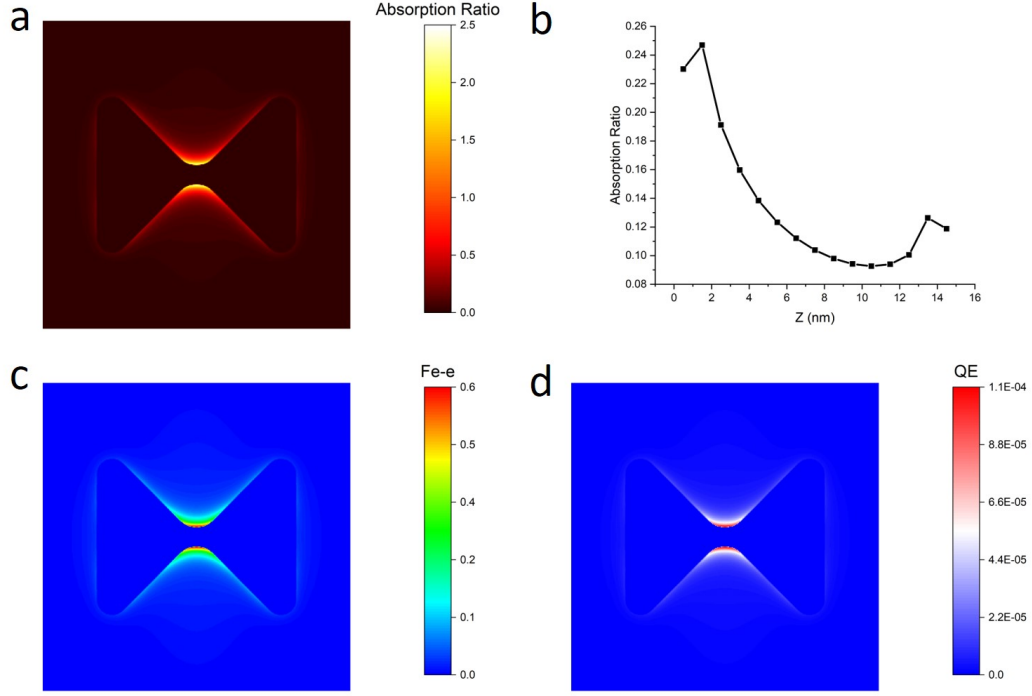


Fig. 3.5. Quantum efficiency map of bowtie aperture. The map of quantum efficiency is calculated using the power loss density simulated by the FDTD EMW tool, CST. There is a 15-nm thick gold on top of the 70-nm thick chrome film to harvest the SPP energy and prevent the contamination of photoemission metal surface. The substrate is fused silica and laser wave length is 266 nm. (a) The absorption ratio distribution of the bowtie aperture. It is defined as the ratio of absorbed optical areal energy density through the gold layer over the incident light areal energy density from the fused silica substrate. (b) The local absorption ratio distribution along the vertical direction of the bowtie plane at one of the bowtie tips. (c) Calculated F_{e-e} . F_{e-e} is the ratio of excited electrons transported to the metal-vacuum interface over the incident photons. (d) Quantum efficiency map. It is defined as the ratio of photo-emitted electron over the incident photons.

(3.5)(c) shows the calculated F_{e-e} . F_{e-e} is the ratio of excited electrons transported to the metal-vacuum interface over the incident photons calculated using Equation (3.3). Due to transport loss, the peak value of F_{e-e} is about 0.6 at the two tips. The physical meaning is that even though the absorption ratio is 2, the excited electron

transporting to the metal-vacuum interface without scattering is only 0.6 per incident photon. The thickness of the gold layer is optimized to have the largest F_{e-e} and 15 nm is chosen. Figure (3.5)(d) shows the quantum efficiency map. It is defined as the ratio of photo-emitted electron over the incident photons calculated by Equation (3.8). The two hot spots of the quantum efficiency have the value of 1.1×10^{-4} which is orders higher than planar metal film cathode shining from backside.

As for experiment, an gold film with 12-nm thickness on fused silica was firstly tested. Given the Fermi energy 5.53 eV, the QE for the 266-nm laser is calculated to be 2.80×10^{-5} and 1-mW laser generates 6.0 nA.

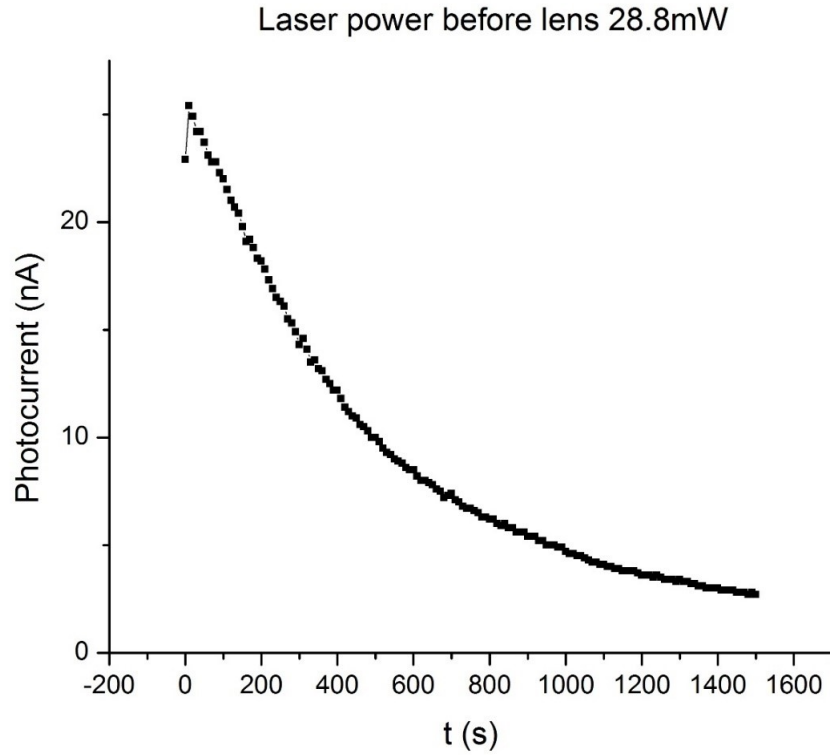


Fig. 3.6. Photoemission test of 12 nm thick gold film deposited on fused silica substrate. The vacuum pressure is 3×10^{-6} mbar. The laser beam with 266 nm wavelength is shining onto the sample from the substrate side through vacuum viewport. A UV grade viewport is used to maintain good transmission at 266 nm. The laser power is 28.8 mW before the viewport.

Figure (3.6) shows the photoemission test of 12-nm thick gold film deposited on fused silica substrate. The vacuum pressure is 3×10^{-6} mbar. The laser beam with 266 nm wavelength is shining onto the sample through vacuum viewport. The laser irradiation is from the the substrate side. The work function of pure gold is above 5 eV. But once exposed to the air, the work function of gold decreases by a few hundred meV to more than 1 eV. This is due to adsorption of water molecule on the gold surface. Numerous experiments have been performed to confirm this effect [63]. The laser power used is 28.8 mW. The measured value is 26 nA at peak. From the measured curve, we can see that life time (defined as $1/e$ of the peak value) of the photoemission is about 500 s which is too short for real application. The reason for this fast decay is that the UV photon interacts with the water molecule and increases the work function.

In order to enhance the QE of photoemission, a Cs dispenser is used to evaporate Cs atoms on the bowtie aperture to lower the work function. The work function of Cs is only 1.95 eV in ultra-high-vacuum environment (vacuum pressure lower than 10^{-9} mbar). Our current vacuum chamber can only achieve a pressure of 10^{-7} mbar so the Cs film is contaminated quickly after deposition because its so active. But it still helps to increase the QE of the photoemission.

Figure (3.7) shows the photocurrent test of 81 bowtie apertures. 81 bowties apertures are fabricated using the FIB recipe (Table (3.1)). The laser has a beam of power of 75 mW and 500 μm beam diameter. The laser power intensity shining on the plasmonic sample is 3.82 MW/m^2 . The fabricated bowtie aperture sample is brought to chamber and exposed to the air during the transport. The Cs dispenser is mounted inside the chamber. When the chamber pressure is about 10^{-6} mbar, the Cs dispenser is heated with 3 A for 60 s to deposit a thin film onto the bowtie apertures. The vacuum pressure increases and drops back to 3.8×10^{-6} mbar after the Cs deposition. A voltage of 100 V is applied to accelerate the photoelectrons. The gap between the bowtie apertures and the silicon anode is set at 34 μm . The photocurrent curve shows that the after 10 min activation, the photocurrent stabilizes

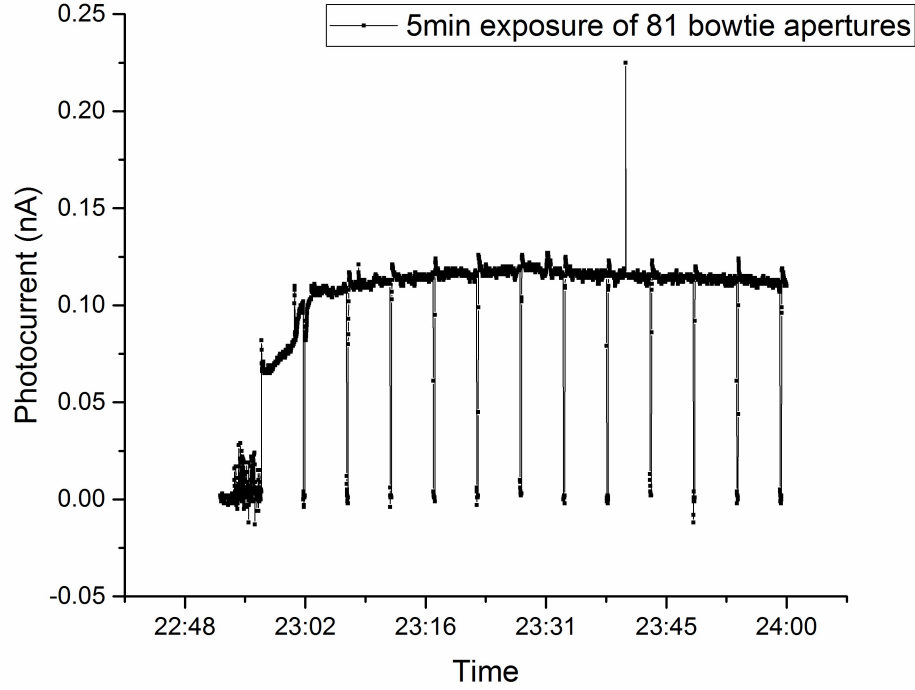


Fig. 3.7. Photocurrent test of 81 bowtie apertures. The laser has a beam of power of 75 mW and $500\mu\text{m}$ beam diameter. The vacuum pressure is $3.8 \times 10^{-6}\text{ mBar}$. The Cs dispenser is heated with 3 A for 60 s to deposit a thin film onto the bowtie apertures. A voltage of 100 V is applied to accelerate the photoelectrons. The gap between the bowtie apertures and the anode is set at $34\mu\text{m}$.

at about 1.25 pA per bowtie aperture. The drift and standard deviation is shown in Table (3.3). The photocurrent starts from 1.37 pA, peaks at 1.47 pA and falls to 1.38 pA. The fluctuation in the 5 min duration is a few percent.

The work function of the Cs coated gold film is unknown, so it is calculated backward from the photocurrent measurement. The 266-nm laser power is $0.258\mu\text{W}$ within the 260 nm by 260 nm area, so the quantum efficiency over the entire bowtie aperture $QE_{overall} = \frac{1.4\text{pA} \times 4.661\text{eV}}{0.258\mu\text{W}} = 2.53 \times 10^{-5}$. From simulated results of bowtie aperture resonance shown in Figure (3.5)(d), the work function is calculated to be 3.93 eV which is much higher than the reported 1.6 eV work function of gold

Table 3.3.
Photocurrent drift and fluctuation.

| Laser on Time | Mean of Photocurrent (pA per bowtie aper- ture) | Standard Deviation of Photocurrent (fA per bowtie aperture) |
|----------------------|--|--|
| 10 - 15 min | 1.37 | 39.8 |
| 15 - 20 min | 1.41 | 24.9 |
| 20 - 25 min | 1.43 | 25.9 |
| 25 - 30 min | 1.44 | 80.6 |
| 30 - 35 min | 1.47 | 36.8 |
| 35 - 40 min | 1.43 | 22.6 |
| 40 - 45 min | 1.42 | 133 |
| 45 - 50 min | 1.41 | 19.9 |
| 50 - 55 min | 1.40 | 18.9 |
| 55 - 60 min | 1.38 | 25.8 |

coated with submonolayer Cs [64]. This is due to the contamination of the metal surface. Substituting the Cs treated work function of 3.93 eV to the work function map calculation shown in Figure (3.5)(d), the peak quantum efficiency at the tips increased from 1.1×10^{-4} to 8.9×10^{-4} but at the cost of broader initial photoelectron energy distribution.

3.3 Test of Plasmonic Electron-Beam Source

Besides the photocurrent per bowtie aperture, the electron-beam source size is another key feature in the system. A proximity lithography is used to measure the electron-beam source size of the bowtie aperture. Figure (3.8)(a) shows the schematic of the proximity lithography system. The SPEP (bowtie aperture) array are pattern

on a 70-nm thick Cr film. The 70-nm thick film is chosen to block the 266-nm laser to avoid exposure caused by UV photons. Chrome is chosen to utilize its good mechanical property and to avoid damaging the sample during lithography operation. The substrate is a UV grade fused silica substrate with a center island. The center island is $35\text{ }\mu\text{m}$ by $35\text{ }\mu\text{m}$ large with the height of $10\text{ }\mu\text{m}$. And the bowtie aperture array are patterned on the top surface of the island. This ensures the electrons generated from the bowtie apertures are at proximity to the underneath silicon wafer. The island is created by wet etch process. The etch mask is made of AZ1518 with the adhesion promoter and patterned using standard optical lithography. The wet etchant is buffered oxide etch solution which comprises a 7:1 volume ratio of 40% NH_4F in water to 49% HF in water. The etching takes about 100 min and stirring should be applied to improve the etch quality. The silicon wafer coated with a layer of 100-nm thick PMMA is put underneath the island. There are 8 pairs of ISPI gratings on the fused silica substrate to detect the gap. A bias voltage is applied across the gap to accelerate the photoelectrons. Figure (3.9) shows the fabricated island with bowtie aperture array. There is some peeling-off on the island edge after the proximity experiment but it does not affect the bowtie aperture array. Figure (3.8)(b) shows the physical process of the proximity lithography. First, the 266-nm UV laser is shining from the substrate onto the bowtie aperture array where the surface plasmon polaritons are excited and focused to the nanoscale hot spots. The photon energy is absorbed by electrons in the metal and some of the excited hot electrons transport to the metal-vacuum interface and overcome the work function to become free electrons. Using the gap control system, the gap between the bowtie aperture and the underneath silicon wafer is controlled within a few nanometers to avoid the scattering of electrons with air molecules. A bias voltage is applied between the plasmonic lens layer and the silicon wafer to accelerate the electrons and guide them to cut the PMMA molecule chain. The bias voltage is ranging from 20 V to 50 V and 50 V has the best lithography results. Then the PMMA is developed using MIBK. The

exposed pattern is a one to one mapping of the electron source and the results are shown in Figure (3.10).

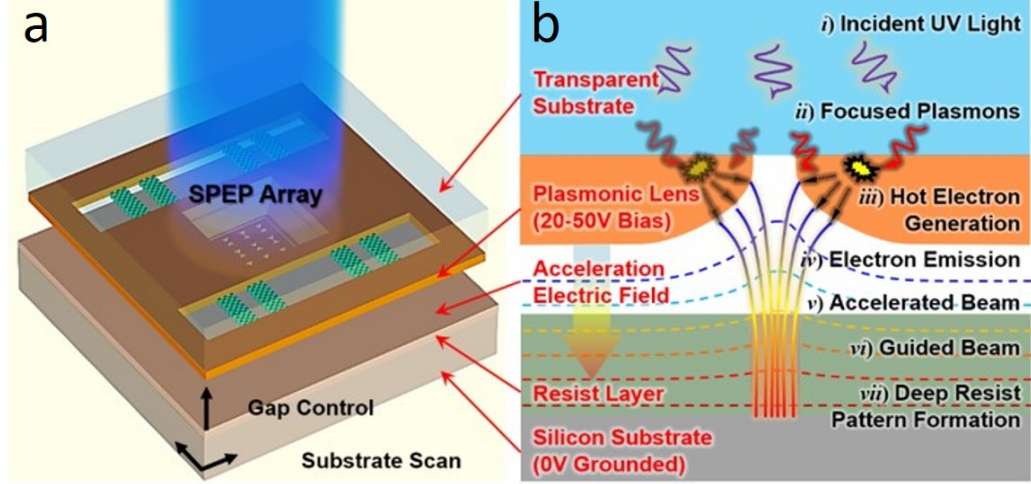


Fig. 3.8. The proximity lithography system using plasmonic electron-beam source. (a) The schematic of the system setup. (b) The physical process of the proximity lithography. There are six steps of the process. i) Incident UV light. ii) Focused plasmons. iii) Hot electron generation. iv) Electron emission. v) Accelerated beam. vi) Guided beam. vii) Deep resist pattern formation.

A laser beam with intensity of 0.4 MW/m^2 is irradiating on the bowtie apertures. After one hour irradiation, the electron-beam source is imaged onto the PMMA resist. The AFM image of the developed PMMA resist is shown in Figure (3.10). The PMMA is not sensitive to UV photons with wavelength larger than 248nm. The exposed pattern is from the photoelectrons accelerated by the bias voltage. This is justified by the depth of the pattern. The evanescent wave nature of the SPPs limits the depth of the optical exposure to be less than 30 nm [7], but the exposed depth is over 75 nm here. This can only be explained by the photoemission exposure. The bowtie aperture hot spots are shown in the PMMA resist in Figure (3.10)(a). The spacing between two bowtie apertures are $5 \mu\text{m}$. Figure (3.10)(b) shows the profile of the exposed pattern at the bowtie tip. The blue and red curves correspond to trace

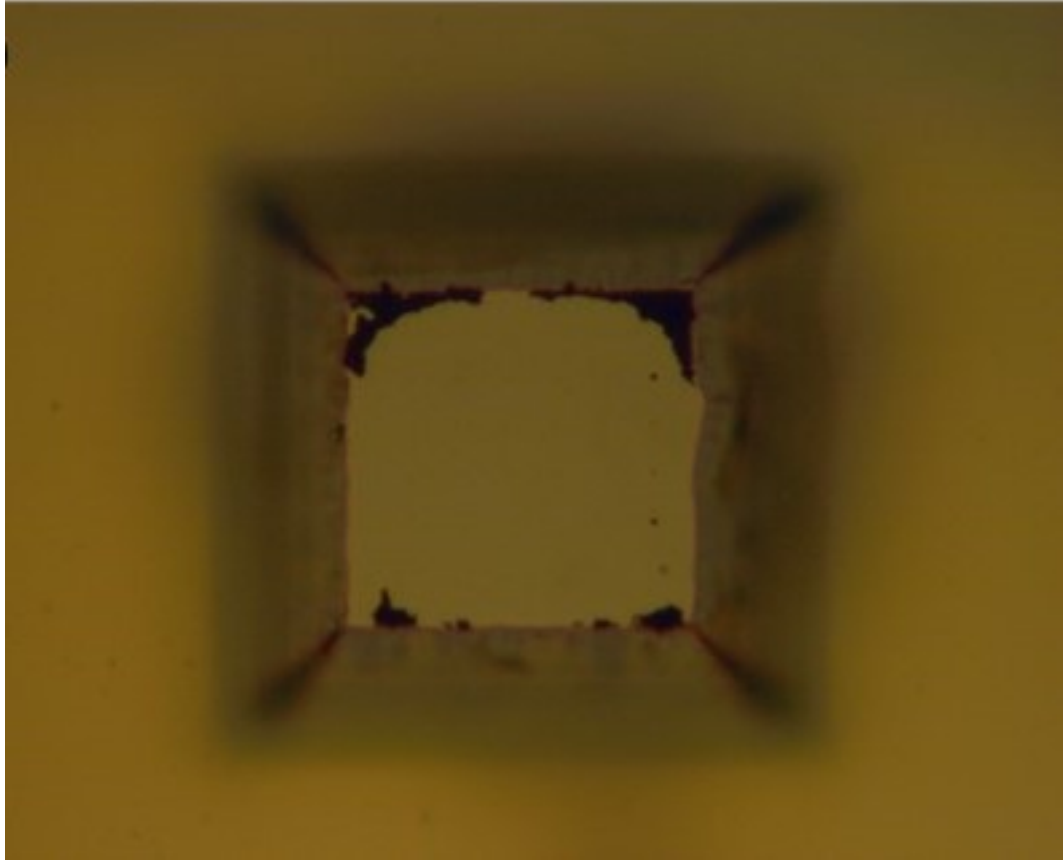


Fig. 3.9. The microscopic image of the island with bowtie apertures. The substrate is quartz and a center island with $10\text{ }\mu\text{m}$ height is fabricated to reduce the contact area. The top surface of the island has an area of $35\text{ }\mu\text{m}$ by $35\text{ }\mu\text{m}$. The bowtie apertures are milled on the 70 nm thick Cr film on top of the island.

and retrace scan of the AFM tip. The full width at half maximum (FWHM) is about 20 nm and the exposed depth is over 75 nm . The difference between the trace and retrace signal shown in (b) is attributed to large scanning speed of the AFM tip.

These photocurrent and electron-beam source size results demonstrate that the plasmonic enhanced electron-beam source is feasible and suitable for the multiple electron-beam lithography tool. The photocurrent yield and stability can be greatly improved by using ultra high vacuum systems. Here the bowtie aperture is chosen as

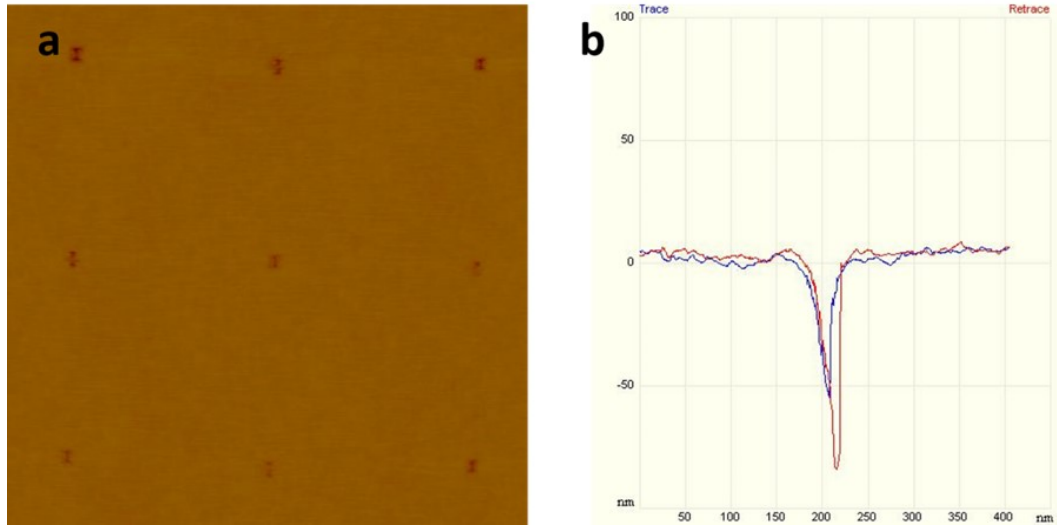


Fig. 3.10. The AFM image of the developed PMMA resist after one hour irradiation of the photoelectrons from the array of bowtie apertures. A bias voltage of 50 V is applied between the bowtie apertures and the Si wafer underneath. A laser beam with intensity of 0.4 MW/m^2 is irradiating on the bowtie apertures.

an example of plamsonic lens and other design with even better performance can be used.

4. ELECTROSTATIC LENS FOR ELECTRON-BEAM

4.1 Design and Analysis of Electrostatic Lens

In order to focus electron-beam onto the target, there are two types of electron lenses can be used [65]. One is electromagnetic lens which utilizes the Lorentz force to focus the electron-beam [66]. The other is electrostatic lens which uses only the electrostatic force [67]. They have their own advantages and applications respectively. In general, electromagnetic lens has better performance in terms of smaller aberrations, but it is cumbersome and not easy to be miniaturized. Electrostatic lens has slightly larger aberrations, but it is easier to design and fabricated at micrometer scale. In multiple electron-beam system, electrostatic lens is chosen for its potential to be fabricated in a compacted and scalable way [67–73]. Microcolumns are microscale electrostatic lenses which have practical advantages over the traditional columns because of their high resolution and compactness. They are also capable of achieving ultralow landing electron energy for some niche applications. Because of their compactness, microcolumns can be arranged into massive arrays for parallel electron-beam lithography. This massive-parallel scheme enables the use of small beam current for each microcolumn to achieve a high total beam current that exceeds the throughput of shaped beam lithography and cell-projection lithography system [74, 75]. High-throughput parallel microcolumns have attracted many interests because of their potentials in the applications of electron-beam lithography and imaging. In the past two decades, researchers have developed a variety of miniature electron-beam columns [67, 68, 76–81]. Most of these prototypes utilized the conventional Schottky emitter with high operation temperature (about 1800K), but thermal issues become the biggest obstacle in its development [82]. The use of carbon nanotubes (CNTs) as electron emitters was proposed to replace Schottky emitters;

however, there is still no practical approach to fabricate the CNT emitters with the desired consistency and uniformity [83].

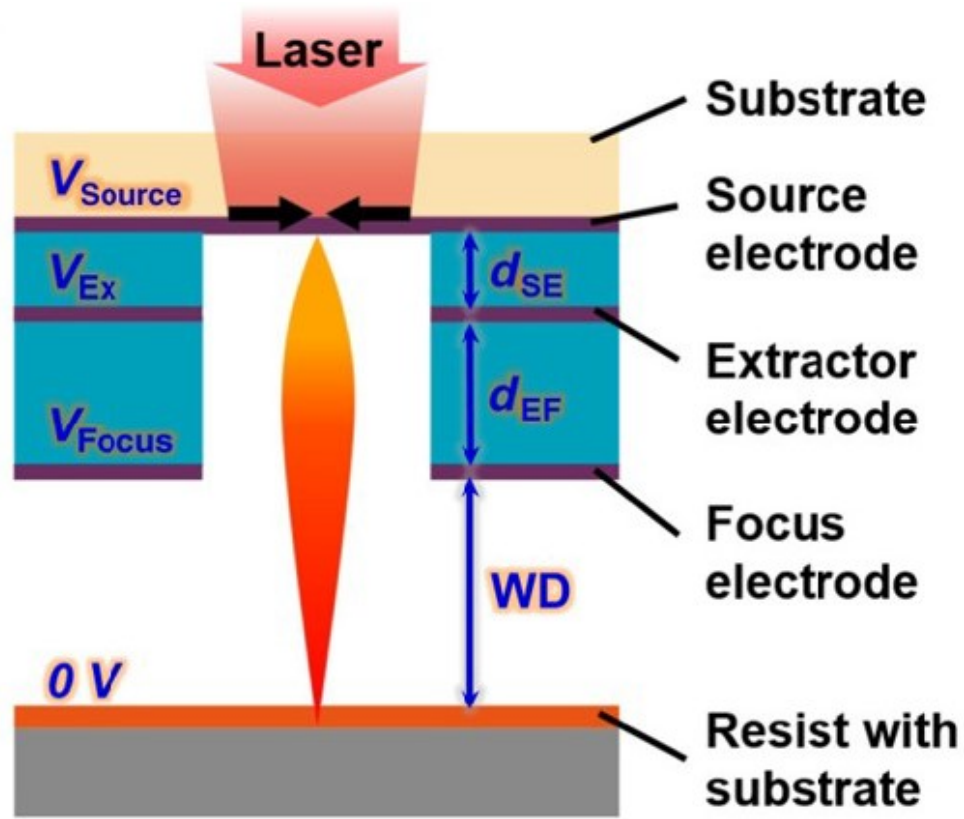


Fig. 4.1. The electrostatic microcolumn: schematic of the components and parameters. The system is composed of three electrodes. The plasmonic lens is fabricated on the source electrode where the electrons are generated by plasmonic enhanced photoemission. The extractor and focus electrodes are accelerating and focusing the electrons onto the silicon wafer underneath. The gap between the focus electrode and the silicon wafer is called working distance (WD).

An electrostatic microcolumn for the nanoscale photoemission sources is designed. A compact column structure is proposed (as short as several microns in length) for the ease of microcolumn fabrication and lithography operation shown in Figure (4.1). There are three metallic layers: the source layer, the extractor layer and the focus layer. The photoemission source is fabricated on the source layer. During the oper-

ation, the plasmonic lens array are back-illuminated by a laser beam and generate a nanoscale beam of photoelectrons, which will be accelerated and focused into a Gaussian spot by the microcolumn. The silicon wafer is grounded and the electric potential of the source electrode is V_{Source} which is lower than the ground. A higher potential V_{Ex} is applied to the extractor electrode to accelerate the electrons and a lower potential V_{Focus} is applied to the focus electrode to decelerate and focus the electron beam onto the silicon wafer. The focal length can be changed by adjusting the potentials of the three electrodes. Compared with the traditional microcolumn, the blanking of the beam can be easily achieved by modulating the incident laser beams which can be achieved using Digital Micromirror Device (DMD); therefore, the electron beam blanker is not needed, which not only significantly reduces the complexities of the fabrication and operation process but also reduces the power consumption by the blanker.

We studied the geometry scaling of a microcolumn design as illustrated in Figure (4.1). While keeping the electrode voltages and photocathode size unaffected, all geometric parameters of the microcolumn are presented in a scaling factor using a dimension L_0 , where L_0 is the distance between source and extractor. As shown in Figure (4.1), the source voltage was fixed at -900 V (V_{Source}), and a bias potential was applied to the extractor electrode of -800 V (V_{Ex}). The focus voltage was optimized, which is approximately -954 V (V_{Focus}), and the resist substrate was grounded (0 V). All electrodes were electrostatic apertures with a diameter of $3 L_0$. The distances between the source and the extractor and between the extractor and the focus electrode are L_0 and $2.5 L_0$, respectively. The thickness of each electrode was $0.1 L_0$. The working distance (WD), which is the distance between the bottom of the focusing electrode and the surface of the resist, was fixed at $5 L_0$ in the following discussion unless otherwise specified here. The overall column length was about $9 L_0$, which is the total distance from source location to resist surface. The column was designed with a demagnification factor of 0.4. Applied voltages and the structure of electron optics (the aperture diameter, the electrode thickness, and so on) can influence and

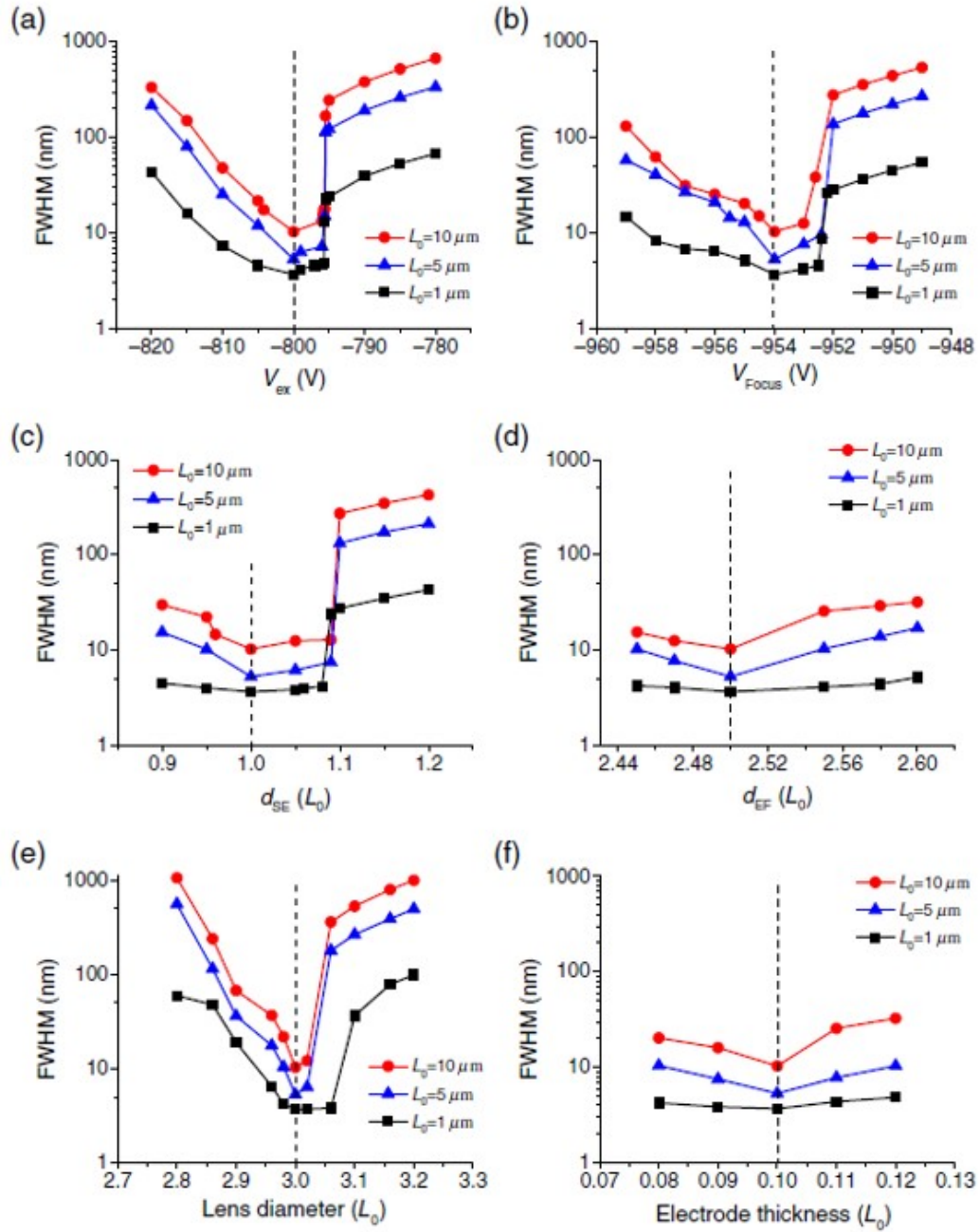


Fig. 4.2. The scaling capability and the dependence of spot size in FWHM on (a) extraction voltage, (b) focusing voltage, (c) distance between source and extractor, (d) distance between extractor and focusing electrode, (e) aperture diameter, and (f) thickness of each electrode. Dashed lines label the optimized parameter values.

determine the performance of final probe beam. Thus, it is necessary to evaluate and analyze the influence on the characteristics of the spot size.

Figure (4.2) shows the resolution dependence for three different scaling factors when varying one design parameter and fixing all others parameters at their optimized values. Influences of different design parameters on the resolution are shown in $L_0 = 1$, 5, and 10 μm , where a constant source size of 10 nm in diameter is maintained when scaling the column size. The obtained results help to examine the manufacturing tolerances and operational parameters of the column designs to meet the desired resolution of 16-nm FWHM beam size. Our simulation indicates that a few percent of variation in dimensions will be acceptable for manufacturing such a microcolumn, which is possible to achieve using state-of-the-art tools. As shown in Figure (4.2), the optimized spot size increases as the microcolumn is scaled up. Although scaling up can provide a safer field strength in the insulators, the changes of resolution become more sensitive to the variation of design parameters. The case of $L_0 = 1 \mu\text{m}$ is explained here to understand the performance dependence on these parameters. As shown in Figure (4.2)(a) and (b), maintaining the voltage between -804.5 V and -795.5 V for extractor and a voltage between -955.6 V and -952.4 V for the focusing electrode is necessary to maintain a spot size smaller than 16 nm. As shown in Figure (4.2)(c) and (d), a tolerance of 80 nm for the distance between source and extractor and a tolerance of 200 nm for the distance between extractor and focusing electrode are acceptable to maintain the spot size smaller than 16 nm. Figure (4.2)(e) and (f) suggest that the aperture diameter needs to be kept to be 3 μm with a variation of 40 nm while the thickness of each electrode does not have significant effects on the performance. When fixing the source size at 10 nm, the optimized design for the cases of $L_0 = 5$ and 10 μm is listed in Table (4.1). During the geometry scaling, the values of optimized parameters scale accordingly but the performance trends to become relatively more sensitive to the same fraction of variations for most of the parameters. These fabrication and operation tolerances are likely affected by the convolution effect between the optical aberrations and the finite source size. In all

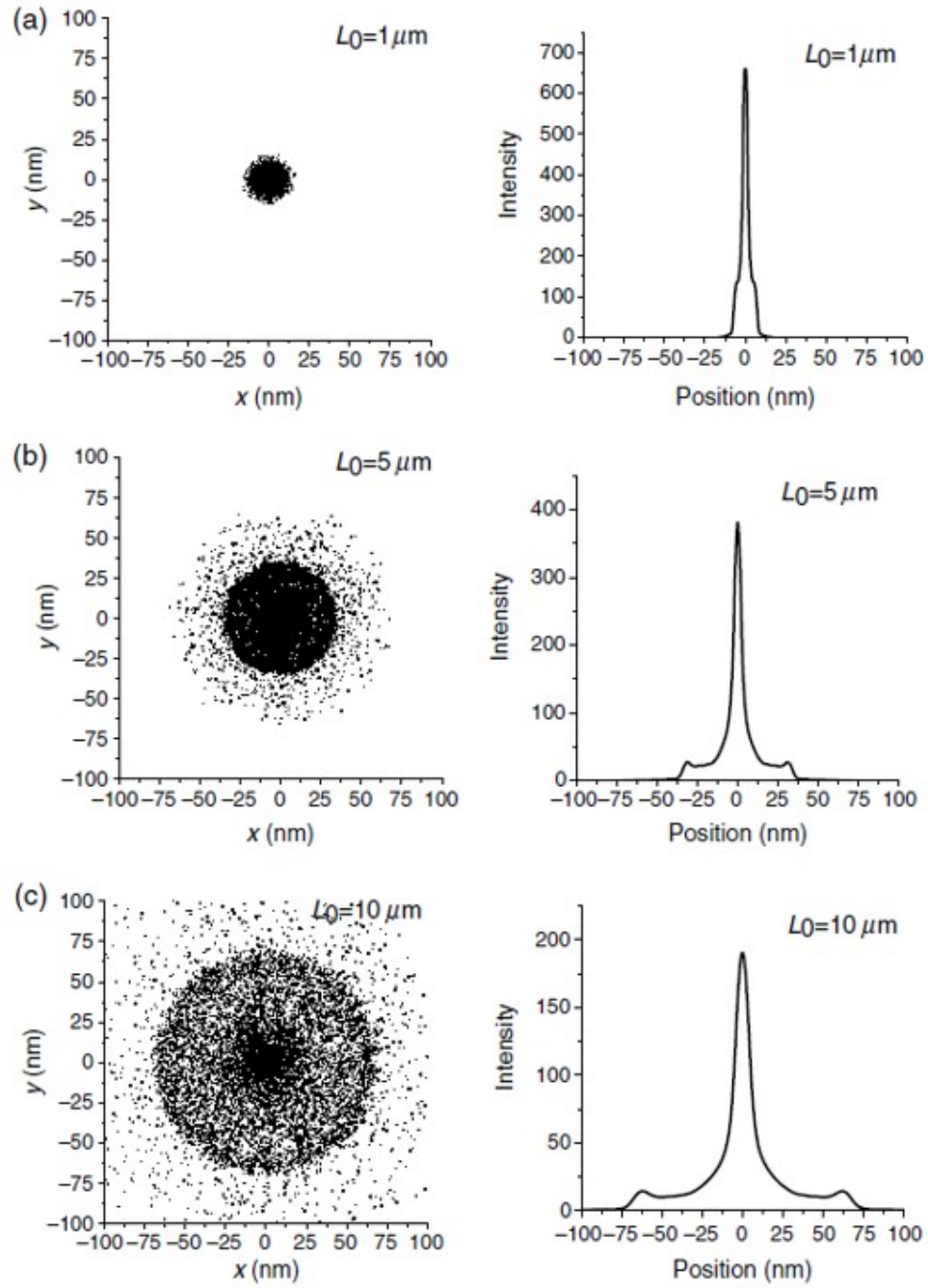


Fig. 4.3. Spot diagram of the microcolumn with 10-nm-diameter source. The size in full-width half-maximum is (a) 3.69 nm for $L_0 = 1 \mu m$, (b) 5.32 nm for $L_0 = 5 \mu m$, and (c) 10.34 nm for $L_0 = 10 \mu m$.

simulations, the initial energy spread is set to be uniformly distributed from 0.1 to 0.2 eV, and the initial emitting angle with respect to the optical axis is from 0 deg to 90 deg, which are typical for typical photocathodes. In these simulations and the following simulations, we use a commercial electron-optical design software SIMION (version 8.1) to calculate the electrical potential and simulate the electron trajectories. In the case of $L_0 = 1 \mu m$, the optimized focus voltage was determined to be -954 V at a WD of 5 μm . The electric-field strength of this design is around 190 V/ μm for the case of $L_0 = 1 \mu m$, which is demanding but still safe if high-quality dielectric materials such as fused silica are chosen as the insulators [84].

Table 4.1.
Optimized design parameters of microcolumn.

| Parameters | Case 1 | Case 2 | Case 3 |
|---------------------------------------|----------------|----------------|----------------|
| L_0 | 1 μm | 5 μm | 10 μm |
| Initial energy (eV) | 0.1 to 0.2 | 0.1 to 0.2 | 0.1 to 0.2 |
| Launch angle of electron source (deg) | 0 to 90 | 0 to 90 | 0 to 90 |
| V_{source} (V) (fixed) | -900 | -900 | -900 |
| $V_{extractor}$ (V) | -800 \pm 4.5 | -800 \pm 4.4 | -800 \pm 4.2 |
| V_{focus} (V) | -954 \pm 1.6 | -954 \pm 1.5 | -954 \pm 0.5 |
| V_{ground} (V) | 0 | 0 | 0 |
| d_{SE} (μm) | 1 \pm 0.08 | 5 \pm 0.45 | 10 \pm 0.40 |
| d_{EF} (μm) | 2.5 \pm 0.2 | 12.5 \pm 0.1 | 25 \pm 0.3 |
| Aperture Diameter (μm) | 3 \pm 0.04 | 15 \pm 0.1 | 30 \pm 0.2 |
| Thickness of electrodes (nm) | 100 | 500 | 1000 |

The optimized beam profiles on the resist surface results using parameters in Table (4.1) are shown in Figure (4.3) under three scaling factors. To achieve prac-

tically high-lithography throughput, large landing beam currents are desired. However, extremely large beam current will cause noticeable electron-electron interaction (Coulomb interaction). The image blur due to Coulomb interaction increases with beam current, optical column length, and demagnification but decreases with convergence angle, source size, and acceleration voltage [74]. The Coulomb interaction can be negligible by distributing the total beam current among microcolumn array, reducing microcolumn length and source size and increasing the acceleration voltage and so on.

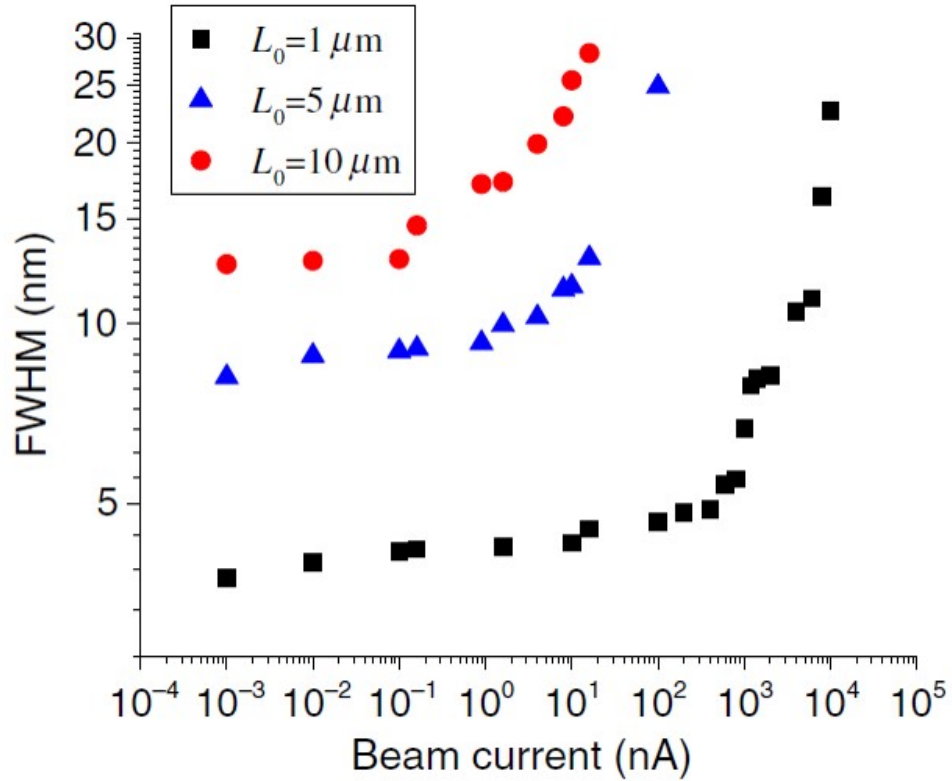


Fig. 4.4. Electronelectron interaction simulation of single column. The spot size was plotted as a function of the beam current. The microcolumn is capable of keeping the spot size variation smaller than 10% over a large current range.

In Figure (4.4), all optimized parameters in Table (4.1) are applied and the figure shows the effect of beam blur induced by Coulomb interaction using a 10-nm-diameter

source. It is shown that the microcolumn can operate at a large beam current reaching tens of nanoamperes without noticeable beam blur for $L_0 = 1\ \mu\text{m}$ and the current limit reduces to several nanoamperes and hundreds of picoamperes for $L_0 = 5\ \mu\text{m}$ and $10\ \mu\text{m}$, respectively. The source voltage of $-900\ \text{V}$ was fixed in investigating the intercolumn interaction.

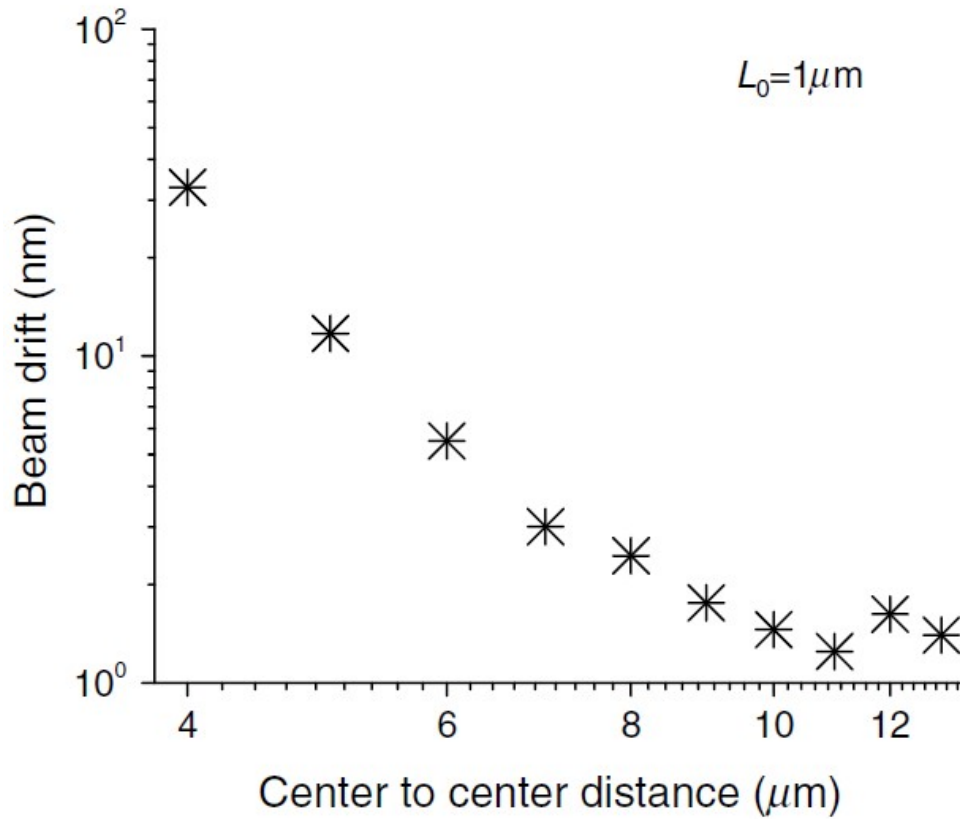


Fig. 4.5. Dual-column interaction with different aperture center-to-center distances for $L_0 = 1\ \mu\text{m}$. It shows that a minimum spacing of $12\ \mu\text{m}$ can safely avoid the field distortion effect from the adjacent microcolumns.

Although electron-beam direct writings using microcolumns provide a superb lithography resolution, the low throughput is the main obstacle in their applications. Using a massive number of microcolumns in parallel can largely increase throughput. Many efforts have been devoted to developing microcolumn arrays and multiple

miniature columns to improve the throughput [1, 70, 85, 85–88]. The analysis indicates that larger number of microcolumns can provide the potential opportunity to increase throughput. However, the number of microcolumns is limited by several factors. The major one is space charge effect (Coulomb interactions); however, this can be neglected in our design if the operating beam current is well below 100 nA for each microcolumn. The second is the beam aberration and drift caused by the fringing fields of the adjacent apertures. It is important to ensure that the microcolumns are positioned far enough to minimize the intermicrocolumn interactions. To evaluate a reasonable footprint size of a 100×100 microcolumn array, we analyzed the interaction between two microcolumns with $L_0 = 1 \mu m$ at a spacing in the range of 4 to $13 \mu m$. We constructed two microcolumns in three-dimensional (3-D) model and varied their center-to-center distance while keeping their distances from the boundaries of the simulation domain to be large enough ($10 \mu m$ and larger) to minimize the boundary influence. Figure (4.5) shows the drift of the beam center caused by the fringing field from adjacent microcolumn for the case of $L_0 = 1 \mu m$. The beam drift reduces rapidly when their aperture center-to-center distance increases in the range of 4 to $8 \mu m$. As the distance further increases, the discretization errors from the 3-D model will start to take over, leading to noise floor of a few nanometers. The trend shown in Figure (4.5) indicates that the fringing field from adjacent microcolumn can be neglected when their aperture center-to-center distance is larger than $12 \mu m$. Simulations for the cases of $L_0 = 5$ and $10 \mu m$ are not performed due to compute-intensive nature of the 3-D models. We expect the beam drift to scale linearly with respect to L_0 , which would require further scaling up the center-to-center distance to a value even higher than $12 L_0$ in order to the same magnitude of beam drift.

4.2 Fabrication of Electrostatic Lens

We chose $L_0 = 1 \mu m$ as an example to demonstrate the possibility of microfabrication. The dielectric material was chosen to be SiO_2 because it can be easily etched

by reactive ion etching (RIE). To test the breakdown field, a $2\text{-}\mu\text{m}$ thick SiO_2 was deposited between two chromium layers. The Leybold E-beam Evaporator was used to deposit the SiO_2 layer at a rate of 3 angstrom per second. The breakdown voltage was measured at the pressure of 3×10^{-6} mbar. The area of the SiO_2 layer is about 1 cm^2 . The I-V curve is shown in Figure (4.6). The breakdown voltage is 635 V. Above the breakdown voltage, the current increased dramatically and was limited by the limiting resistance. The breakdown voltage of SiO_2 is above the operation voltage designed in Case 1 of Table (4.1). So the design is safe in terms of breakdown of SiO_2 .

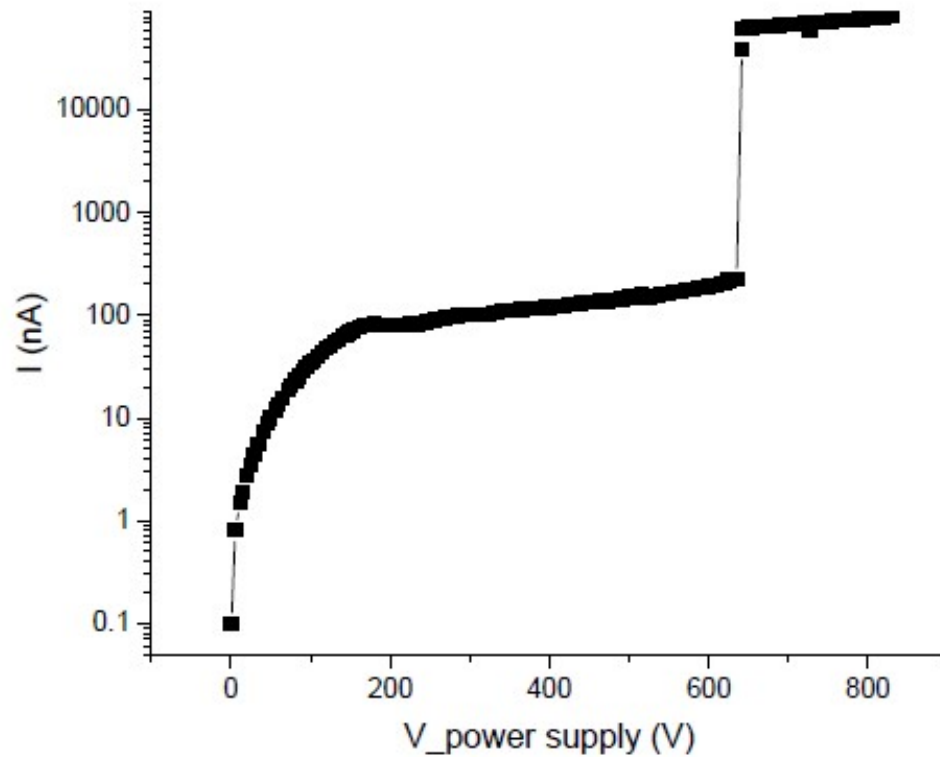


Fig. 4.6. Breakdown test of the $2\text{ }\mu\text{m}$ thick SiO_2 film. The breakdown voltage is 635 V corresponding to $317.5\text{ V}/\mu\text{m}$. Above 635 V, the current is limited by the limiting resistance.

A stack of metal and dielectric layers was fabricated by optical lithography method as shown in Figure (4.7). The source and focus layers are chromium and the extractor layer is titanium. The chrome is chosen because it has much slower etch rate than

SiO_2 in the RIE process and thus the top focus electrode works as etch mask and the bottom source electrode works as etch stop. The titanium is used because it can be easily etched in the RIE process when SiO_2 is being etched.

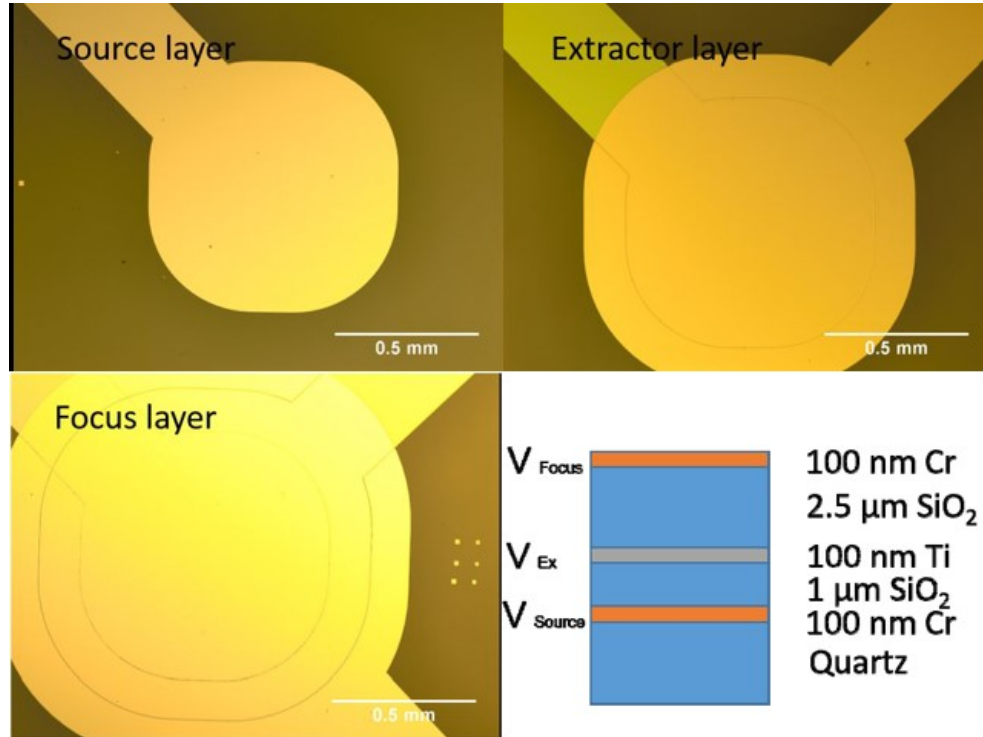


Fig. 4.7. Optical image of metal layers. The source and focus layers are chromium and the extractor layer is titanium.

The focused ion beam (FIB) tool was used to mill an array of holes into the focus layer by 400 nm depth. The diameter of the holes is 3 μm . Then we use RIE process to further etch the holes down to the source layer. The focus layer with an array of holes works as the hard mask in the RIE process. Figure (4.8)(a) is the SEM image of the array. And Figure (4.8)(b) shows the cross section view of the microcolumn. It can be seen that the hole stops right at the source layer. The diameter of the aperture of the extractor layer is smaller than that of the focus layer. The difference between apertures can be compensated by tuning the focus voltage. Actually, this tapered shape isn't worse than the straight one though it isn't easy to control. Initially the top focus layer has a thickness of 350 nm and reduces to around 100 nm during the

Table 4.2.

The recipe of fabricating microscale electrostatic lens.

No. Fabrication Step

- 1 Clean fused silica wafer.
- 2 Optical lithography to pattern the source electrode photo resist.
- 3 Deposit 100-nm thick Cr with e-beam PVD and do the liftoff.
- 4 Deposit $1\mu\text{m}$ thick SiO_2 with HDPCVD.
- 5 Optical lithography to pattern the extractor electrode photo resist.
- 6 Deposit 100-nm thick Ti with e-beam PVD and do the liftoff.
- 7 Deposit $2.5\text{-}\mu\text{m}$ thick SiO_2 with HDPCVD.
- 8 Deposit 10-nm thick SiO_2/Ti transition layer with sputtering PVD.
- 9 Optical lithography to pattern the focus electrode photo resist.
- 10 Deposit 350-nm thick Cr with e-beam PVD and do the liftoff.
- 11 Use FIB to pattern the array of holes on the focus electrode.
- 12 Use ICP plasma RIE with CHF_3 to etch the SiO_2 and Ti layers.
- 13 Use FIB to pattern the plasmonic lenses on the source layer.

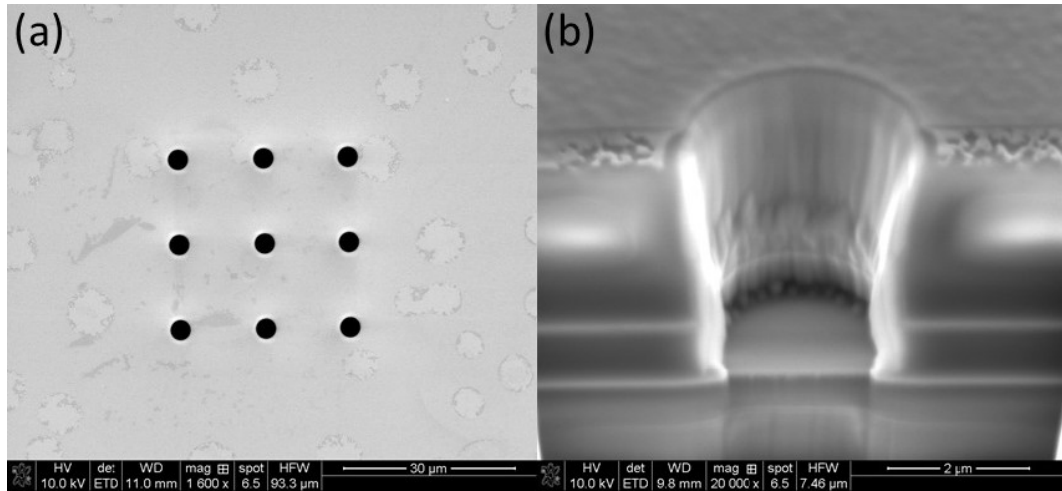


Fig. 4.8. SEM image of the fabricated microcolumn. (a) The 3×3 array with a spacing of $15 \mu\text{m}$. (b) The cross section of the microcolumn.

RIE process. The details of the fabrication recipe can be seen in Table (4.2). Figure (4.9) shows the delamination issue of the focus layer under large V_{Focus} without the transition layer in step 8 of the recipe. The cause of the delamination is large shear stress at the interface between SiO_2 and Cr films during the fabrication process. When there is a large attractive electrostatic force between the focus layer and the silicon wafer, the delamination happens. This limits how large the V_{Focus} can be and thus limits the resolution of the electron beams. To solve this issue, a transition layer made of 1:1 SiO_2/Ti is sputtered on the second SiO_2 layer first and then the focus layer is deposited. The mixture layer of metal and oxide promotes the adhesion between SiO_2 and Cr and also makes the thickness of the metal-oxide interface increases from single atom to 10 nm which greatly reduces the stress. Before applying the transition layer, the delamination happens when the electric field across the WD is larger than $4 \text{ V}/\mu\text{m}$. If the focus layer is at -120 V , the working distance has to be larger than $30 \mu\text{m}$ but the electron optics at this WD operates in a magnifying mode. This magnification is about X3.5 and is not good for getting a small electron beam spot on

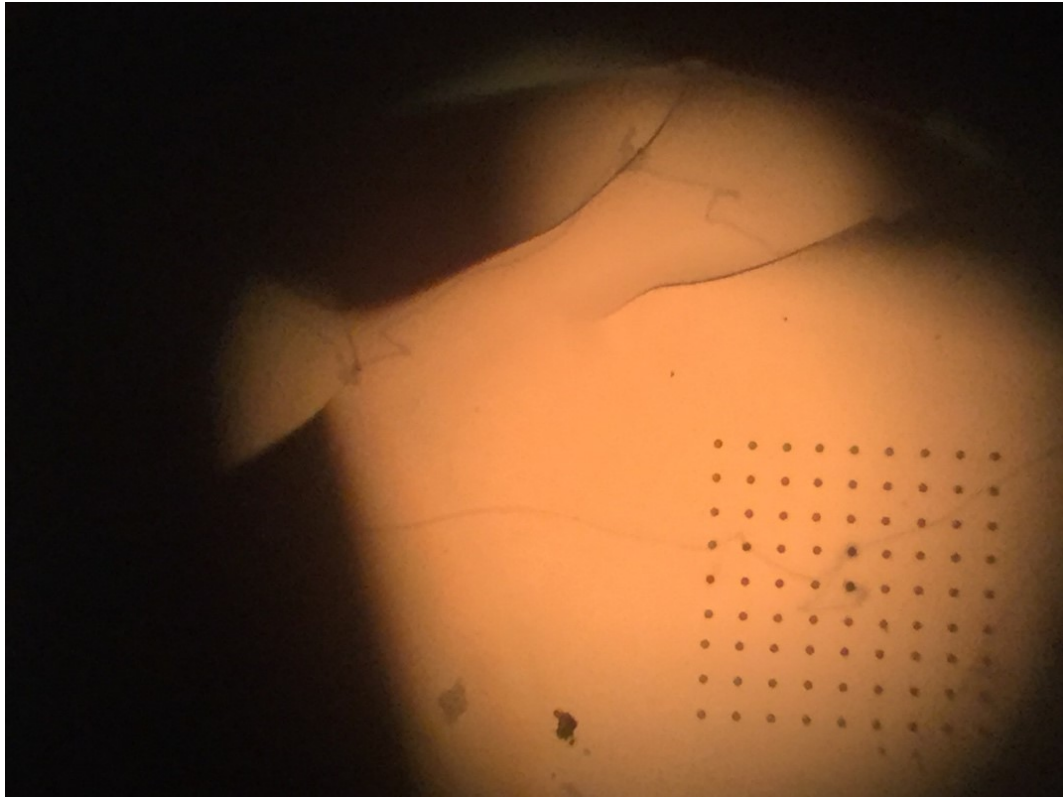


Fig. 4.9. Delamination of the focus layer due to interface stress and electrostatic force.

the silicon wafer. Once the transition layer is used, the delamination issue is solved and V_{Focus} can be -260 V with WD of $10\ \mu\text{m}$ without seeing any delamination.

5. MULTIPLE ELECTRON-BEAM LITHOGRAPHY SYSTEM

As a proof of concept, a simplified surface plasmon enhanced photoemission multiple electron-beam lithography system is designed. Figure (5.1) shows the schematic of the multiple electron-beam lithography system. The system is composed of plasmonic enhanced multiple electron-beam source, microscale electrostatic lens array, high voltage module, nano-positioning stage, vacuum system and control systems.

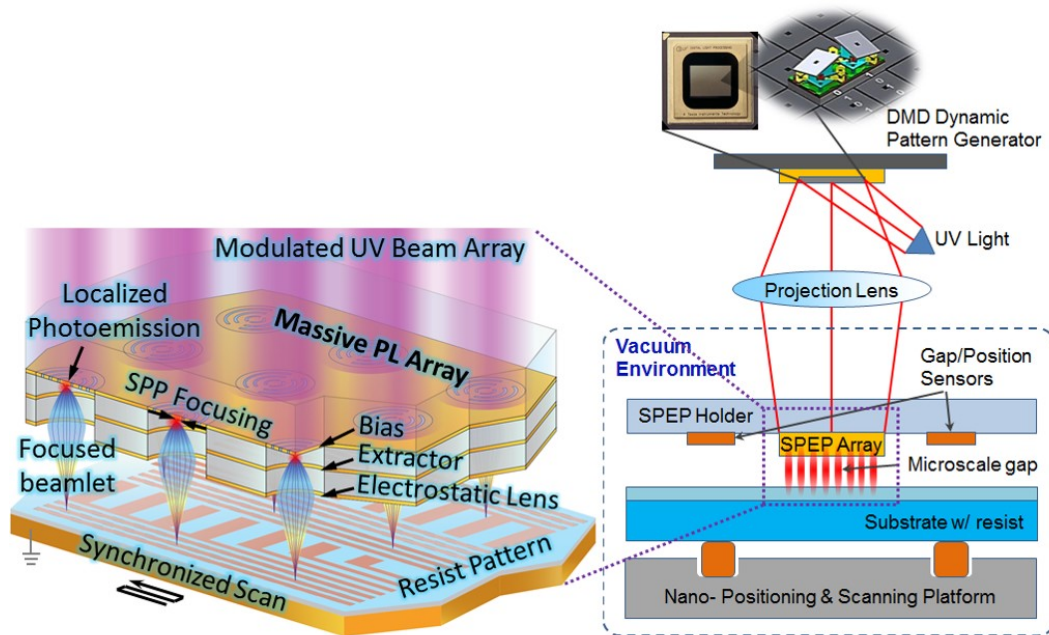


Fig. 5.1. Illustration of the surface plasmon enhanced photoemission multiple electron-beam lithography system first-stage engineering system using plasmonic lenses (PLs).

The plasmonic enhanced multiple electron-beam source is made of individually controllable UV light beam array, UV light projection lens and the SPEP array where plasmonic enhanced electrons are generated. The UV light source is a 200-mW CW

laser with 266-nm wavelength. Then the laser beam is expanded and shining onto an array of microscale optical lenses and thermally actuating shutter array to generate an array of individually controllable UV beams. The switching of the individual electron beam is controlled by switching the individual UV beam. The UV light beam is first focused by the plasmonic lens to a nanoscale hot spot which goes beyond the light diffraction limit. The hot spot then generates localized plasmonic enhanced photoemission as the electron source. As proof of concept, the UV light beam array is not included in the system and an expanded UV light beam is directly shining onto the SPEP array and a mechanical shutter is used to switch the UV light beam on and off.

The microscale electrostatic lens array is fabricated using micro- and nano-fabrication technique as described in previous chapter. The electron lens is made of three electrodes: the source, extractor and focus electrodes. The underneath silicon wafer is grounded and the electron landing energy is set by the negatively biased source electrode. The electrons generated by the plasmonic lens are accelerated by the extractor electrode where a higher electric potential is applied. The divergence angle of the electron beams is decreased by this accelerating potential. Then the electrons will be decelerated by the focus electrode where a lower electric potential is applied. The divergence angle of the electron beams is further decreased and eventually the angle becomes convergence and focused at the focal point. By tuning the electric potential of the focus electrode, the focal point of the electron optics is adjusted onto the silicon wafer.

The high voltage module is designed and made. The reference voltage is used to control the output high voltage. The reference voltage ranges from 0 to 10 V and corresponds from 0 to 1 kV for the high voltage output. There are three channels available for V_{Source} , V_{Ex} and V_{Focus} . To reduce the noise, a low pass filter circuit is added to each channel and the noise of the output is measured to be 5 mV. The reference analog signals are given from the control system and the output high voltages are given to the electrodes of microscale electrostatic lenses through the electric

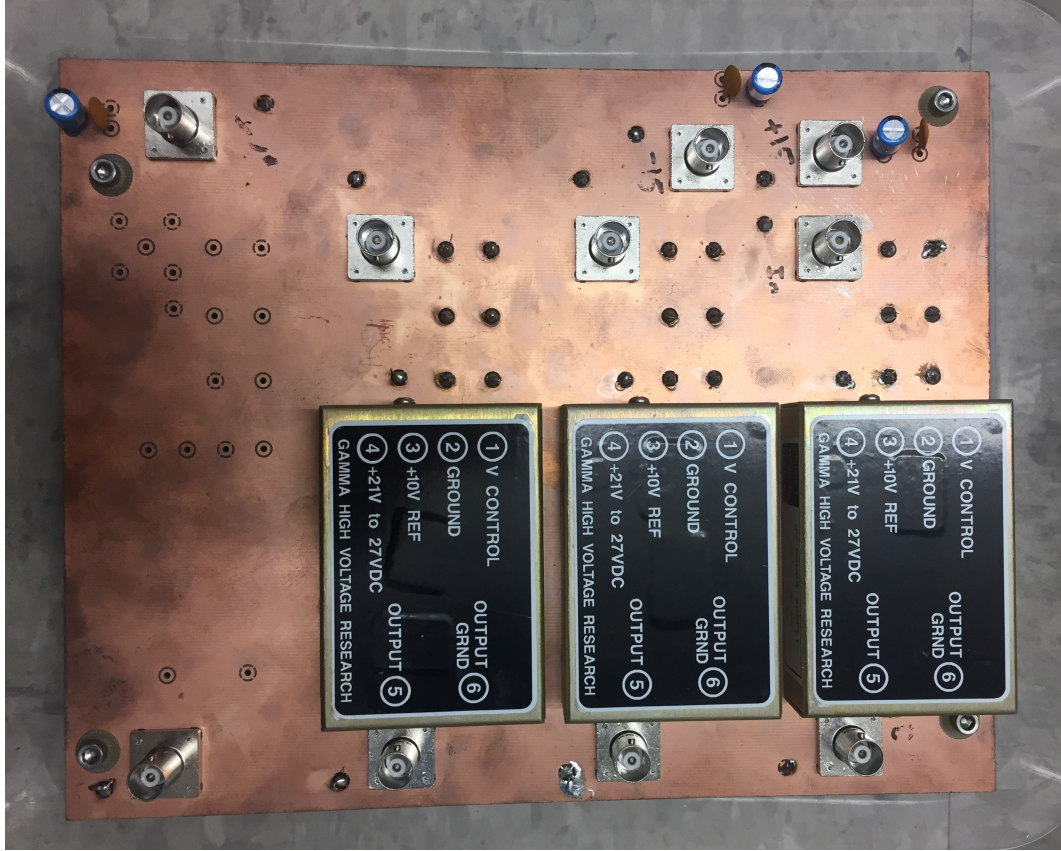


Fig. 5.2. Image of the high voltage module.

feedthrough of the vacuum chamber. Figure (5.2) shows the image of the high voltage module.

The nano-position stage is designed and assembled. It's composed of two 5-axis stage and one 2-axis stage. The microscale electrostatic lens sample adapter is designed and machined. It's made of machinable ceramic which is insulating material for the high voltage insulation. The electrostatic lens sample is mounted on the ceramic adapter and is positioned by a manual 5-axial stage. The 2-axis and 5-axis motorized stages are stacked together. The picomotors are used to control the motorized stages with a step size of 20 nm. The silicon wafer is mounted on the stack of the motorized stages. The 5-axis motorized stage is used to tune the surface of the silicon wafer and make it in parallel with microscale electrostatic lens sample. The

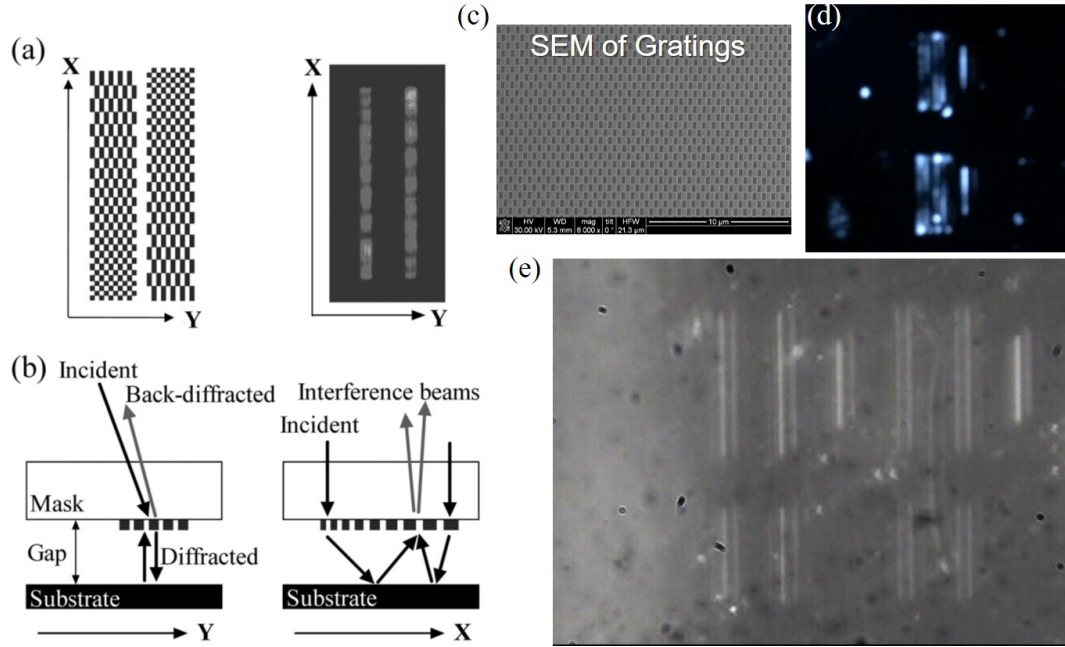


Fig. 5.3. Gap detection system. (a) The pair of chirped gratings are used to detect the gap with nanometer accuracy. (b) The working mechanism of ISPI gratings. [7] (c) The SEM image of the fabricated ISPI grating on the electron source sample. (d) The image of the detected interference fringes of the ISPI gratings. The gap is proportional to the numbers of the peaks in the interference pattern. (e) The rough measurement of the gap using grating imaging. The 5 gratings on the right are real and fabricated on the microcolumn sample. The 5 gratings on the left are image of the real gratings reflected by the Si wafer. The distance between these two sets of gratings is proportional to the gap. The scale is set according to the known distance between the real 5 gratings.

2-axis motorized stage is used to scan the silicon sample to write arbitrary patterns with the help of laser switching. With the help of Prof. Xianfan Xu's group, ISPI gratings are designed and fabricated on the electron source sample to detect the gap between the electron source and the silicon wafer with nanometer accuracy. Figure (5.3) show the gap detection system. With the help of Prof. Xianfan Xu's group, the ISPI gratings are designed and fabricated to detect the gap or equivalently the working distance. Figure (5.3)(a) shows the pair of chirped gratings are used to de-

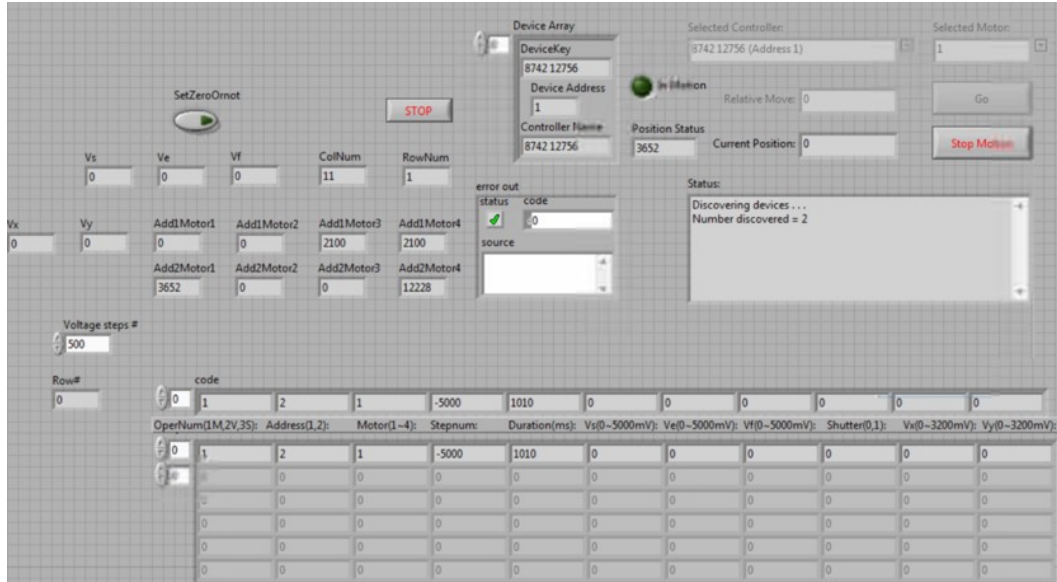


Fig. 5.4. Image of the first stage multiple electron-beam lithography system.

tect the gap with nanometer accuracy. (b) shows the working mechanism of ISPI gratings. [7] (c) shows the SEM image of the fabricated ISPI grating on the electron source sample. (d) The image of the detected interference fringes of the ISPI gratings. The gap is proportional to the numbers of the peaks in the interference pattern. (e) The rough measurement of the gap using grating imaging. The 5 gratings on the right are real and fabricated on the microcolumn sample. The 5 gratings on the left are image of the real gratings reflected by the Si wafer. The distance between these two sets of gratings is proportional to the gap. The scale is set according to the known distance between the real 5 gratings. The accuracy of the rough measurement is better than a few hundreds of nanometers. The working distance is detected first by the rough measurement using the grating imaging. And then the accurate measurement is achieved by the ISPI grating interference patterns.

The vacuum system composes of a main chamber, a vacuum pump station with diaphragm and turbo pump series, an ion pump and ion gauge. After loading a new silicon sample in the chamber, the diaphragm and turbo pump series pump the chamber to 10^{-6} mbar. Then they are turned off and the ion pump is on to

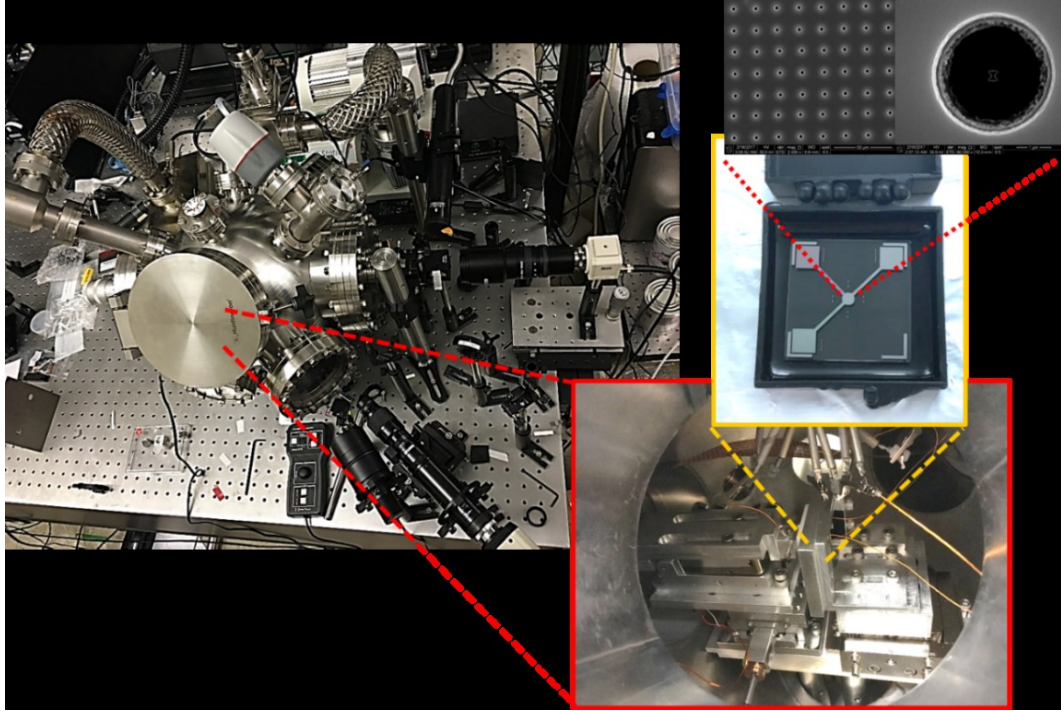


Fig. 5.5. Image of the first stage multiple electron-beam lithography system.

maintain the vacuum. The ion pump doesn't moving parts so it won't disturb the stage while the lithography is being done. The ultimate vacuum level for this system is in the order of 10^{-7} mbar. The vacuum pressure is too high for photoemission and will make the quantum yield much lower than theoretical predictions. But with the limited resources, the first stage lithography system is enough to demonstrate the concept.

The lithography system is controlled by a Labview program shown in Figure (5.4). A script file is generated to control the high voltages, the UV laser shutter and the stage to write arbitrary patterns on the silicon wafer. Figure (5.5) shows the first stage multiple electron-beam lithography system. To further improve the stability of the stages, the whole system is sitting on a stable optical table to filter out high frequency vibrations.

6. LITHOGRAPHY RESULTS AND DISCUSSION

6.1 Lithography Results

Using the multiple electron-beam lithography system, lithography was tested with the following parameters. The 266-nm laser power shining on the plasmonic sample is 200 mW with the beam diameter of 500 μm . The gold and Cs layers were not used in order to narrow the initial electron energy spread and thus reducing the aberrations of the electron optics. The work function of chrome is 4.5 eV so the initial energy spread is 0.16 eV. The vacuum pressure is 2.0×10^{-6} mbar. V_{Source} is -200 V, V_{Ex} is -50 V and V_{Focus} is ramping from -231.2 V to -256.2 V. The working distance (WD) is set at 10 μm . The scaling factor of the SPEBL device is set to be 2 so the diameter of the electrostatic lens aperture is 6 μm . The dielectric material thicknesses are 2 μm and 4 μm respectively. The C and bowtie aperture plasmonic lenses are chosen as the electron source and the size of the hot spot is estimated to be less than 50 nm.

Figure (6.1) shows the simulation results of the focused beam size using the real geometry parameters, voltages, and working distance of the microcolumns. The electron source is set as a disk with a diameter of 50 nm. The initial electron energy spread is estimated to be 0.5 eV. (a) shows the image of the electrons landing on the silicon wafer. (b) shows the histogram of current density distribution with respect to R coordinate. The magnification of the electron optics is -0.5 and an electron beam with FWHM of 25 nm can be achieved. Within the 25 nm diameter beam spot, 25% of the overall current is useful. Given the low initial electron energy spread, the aberration of the electrostatic lens is less than 10 nm.

Figure (6.2)(a) shows an example design consists of three electrodes, separated by 2 μm and 4 μm respectively. The diameter of the electron lens aperture is 6 μm . By varying the electric potentials, this design can project the source image onto a resist

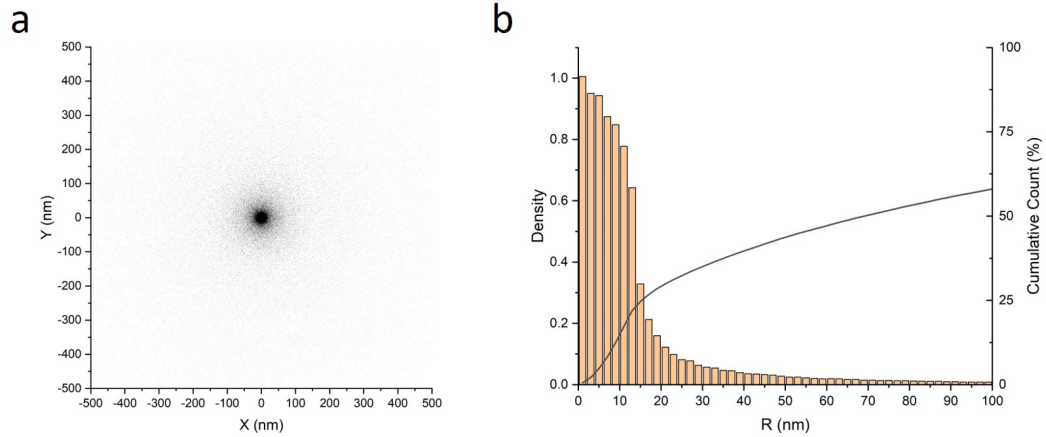


Fig. 6.1. Simulation results of the focused beam size using the real geometry parameters, voltages, and working distance of the micro-columns. The electron source is set to a disk with a diameter of 50 nm. The initial electron energy spread is estimated to be 0.5 eV. (a) The image of the electrons landing on the silicon wafer. (b) The histogram of current density distribution with respect to R coordinate. The magnification of the electron optics is -0.5 and an electron beam with FWHM of 25 nm can be achieved. Within the 25 nm diameter beam spot, 25% of the overall current is useful.

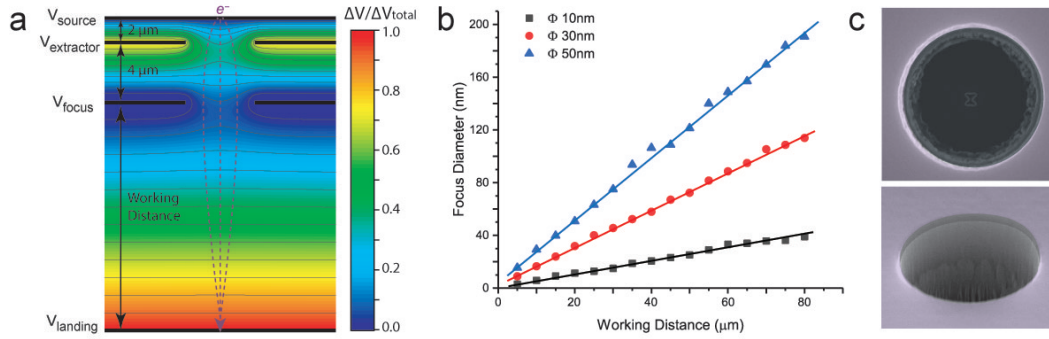


Fig. 6.2. Compact microscale electrostatic lens designed for plasmonic electron emitters. (a) The electric potential distribution of this compact design. (b) The optimized focused beam size as a function of working distance and source size (Φ). (c) SEM images of the top and oblique views of an electron lens. The lens diameter is 6- μ m diameter. The center bowtie aperture can be clear seen.

surface at a controllable magnification ratio and a corresponding working distance. I simulated the projection of electron beamlet with a 0.5-eV initial energy dispersion at the emitter and a 200-eV landing energy at the resist surface. As shown in Figure (6.2)(b), the beam size increases almost linearly with source size and magnification ratio. The achievable beam size is about 3 nm in FWHM using a 10-nm source at a 5- μm working distance. The beam size can be further improved by increasing the landing energy to reduce the effect of beam aberration. Figure (6.2)(c) shows the SEM images of the microscale electron electrostatic lens fabricated on top of an emitter.

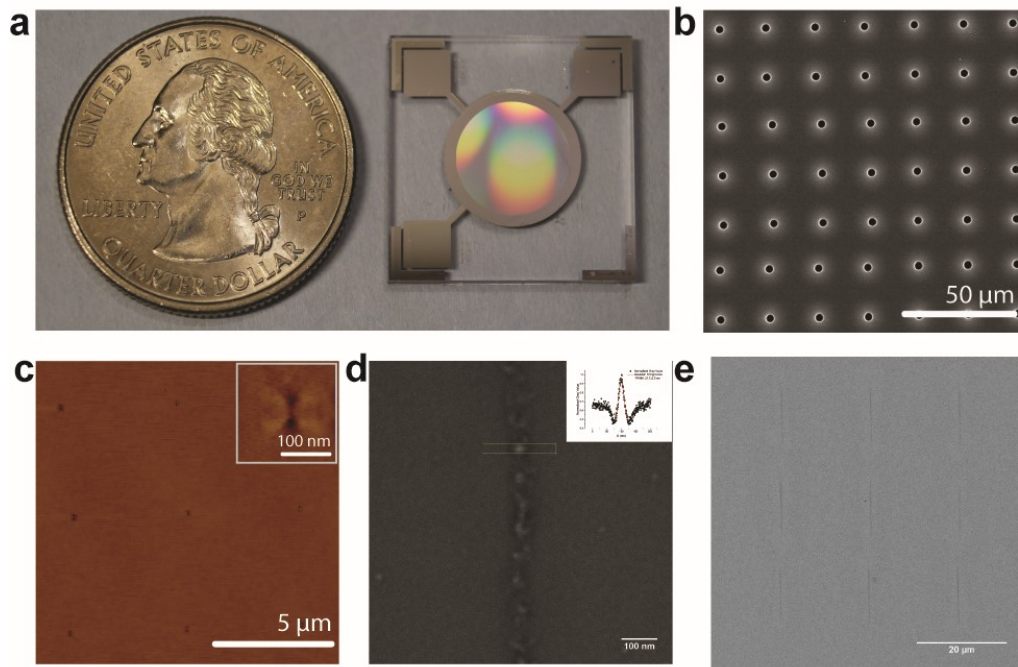


Fig. 6.3. Maskless lithography results using SPEBL method. (a) An SPEBL device that can produce more than 1 million electron beamlets within a 1-cm² area. (b) SEM image of an array of electron lenses. (c) The proximity lithography result shows the size of the electron source. (d) SEM image of a line of dots at 22-nm FWHM written by SPEBL at a working distance of 10 μm . (e) SEM image of parallel-writing of an array of lines.

Figure (6.3)(a) shows the photo of a SPEBL device capable of generating more than 1 million beamlets within a 1-cm² area without crosstalk. This prototype device also contains electrical contact pads and metrology gratings shown in the previous chapter. Figure (6.3)(b) is the SEM image of an array. The effective source size of the emitter is evaluated in a proximity lithography test. During the test, an array of emitters is held at a nanoscale gap above a silicon wafer coated with a 100-nm-thick PMMA resist. A 50-V acceleration voltage is applied across the emitters and the wafer to get a 1:1 map of the source array. Figure (6.3)(c) shows the AFM image of the developed resist pattern. The measured full width half maximum (FWHM) of exposure dots is about 20 nm and the exposed depth is about 75 nm. In the beam projection tests, the performance of SPEBL is demonstrated using a source size of about 50 nm at a working distance of about 10 m. During the exposure, the silicon wafer moves linearly at 80 nm per step on a motorized stage and the control system simultaneously scan the focusing electrode voltage to vary the projection distance. The exposure dosages are controlled by laser pulse duration at a constant beam current. Figure (6.3)(d) and (e) show SEM images of the exposure results. The electron beam resist is chosen to be HSQ for its high resolution ability. An FWHM dot size of 22 nm is obtained at the optimized focusing voltage. Besides writing the lines of dots to demonstrate the resolution, some arbitrary patterns are writtern on PMMA.

Figure (6.4)(a) shows an array of letters of 'NSF' written on the PMMA resist. Figure (6.4)(b) shows the Zoom-in AFM image of the 'NSF'. These test results demonstrated the concept of SPEBL. The lithography resolution can reach a few nanometres using demagnified beamlets and emitters of a smaller source size. Because of the compact size and high efficiency of the SPEBL device, the lithography throughput can be greatly enhanced by employing millions of emitters for parallel writing. Lithography using SPEBL is a promising solution to enable the agile maskless nanoscale fabrication with high throughput, meeting the needs for low-cost, high-throughput fabrication in scientific studies and industrial production. By adding the electrodes

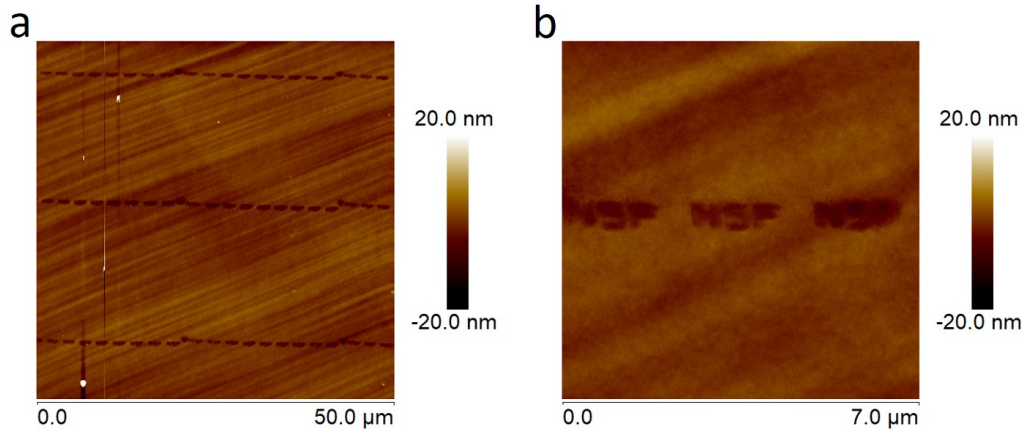


Fig. 6.4. Patterns writtern by SPEBL. (a) An array of letters of 'NSF' are written on the PMMA resist. (b) Zoom-in AFM image of the 'NSF'.

for secondary electron collection, this high-speed technique can also be used for fast electron beam microscopy. Such a low-cost, high-throughput scheme promises a new route towards the next generation of nano-manufacturing.

6.2 Discussion

In order to improve lithography resolution, the work function (WD) should be reduced. Simulation results show that if the WD is kept at 5 μm , the magnification is reduced to be $0.25\times$ and the beam size can be reduced to 13 nm. Previously, the limitation of reducing the WD and/or increasing voltage across the WD was delamination of the focus layer shown in Figure (4.9). This is solved to add transition layer between Cr and SiO_2 layers. The transition layer is made of a 10-nm thick alloy composed of Ti and SiO_2 and it releases the shear stress effectively. Another limitation is the vacuum breakdown between the electrodes and the silicon wafer. This can be taken care of by making the surface clean and ultra-smooth.

Up to now, the record of beam number of individually addressable multiple electron-beam lithography system is on the order of 10K which is kept by MAP-

PER [89]. In our system, the beam number can be scaled to be on the order of 1M. In future industrial implantation of this technology, several engineering challenges must be tackled such as pattern data management, lithography process control, which are common for all maskless lithography approaches. The rapid rastering of writing beamlets can be achieved by adding electrostatic deflectors.

The potential lithography throughput of this scheme is in the order of 10 wafers per hour at sub-10 nm node. The DUV light source with 193 nm wavelength and low work function materials can be used to improve the quantum yield of photoemission. The UV beamlets projection system is also needed for real lithography systems. The quasi-3D plasmonic design with 2500 intensity enhancement and 20-nm size hot spot shown in Figure (2.6) can be used to improve the photon focusing efficiency. More advanced electron optics design (including limiting aperture, deflector, etc) should be used to reduce the aberrations of the electron optics when the initial electron energy spread is large. The plasmonic lens design with shaped hotspot (Figure (2.4) and (2.5)) can be used to build a shaped electron beam lithography system. The shaped electron beam lithography is very used for mask fabrication because of its higher throughput and low line edge roughness.

This report shows the progress and results of the high-throughput electron-beam lithography system with multiple plasmonic enhanced photoemission beamlets. The demo system and lithography results demonstrate the feasibility and potential of the alternative lithography approach with the advantage of acceptable throughput, high resolution and low cost.

With some easy modifications, this multiple electron-beam system can also be used high-throughput low electron energy microscopy (LEEM) [90] and high-throughput-high-resolution electron-beam induced deposition (EBID) [91, 92].

LEEM is scanning electron-beam microscopy with electron landing energy below 100 V. It is very useful in imaging soft materials like biological tissues and polymers with nanoscale resolution. The optical microscopy cannot achieve such resolution and normal SEM or TEM has the resolution but the electron landing energy is too high

and destroys the soft sample. So LEEM is suitable for imaging these materials with high accuracy. But the LEEM has a complicated electron optics because the electron beam is first accelerate to achieve high resolution and decelerate just before landing the sample. The throughput is also low especially when its used to inspect a large area with fine features like the EUV mask. So the multiple electron-beam system reported here can be easily modified to achieve the high-resolution-high-throughput LEEM.

The main approach of nanofabrication now is top-down process which removes material to do the patterning. Another approach is to build the device bottom up. At micron or submicrometer scale, 3D printing can be used to do additive manufacturing. At nanoscale, electron-beam-induced deposition (EBID) is used. EBID is a process of decomposing gaseous molecules by an electron beam leading to deposition of non-volatile fragments onto a nearby substrate. There are two limitations of the current EBID technique. One is the low throughput and the other is the resolution limit due to the back scattered electrons from the substrate. The low throughput can be addressed by the multiple electron-beams operating at the same time. The backed scattered electrons can be reduced by low electron energy. So the multiple electron-beam system has the potential to improve the EBID technique.

REFERENCES

REFERENCES

- [1] E. Slot, M. J. Wieland, G. d. Boer, P. Kruit, G. F. t. Berge, A. M. C. Houkes, R. Jager, T. v. d. Peut, J. J. M. Peijster, S. W. H. K. Steenbrink, T. F. Teepen, A. H. V. v. Veen, and B. J. Kampherbeek, "Mapper: high throughput maskless lithography," pp. 6921 – 6921 – 9, 2008.
- [2] P. Petric, C. Bevis, M. McCord, A. Carroll, A. Brodie, U. Ummethala, L. Grella, A. Cheung, and R. Freed, "Reflective electron beam lithography: A maskless ebeam direct write lithography approach using the reflective electron beam lithography concept," *Journal of Vacuum Science and Technology B, Nanotechnology and Microelectronics: Materials, Processing, Measurement, and Phenomena*, vol. 28, no. 6, pp. C6C6–C6C13, 2010.
- [3] M. Esashi, A. Kojima, N. Ikegami, H. Miyaguchi, and N. Koshida, "Development of massively parallel electron beam direct write lithography using active-matrix nanocrystalline-silicon electron emitter arrays," *Microsystems and Nanoengineering*, vol. 1, p. 15029, 2015.
- [4] S. T. Coyle, D. Holmgren, X. Chen, T. Thomas, A. Sagle, J. Maldonado, B. Shamoun, P. Allen, and M. Gesley, "Prototype raster multibeam lithography tool," *Journal of Vacuum Science and Technology B: Microelectronics and Nanometer Structures Processing, Measurement, and Phenomena*, vol. 20, no. 6, pp. 2657–2661, 2002.
- [5] Z. Gan, Y. Cao, R. A. Evans, and M. Gu, "Three-dimensional deep sub-diffraction optical beam lithography with 9 nm feature size," *Nature Communications*, vol. 4, p. 2061, 2013.
- [6] L. Pan, Y. Park, Y. Xiong, E. Ulin-Avila, Y. Wang, L. Zeng, S. M. Xiong, J. Rho, C. Sun, D. B. Bogy, and X. Zhang, "Maskless plasmonic lithography at 22 nm resolution," *Scientific Reports*, vol. 1, p. 175, 2011.
- [7] X. Wen, A. Datta, L. M. Traverso, L. Pan, X. Xu, and E. E. Moon, "High throughput optical lithography by scanning a massive array of bowtie aperture antennas at near-field," *Scientific Reports*, vol. 5, 2015.
- [8] K. Unal, J. Frommer, and H. K. Wickramasinghe, "Ultrafast molecule sorting and delivery by atomic force microscopy," *Applied Physics Letters*, vol. 88, no. 18, p. 183105, 2006.
- [9] D. C. Spanner, "The principle of the invariance of brightness in electron optics," *British Journal of Applied Physics*, vol. 18, no. 6, p. 773, 1967.
- [10] M. Guillorn, M. Simpson, G. Bordonaro, V. Merkulov, L. Baylor, and D. Lownes, "Fabrication of gated cathode structures using an in situ grown vertically aligned carbon nanofiber as a field emission element," *Journal of Vacuum Science*

- and Technology B: Microelectronics and Nanometer Structures*, vol. 19, no. 2, pp. 573–578, 2001.
- [11] L. R. Baylor, W. L. Gardner, X. Yang, R. J. Kasica, M. A. Guillorn, B. Blalock, H. Cui, D. K. Hensley, S. Islam, D. H. Lowndes, A. V. Melechko, V. I. Merkulov, D. C. Joy, P. D. Rack, M. L. Simpson, and D. K. Thomas, “Initial lithography results from the digital electrostatic e-beam array lithography concept,” *Journal of Vacuum Science and Technology B*, vol. 22, no. 6, pp. 3021–3024, 2004.
 - [12] Y. Wen, Z. Du, and L. Pan, “Design of electrostatic microcolumn for nanoscale photoemission source in massively parallel electron-beam lithography,” *J. of Micro/Nanolithography, MEMS, and MOEMS*, vol. 14, no. 4, p. 043508, 2015.
 - [13] R. H. Ritchie, “Plasma losses by fast electrons in thin films,” *Physical Review*, vol. 106, no. 5, pp. 874–881, 1957.
 - [14] E. A. Stern and R. A. Ferrell, “Surface plasma oscillations of a degenerate electron gas,” *Physical Review*, vol. 120, no. 1, pp. 130–136, 1960.
 - [15] V. V. Temnov, “Ultrafast acousto-magneto-plasmonics,” *Nat Photon*, vol. 6, no. 11, pp. 728–736, 2012.
 - [16] W. F. Andress, H. Yoon, K. Y. M. Yeung, L. Qin, K. West, L. Pfeiffer, and D. Ham, “Ultra-subwavelength two-dimensional plasmonic circuits,” *Nano Letters*, vol. 12, no. 5, pp. 2272–2277, 2012.
 - [17] K. A. Willets and R. P. Van Duyne, “Localized surface plasmon resonance spectroscopy and sensing,” *Annual Review of Physical Chemistry*, vol. 58, pp. 267–297, 2007.
 - [18] S. Vedantam, H. Lee, J. Tang, J. Conway, M. Staffaroni, and E. Yablonovitch, “A plasmonic dimple lens for nanoscale focusing of light,” *Nano Letters*, vol. 9, no. 10, pp. 3447–3452, 2009.
 - [19] J. A. Schuller, E. S. Barnard, W. S. Cai, Y. C. Jun, J. S. White, and M. L. Brongersma, “Plasmonics for extreme light concentration and manipulation,” *Nature Materials*, vol. 9, no. 3, pp. 193–204, 2010.
 - [20] W. Srituravanich, N. Fang, C. Sun, Q. Luo, and X. Zhang, “Plasmonic nanolithography,” *Nano Letters*, vol. 4, no. 6, pp. 1085–1088, 2004.
 - [21] J. M. Pitarke, V. M. Silkin, E. V. Chulkov, and P. M. Echenique, “Theory of surface plasmons and surface-plasmon polaritons,” *Reports on Progress in Physics*, vol. 70, no. 1, pp. 1–87, 2007.
 - [22] Y.-Y. Teng and E. A. Stern, “Plasma radiation from metal grating surfaces,” *Physical Review Letters*, vol. 19, no. 9, pp. 511–514, 1967.
 - [23] A. Otto, “Excitation of nonradiative surface plasma waves in silver by the method of frustrated total reflection,” *Zeitschrift fr Physik A Hadrons and nuclei*, vol. 216, no. 4, pp. 398–410, 1968.
 - [24] E. Kretschmann and H. Raether, “Notizen: Radiative decay of non radiative surface plasmons excited by light,” *Zeitschrift fr Naturforschung A*, vol. 23, no. 12, p. 2135, jan 1968.

- [25] D. H. Dowell and J. F. Schmerge, “Quantum efficiency and thermal emittance of metal photocathodes,” *Physical Review Special Topics-Accelerators and Beams*, vol. 12, no. 7, 2009.
- [26] H. Puff, “Zur theorie der sekundarelektronenemission der transportproze. i. formulierung des problems,” *physica status solidi (b)*, vol. 4, no. 1, pp. 125–138, 1964.
- [27] C. N. Berglund and W. E. Spicer, “Photoemission studies of copper and silver: Theory,” *Physical Review*, vol. 136, no. 4A, pp. A1030–A1044, 1964.
- [28] A. Sommer, *Photoemissive materials: preparation, properties, and uses*. Wiley, 1968.
- [29] W. E. Spicer, “Optical transitions in which crystal momentum is not conserved,” *Physical Review Letters*, vol. 11, no. 6, pp. 243–245, 1963.
- [30] K. L. Jensen, P. G. OShea, D. W. Feldman, and N. A. Moody, “Theoretical model of the intrinsic emittance of a photocathode,” *Applied Physics Letters*, vol. 89, no. 22, p. 224103, 2006.
- [31] W. E. Spicer, “Possible non-one-electron effects in the fundamental optical excitation spectra of certain crystalline solids and their effect on photoemission,” *Physical Review*, vol. 154, no. 2, pp. 385–394, 1967.
- [32] H. Jouin, M. Raynaud, G. Duchateau, G. Geoffroy, A. Sadou, and P. Martin, “Quantum-classical model for the surface plasmon enhanced photoemission process at metal surfaces,” *Physical Review B*, vol. 89, no. 19, p. 195136, 2014.
- [33] D. W. O. Heddle, *Electrostatic lens systems*, 2nd ed. Bristol, UK ; Philadelphia: IOP, 2000.
- [34] D. C. Joy, “The aberration corrected sem,” *AIP Conference Proceedings*, vol. 788, no. 1, pp. 535–542, 2005.
- [35] O. Scherzer, “Über einige Fehler von Elektronenlinsen,” *Zeitschrift für Physik*, vol. 101, pp. 593–603, Sep. 1936.
- [36] J. B. Pendry, “Negative refraction makes a perfect lens,” *Phys. Rev. Lett.*, vol. 85, pp. 3966–3969, Oct 2000.
- [37] N. Fang, H. Lee, C. Sun, and X. Zhang, “Sub-diffraction-limited optical imaging with a silver superlens,” *Science*, vol. 308, no. 5721, pp. 534–537, 2005.
- [38] Y. T. Cheng, Y. Takashima, Y. Yuen, P. C. Hansen, J. B. Leen, and L. Hesselink, “Ultra-high resolution resonant c-shaped aperture nano-tip,” *Optics Express*, vol. 19, no. 6, pp. 5077–5085, 2011.
- [39] N. Zhou, X. F. Xu, A. T. Hammack, B. C. Stipe, K. Z. Gao, W. Scholz, and E. C. Gage, “Plasmonic near-field transducer for heat-assisted magnetic recording,” *Nanophotonics*, vol. 3, no. 3, pp. 141–155, 2014.
- [40] O. Mahboub, S. C. Palacios, C. Genet, F. J. Garcia-Vidal, S. G. Rodrigo, L. Martin-Moreno, and T. W. Ebbesen, “Optimization of bull’s eye structures for transmission enhancement,” *Optics Express*, vol. 18, no. 11, pp. 11 292–11 299, 2010.

- [41] P. Lalanne, J. P. Hugonin, and J. C. Rodier, "Theory of surface plasmon generation at nanoslit apertures," *Physical Review Letters*, vol. 95, no. 26, 2005.
- [42] Y. Wang, Z. Du, Y. Park, C. Chen, X. Zhang, and L. Pan, "Quasi-3d plasmonic coupling scheme for near-field optical lithography and imaging," *Optics Letters*, vol. 40, no. 16, pp. 3918–3921, 2015.
- [43] D. R. Lide, "Crc handbook of chemistry and physics, 88th ed.(brief article)(book review)," *Journal of the American Chemical Society*, vol. 130, no. 1, 2008.
- [44] M. N. Polyanskiy. Refractive index database. [Online]. Available: <https://refractiveindex.info>
- [45] D. R. Smith, J. B. Pendry, and M. C. K. Wiltshire, "Metamaterials and negative refractive index," *Science*, vol. 305, no. 5685, pp. 788–792, 2004.
- [46] V. M. Shalaev, "Optical negative-index metamaterials," *Nature Photonics*, vol. 1, no. 1, 2007.
- [47] C. M. Soukoulis and M. Wegener, "Materials science. optical metamaterials—more bulky and less lossy," *Science*, vol. 330, no. 6011, 2010.
- [48] T. J. Yen, W. J. Padilla, N. Fang, D. C. Vier, D. R. Smith, J. B. Pendry, D. N. Basov, and X. Zhang, "Terahertz magnetic response from artificial materials," *Science*, vol. 303, no. 5663, 2004.
- [49] S. Linden, C. Enkrich, M. Wegener, J. Zhou, T. Koschny, and C. M. Soukoulis, "Magnetic response of metamaterials at 100 terahertz," *Science*, vol. 306, no. 5700, 2004.
- [50] C. Enkrich, M. Wegener, S. Linden, S. Burger, L. Zschiedrich, F. Schmidt, J. F. Zhou, T. Koschny, and C. M. Soukoulis, "Magnetic metamaterials at telecommunication and visible frequencies," *Physical review letters*, vol. 95, no. 20, 2005.
- [51] R. A. Shelby, D. R. Smith, and S. Schultz, "Experimental verification of a negative index of refraction," *Science*, vol. 292, no. 5514, pp. 77–79, 2001.
- [52] S. Zhang, W. Fan, N. C. Panoiu, K. J. Malloy, R. M. Osgood, and S. R. J. Brueck, "Experimental demonstration of near-infrared negative-index metamaterials," *Physical review letters*, vol. 95, no. 13, 2005.
- [53] E. Economou, "Surface plasmons in thin films," *Physical Review*, vol. 182, no. 2, pp. 539–554, 1969.
- [54] *Electromagnetic surface modes*. Wiley, 1982.
- [55] S. A. Maier and H. A. Atwater, "Plasmonics: Localization and guiding of electromagnetic energy in metal/dielectric structures," *Journal of Applied Physics*, vol. 98, no. 1, 2005.
- [56] D. K. Gramotnev and S. I. Bozhevolnyi, "Plasmonics beyond the diffraction limit," *Nature Photonics*, vol. 4, no. 2, 2010.
- [57] K. R. Catchpole and A. Polman, "Plasmonic solar cells," *Optics express*, vol. 16, no. 26, 2008.

- [58] M. Muralidhar Singh, G. Vijaya, M. Krupashankara, B. Sridhara, and T. Shridhar, "Deposition and characterization of aluminium thin film coatings using dc magnetron sputtering process," *Materials Today: Proceedings*, vol. 5, no. 1, pp. 2696–2704, 2018.
- [59] A. L. Cauduro, R. Dos Reis, G. Chen, A. K. Schmid, H.-G. Rubahn, and M. Madsen, "Work function mapping of MoOx thin-films for application in electronic devices," *Ultramicroscopy*, vol. 183, pp. 99–103, 2017.
- [60] B. C. Yao, C. P. Wang, S. C. Tseng, and C. H. Tsai, "Design and fabrication of micro carbon nanotube column for electron-beam lithography," in *5th IEEE Conference on Nanotechnology, 2005.*, July 2005, pp. 673–676 vol. 2.
- [61] H. Yang, A. Jin, Q. Luo, J. Li, C. Gu, and Z. Cui, "Electron beam lithography of hsq/pmma bilayer resists for negative tone lift-off process," *Microelectronic Engineering*, vol. 85, no. 56, pp. 814–817, 2008.
- [62] H. Kanter, "Slow-electron mean free paths in aluminum, silver, and gold," *Phys. Rev. B*, vol. 1, pp. 522–536, Jan 1970.
- [63] G. Hechenblaikner, T. Ziegler, I. Biswas, C. Seibel, M. Schulze, N. Brandt, A. Scholl, P. Bergner, and F. T. Reinert, "Energy distribution and quantum yield for photoemission from air-contaminated gold surfaces under ultraviolet illumination close to the threshold," *Journal of Applied Physics*, vol. 111, no. 12, p. 12, 2012.
- [64] J. L. LaRue, J. D. White, N. H. Nahler, Z. Liu, Y. Sun, P. A. Pianetta, D. J. Auerbach, and A. M. Wodtke, "The work function of submonolayer cesium-covered gold: A photoelectron spectroscopy study," *The Journal of Chemical Physics*, vol. 129, no. 2, p. 024709, 2008.
- [65] S. J. Pennycook, *Scanning Transmission Electron Microscopy*, ser. Scanning transmission electron microscopy: imaging and analysis. New York, NY : Springer New York : Imprint: Springer, 2011.
- [66] S. L. Flegler, *Scanning and transmission electron microscopy : an introduction*. New York: New York : W.H. Freeman, 1993.
- [67] A. Cerezo and M. K. Miller, "Einzel lenses in atom probe designs," *Surface Science*, vol. 246, no. 13, pp. 450–456, 1991.
- [68] M. Despont, U. Staufer, C. Stebler, R. Germann, and P. Vettiger, "Microfabrication of lenses of a miniaturized electron column," *Microelectronic Engineering*, vol. 27, no. 14, pp. 467–470, 1995.
- [69] C. D. Bubeck, A. Fleischmann, G. Knell, R. Y. Lutsch, E. Plies, and D. Winkler, "Miniature electrostatic lens for generation of a low-voltage high current electron probe," *Nuclear Instruments and Methods in Physics Research Section A: Accelerators, Spectrometers, Detectors and Associated Equipment*, vol. 427, no. 12, pp. 104–108, 1999.
- [70] E. Yin, A. D. Brodie, F. C. Tsai, G. X. Guo, and N. W. Parker, "Electron optical column for a multicolumn, multibeam direct-write electron beam lithography system," *Journal of Vacuum Science and Technology B*, vol. 18, no. 6, pp. 3126–3131, 2000.

- [71] K. Young Chul, K. Dae-Wook, A. Seungjoon, C. Sang-Kook, K. Dae-Yong, and K. Ho Seob, "Effect of the einzel lens structure in microcolumn," *Japanese Journal of Applied Physics*, vol. 43, no. 6S, p. 3728, 2004.
- [72] Y. Neo, A. Koike, T. Fujino, H. Mimura, T. Yoshida, T. Nishi, M. Nagao, and H. Murata, "The electron optics properties of micro-column with field emitter," *2012 25th International Vacuum Nanoelectronics Conference (Ivnc)*, pp. 90–91, 2012.
- [73] Z. Du, Y. Wen, L. Traverso, A. Datta, C. Chen, X. Xu, and L. Pan, "Design and fabrication of electrostatic microcolumn in multiple electron-beam lithography," pp. 9777 – 9777 – 13, 2016.
- [74] H. C. Pfeiffer, D. E. Davis, W. A. Enichen, M. S. Gordon, T. R. Groves, J. G. Hartley, R. J. Quickle, J. D. Rockrohr, W. Stickel, and E. V. Weber, "El4, a new generation electronbeam lithography system," *Journal of Vacuum Science and Technology B*, vol. 11, no. 6, pp. 2332–2341, 1993.
- [75] Y. Nakayama, S. Okazaki, N. Saitou, and H. Wakabayashi, "Electronbeam cell projection lithography: A new highthroughput electronbeam directwriting technology using a specially tailored si aperture," *Journal of Vacuum Science and Technology B*, vol. 8, no. 6, pp. 1836–1840, 1990.
- [76] T. H. P. Chang, D. P. Kern, and L. P. Muray, "Microminiaturization of electron optical systems," *Journal of Vacuum Science and Technology B*, vol. 8, no. 6, pp. 1698–1705, 1990.
- [77] Y. C. Kim, D. W. Kim, S. Ahn, T. S. Oh, J. B. Kim, Y. S. Roh, D. G. Hasko, and H. S. Kim, "Inspection method for contact/via-holes using a low-energy electron microcolumn," *Journal of Vacuum Science and Technology B*, vol. 27, no. 6, pp. 3208–3212, 2009.
- [78] E. Kratschmer, H. S. Kim, M. G. R. Thomson, K. Y. Lee, S. A. Rishton, M. L. Yu, S. Zolgharnain, B. W. Hussey, and T. H. P. Chang, "Experimental evaluation of a 20×20 mm footprint microcolumn," *Journal of Vacuum Science and Technology B*, vol. 14, no. 6, pp. 3792–3796, 1996.
- [79] L. P. Muray, U. Stauffer, D. P. Kern, and T. H. P. Chang, "Performance measurements of a 1kev electronbeam microcolumn," *Journal of Vacuum Science and Technology B*, vol. 10, no. 6, pp. 2749–2753, 1992.
- [80] T. S. Oh, D.-W. Kim, Y. C. Kim, S. Ahn, G.-h. Lee, and H. S. Kim, "Inspection of open defects in a thin film transistor-liquid crystal display panel by using a low-energy electron microcolumn," *Journal of Vacuum Science and Technology B*, vol. 28, no. 6, pp. C6C69–C6C73, 2010.
- [81] R. Saini, Z. Jandric, I. Gory, S. A. M. Mentink, and D. Tuggle, "Assembled microelectromechanical system microcolumns for miniature scanning electron microscopies," *Journal of Vacuum Science and Technology B*, vol. 24, no. 2, pp. 813–817, 2006.
- [82] R. Saini, Z. Jandric, K. Tsui, T. Udeshi, and D. Tuggle, "Assembled micro-electromechanical-systems microcolumn from a single layer silicon process," *Journal of Vacuum Science and Technology B*, vol. 22, no. 6, pp. 3168–3173, 2004.

- [83] N. de Jonge, M. Allieux, J. T. Oostveen, K. B. K. Teo, and W. I. Milne, "Optical performance of carbon-nanotube electron sources," *Physical Review Letters*, vol. 94, no. 18, p. 186807, 2005.
- [84] W. Haynes, *CRC Handbook of Chemistry and Physics, 96th Edition*. CRC Press, 2015.
- [85] H. Yasuda, T. Haraguchi, H. Yabara, K. Takahata, H. Murata, E. Rokuta, and H. Shimoyama, "Multiaxis and multibeam technology for high throughput maskless e-beam lithography," *Journal of Vacuum Science and Technology B*, vol. 30, no. 6, 2012.
- [86] M. Mankos, S. Coyle, A. Fernandez, A. Sagle, P. Allen, W. Owens, J. Sullivan, and T. H. P. Chang, "Multisource optimization of a column for electron lithography," *Journal of Vacuum Science and Technology B*, vol. 18, no. 6, pp. 3010–3016, 2000.
- [87] P. Petric, C. Bevis, A. Carroll, H. Percy, M. Zywno, K. Standiford, A. Brodie, N. Bareket, and L. Grella, "Rebl: A novel approach to high speed maskless electron beam direct write lithography," *Journal of Vacuum Science and Technology B*, vol. 27, no. 1, pp. 161–166, 2009.
- [88] C. Klein, J. Klikovits, L. Szikszai, E. Platzgummer, and H. Loeschner, "Projection mask-less lithography (pml2)," *Microelectronic Engineering*, vol. 87, no. 5, pp. 1154–1158, 2010.
- [89] V. Kuiper, B. J. Kampherbeek, M. J. Wieland, G. d. Boer, G. F. t. Berge, J. Boers, R. Jager, T. v. d. Peut, J. J. M. Peijster, E. Slot, S. W. H. K. Steenbrink, T. F. Teeppen, and A. H. V. v. Veen, "Mapper: High throughput maskless lithography," in *25th European Mask and Lithography Conference*, Jan 2009, pp. 1–5.
- [90] E. Bauer, "Low energy electron microscopy," *Reports on Progress in Physics*, vol. 57, no. 9, p. 895, 1994.
- [91] W. F. van Dorp, B. van Someren, C. W. Hagen, P. Kruit, and P. A. Crozier, "Approaching the resolution limit of nanometer-scale electron beam-induced deposition," *Nano Letters*, vol. 5, no. 7, pp. 1303–1307, 2005.
- [92] M. H. Song and K. Furuya, "Fabrication and characterization of nanostructures on insulator substrates by electron-beam-induced deposition," *Science and Technology of Advanced Materials*, vol. 9, no. 2, 2008.

VITA

VITA

Zhidong Du received his B.S. in Physics in July 2010 from Department of Modern Physics at University of Science and Technology of China (USTC) in Hefei, Anhui, China. He received his M.S. in August 2014 from Department of Mechanical Engineering at Purdue University in West Lafayette, IN.

Zhidong Du has research experiences in cold atom physics, all optical switching (AOS) of magnetic materials and plasmonic enhanced multiple electron beam lithography. He also did some work in nanoscale heat transfer.

Journal Publication

Zhang, J., Ji, S., Chen, Z., Zhang, L., **Du, Z.**, Yan, B., Pan, G., Zhao, B., Deng, Y., Zhai, H., Chen, S., Pan, J., Collective Dipole Oscillations of a Spin-Orbit Coupled Bose-Einstein Condensate. *Physical Review Letters*, 2012. 109(11).

Zhang, L., Zhang, J., Ji, S., **Du, Z.**, Zhai, H., Deng, Y., Chen, S., Zhang, P., Pan, J., Stability of excited dressed states with spin-orbit coupling. *Physical Review A*, 2013. 87(1): p. 4.

Ji, S., Zhang, J., Zhang, L., **Du, Z.**, Zheng, W., Deng, Y., Zhai, H., Chen, S., Pan, J., Experimental determination of the finite-temperature phase diagram of a spin-orbit coupled Bose gas. *Nature Physics*, 2014. 10(4): p. 314-320.

Chen, C., **Du, Z.**, and Pan, L., Optothermal Modeling of Plasmonic Nanofocusing Structures With Nonlocal Optical Response and Ballistic Heat Transport. *Journal of Micro and Nano-Manufacturing*, 2015. 3(1): p. 011009-011009.

Chen, C., **Du, Z.**, and Pan, L., Extending the diffusion approximation to the boundary using an integrated diffusion model. *AIP Advances*, 2015. 5(6): p. 067115.

Wang, Y., **Du, Z. (Co-first author)**, Park, Y., Chen, C., Zhang, X., Pan, L., Quasi-3D plasmonic coupling scheme for near-field optical lithography and imaging. *Optics Letters*, 2015. 40(16): p. 3918-3921.

Wen, Y., **Du, Z.**, and L. Pan, Design of electrostatic microcolumn for nanoscale photoemission source in massively parallel electron-beam lithography. *Journal of Micro/Nanolithography, MEMS, and MOEMS*, 2015. 14(4): p. 043508-043508.

Chen, C., **Du, Z.**, Wang, J. Pan, L., Temperature mapping using molecular diffusion based fluorescence thermometry via simultaneous imaging of two numerical apertures. *Optics Express*, 2016. 24(23): p. 26599-26611.

Du, Z., Chen, C., Cheng, F., Liu, Y., Pan, L., Prediction of Deterministic All-Optical Switching of Ferromagnetic Thin Film by Ultrafast Optothermal and Optomagnetic Couplings, *Scientific Reports*, 7, 13513, 2017.

Chen, C., Shen, T., **Du, Z.**, Zhang, J., Wang, J., Marconnet, A., Pan, L.*, Microscale Two-Dimensional (2D) Temperature Mapping by Ratiometric Fluorescence Imaging under Orthogonal Excitations, *Experimental Thermal and Fluid Science*, 94, 168-171, 2018.

Chen, C., Vasudevan, I., **Du, Z.**, Xu, X., Pan, L., Ultrafast time-resolved measurement of energy transport at the metal-liquid interface, *Applied Physics Letters*, 112(25), 253105, 2018.